Wind farm wake flow recovery with the use of kites

Jop Kokkedee

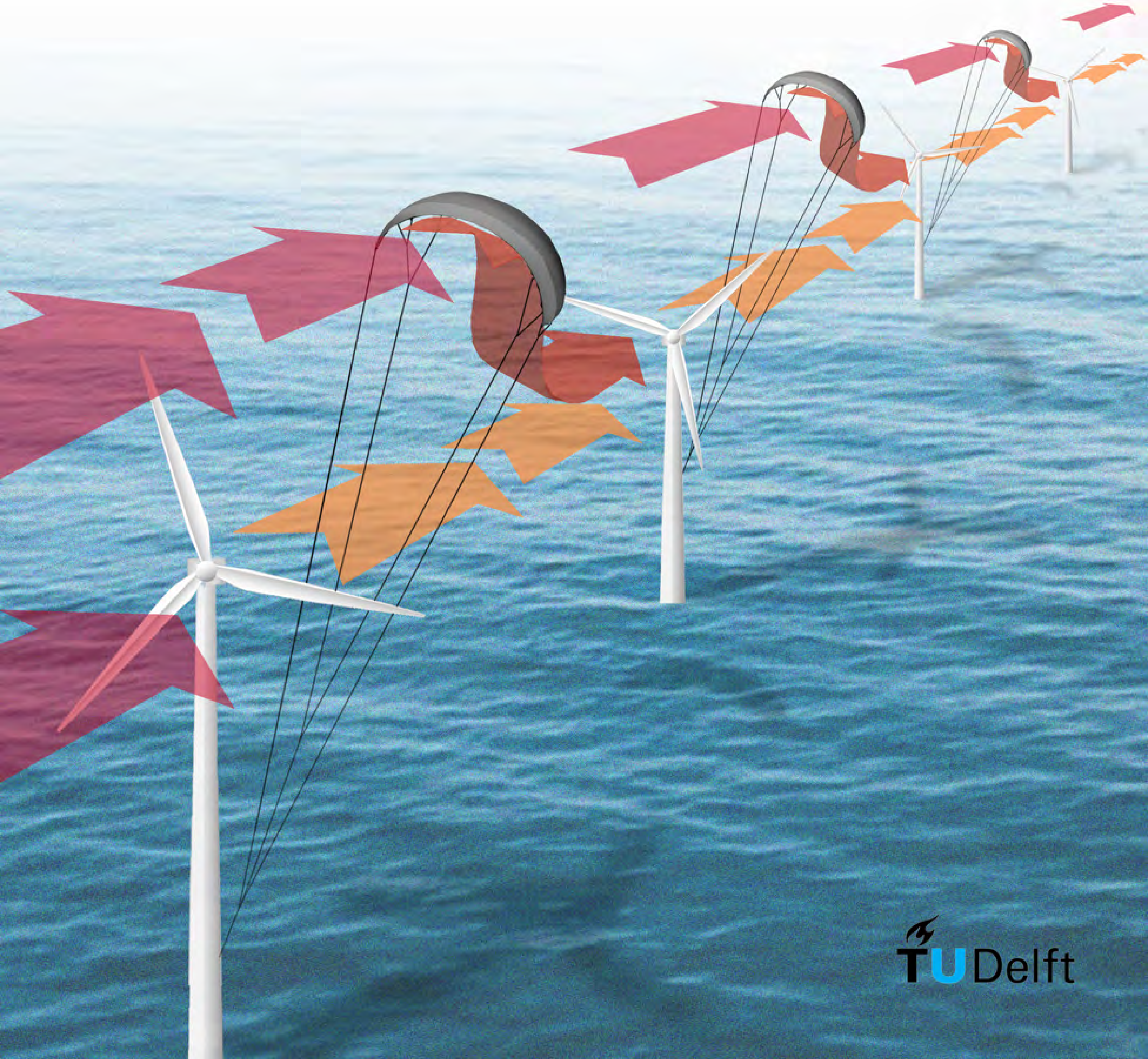

TU Delft

WIND FARM WAKE FLOW RECOVERY WITH THE USE OF KITES

A thesis submitted to the Delft University of Technology in partial
fulfillment
of the requirements for the degree of

Master of Science in Sustainable Energy Technologies

To be defended publicly on Tuesday June 28, 2022 at 09:00 AM.

by

Jop Kokkedee

June 2022

Chair:	Dr. ir. Roland Schmehl
Supervisor:	Dr. ir. Wim Bierbooms
Supervisor:	Dr. ir. Dries Allaerts
Exam committee member:	Dr. ir. Alexander van Zuijlen

Jop Kokkedee: *Wind farm wake flow recovery with the use of kites* (2022)
🅭🅯 This work is licensed under a Creative Commons Attribution 4.0 International License. To view a copy of this license, visit
http://creativecommons.org/licenses/by/4.0/.

The work in this thesis was made in the:

Group:	Wind Energy Group
Department:	Department of Aerodynamics, Wind Energy, Flight Performance and Propulsion
Faculty:	Faculty of Aerospace Engineering
University:	Delft University of Technology

Chair	Roland Schmehl
Supervisor	Wim Bierbooms
Supervisor	Dries Allaerts
Exam committee member	Alexander van Zuijlen

ABSTRACT

With an ever increasing demand for sustainable energy, limitations of current sustainable technologies are studied widely. In wind farms, the so-called wake effect provides the biggest limitation on wind farm total power output. Using wind from the unaffected boundary layer to re-energize the wind flow in the wake provides a method of limiting this wake effect. In this study, kites are introduced to steer the wind flow of the unaffected boundary layer into the wake through a downwash velocity.

RANS (Reynolds-averaged Navier-Stokes) simulations are performed in Computational Fluid Dynamics (CFD) software OpenFOAM of the atmospheric boundary layer (1), a small four-turbine wind farm (2) and a wind farm with static kites between the turbines (3). The turbines are modelled through the actuator disc approach, and kites are introduced through the more complex actuator line method. Results of the Athmospheric boundary layer (ABL) and wind farm simulations correspond well with literature. Through extensive kite parameter studies, an optimal layout of kites in the wind farm is presented yielding a wind farm efficiency increase of 2.3 %, which increases over 5% for even larger kites. Kite size and the kite's downstream location show to impact the re-energising levels of the wake flow the most. The kites generate a downwash wake instead of a single downwash velocity, a finding that should further be studied in future research.

ACKNOWLEDGEMENTS

2018 was an important year in my life: it was the year I started my Master in Sustainable Energy Technologies (SET) and founded my own company with my business partner Merlijn. Two things that completely changed my life and perception of life.

Initially, my focus in the field of sustainable energy was drawn to energy storage technologies, under the impression that energy storage is the main problem to be solved for our planet to yield the ever desired sustainable world. After an introduction course on wind energy, however, dr. Wim Bierbooms introduced me and my fellow class mates to all the possibilities wind energy has into reaching a sustainable world. The lecture discussing local winds and wind farms in mountains got me hooked on the subject of wind energy. Wim suggested me to take the elective course of Airborne Wind Energy, taught by dr. Roland Schmehl. In this course Roland introduced me to the use of kites for electricity generation purposes. His enthusiasm on the airborne wind energy field sparked my interest in the application of kites.

In the summer of 2020, Covid had slowed down my business' growth. A perfect time to start the final chapter of my master: the master Thesis. Luckily, Wim offered a Thesis topic that combined two topics in which my interest had sparked: wind energy and the application of kites. The Thesis proposition was to simulate a wind farm using computational fluid dynamics, and study the effects kites (introduced in the wind farm) may or may not have on the wake flow in the wind farm. I want to thank Wim Bierbooms for accepting me to take on this master Thesis and introducing me into the Wind Energy group of TU Delft. A difficult start to my Thesis was my non-existing knowledge of computational fluid dynamics. To smoothen this knowledge gap, a second supervisor, dr. Dries Allaerts, decided to assist me in this Thesis. Without his expertise on computational fluid dynamics this Thesis would probably have taken at least another year to finish up.

Close to the end of my Thesis, the exam committee was selected. Dr. Roland Schmehl, who sparked my interest in the application of kites, was asked to chair the exam committee: the circle was complete. Dr. Alexander van Zuijlen, who had helped me numerous times with questions on computational fluid dynamics, joined the exam committee as well.

I would like to thank Wim, Dries, Roland and Alexander for enriching me with knowledge during this Thesis. Especially Wim and Dries I would like to thank for always making time to answer my questions, assist me when I was having problems, and their understanding towards working on this Thesis part-time as my company had grown rapidly again from the sum-

mer of 2020 onwards.

Besides my exam committee, I would like to thank my friends and family, and especially my roommates Karsten, Jasmin, Merlijn, Boudewijn and Seymour, for celebrating with me during the good times, and having my back during the more stressful moments of this Thesis. Finally, a big shoutout to Marilise who designed the awesome front page of this Thesis!

CONTENTS

LIST OF FIGURES

LIST OF TABLES

LIST OF ACRONYMS AND SYMBOLS

List of acronyms:

NWR	Near Wake Region	3
FWR	Far Wake Region	4
IWR	Intermediate Wake Region	4
CFD	Computational Fluid Dynamics	ii
RANS	Reynold-averaged Navier-Stokes	ix
LES	Large Eddy Simulation	9
AD	Actuator Disc	x
ABL	Athmospheric boundary layer	ii
AL	Actuator Line	10
Ma	Mach number	18
Re	Reynolds number	19
N-S equations	Navier-Stokes equations	19
DNS	Direct Numerical Simulation	19
URANS	Unsteady Reynolds-averaged Navier-Stokes	20
DES	Detached Eddy Simulation	20
FV	Finite Volume	22
UDS	Upwind Differencing Scheme	23
CDS	Central Differencing Scheme	23
ALR	Adiabatic Lapse Rate	vii
AoA	angle of attack	68

List of symbols:

L	Lift	13
D	Drag	13
F_z	Gravitational Force	13
F_a	Aerodynamic Force	13
F_t	Tether Force	13
ρ	Density	13
C_L	Lift coefficient	13
C_D	Drag coefficient	13
v_a	Apparent wind velocity	13

S	Kite surface area	13
m_k	Kite mass	13
α	Angle of attack	14
AR	Aspect Ratio	15
b	wingspan	15
C_{l0}	Basic Free Stream Lift Coefficient	15
V	Free stream wind speed	15
w	Downwash velocity	15
ϵ_{dw}	Downwash angle	15
t	time	18
$\underline{u}$	velocity in 3 dimensions [s]	18
$\sum_n F_{n,j}$	sum of all external forces [N]	18
E	internal energy [J]	18
p	pressure [Pa]	18
τ_{ij}	shear stress tensor	18
q_i	heat flux [W/m^2]	18
f_i	body force per unit mass [N/kg]	18
U_0	advection velocity [m/s]	19
c_0	speed of sound [m/s]	19
L	characteristic length for the flow [m]	19
μ	dynamic viscosity of the fluid	19
v_T	eddy viscosity	21
sij	strain rate	21
dij	Kronecker delta function	21
k	turbulence kinetic energy	ix
ϵ	rate of dissipation of turbulent kinetic energy	ix
ω	specific dissipation rate	ix
u_{ref}	reference wind speed at height z_{ref}	28
z_0	surface roughness value	28
u_z	wind speed at height z	28
u_*	friction velocity	28
κ	von Karman constant	28
Ψ	stability correction function	28
L_{obh}	Obhukov length	28
n	Hellman exponent	28
z_{ref}	reference height	30
d_z	ground-normal displacement height	30

d_x	domain length	31
d_y	domain width	31
d_z	domain height	31
D_{wt}	wind turbine diameter	31
N_{cells}	number of grid cells	32
$\dot{m}$	mass flow rate	39
$\mathbf{T}$	thrust force	40
A_{wt}	actuator disc area	39
P_{wt}	wind turbine power	40
Δp	pressure drop	40
U_r	rotor velocity	40
U_e	outlet velocity	40
$\mathbf{a}$	induction factor	40
C_T	thrust coefficient	41
C_P	power coefficient	41
ρ_{ref}	monitored incoming fluid density	42
u_m	spatially averaged incoming velocity on monitored region	42
$\mathbf{n}$	surface-normal vector of the actuator disc pointing upstream	42
p_{OF}	pressure definition in OpenFOAM	52
p_{amb}	ambient pressure	52
η_{wf}	wind farm efficiency	55
P_i	Power output for turbine i	55
c_{kite}	kite chord length	65

1 INTRODUCTION

1.1 NECESSITY OF WIND ENERGY

Since the oil crisis in the 1970's (Salameh [2015]), the interest in wind energy for electricity generation purposes has rapidly increased. Especially in regions where wind is in abundance, like in northern Europe, shown in Figure 1.1, wind plays an important role in the transition towards a more sustainable energy future. Currently, the largest wind turbine offshore the Netherlands has a rating of 12MW and has set the world record of producing 262 MWh in a single day, enough energy for 30,000 households (Steffen, L [2019]). The Netherlands alone has over 7.9 million households, requiring a theoretical minimum of 263 of these turbines. Unfortunately perfect operating conditions are rare, and average wind turbine power output at less optimal conditions is reduced to about 2.5 MW. To provide Dutch households of enough energy at least 2000 turbines will be required, if these turbines would operate all day and all night. Hence, concentration of many turbines into larger wind farms is required to provide the necessary energy.

Concentrating wind turbines into wind farms brings many additional advantages. First of all, especially offshore it is much cheaper to electrically connect wind turbines to a single power line transporting the combined generated electricity to the main land. Secondly, locating multiple wind turbines together optimises the installation and maintenance efforts and costs, as travelling from one wind turbine to another takes less time and in one wind farm, similar maintenance issues may be found, decreasing total maintenance time (Moskalenko et al. [2010]). Finally, a wind turbine is regarded as a nuisance for human living or working close to this turbine, because of its size and the noise a turbine makes. Concentrating wind turbines into wind farms in less rural areas limits these effects of a wind farm.

These advantages gave rise to the idea of optimisation of wind farm area by placing as many wind turbines as possible together while ensuring these turbines to be not too close together for safe operations. Research has been focused on increasing the wind turbine density per area while keeping the wind power output per wind turbine at an acceptable level (losses less than 50%). A wrongful expectation assumes the most optimal layout of a wind farm is where the wind turbines are located as close as possible together, limited by the blade length of the wind turbines and with a safety margin for any collapsing wind turbine. Practically, this is not the case, because of effects that limit the efficiency, thus the power output, of a wind farm. The most important effect limiting wind farm efficiency is the wake effect.

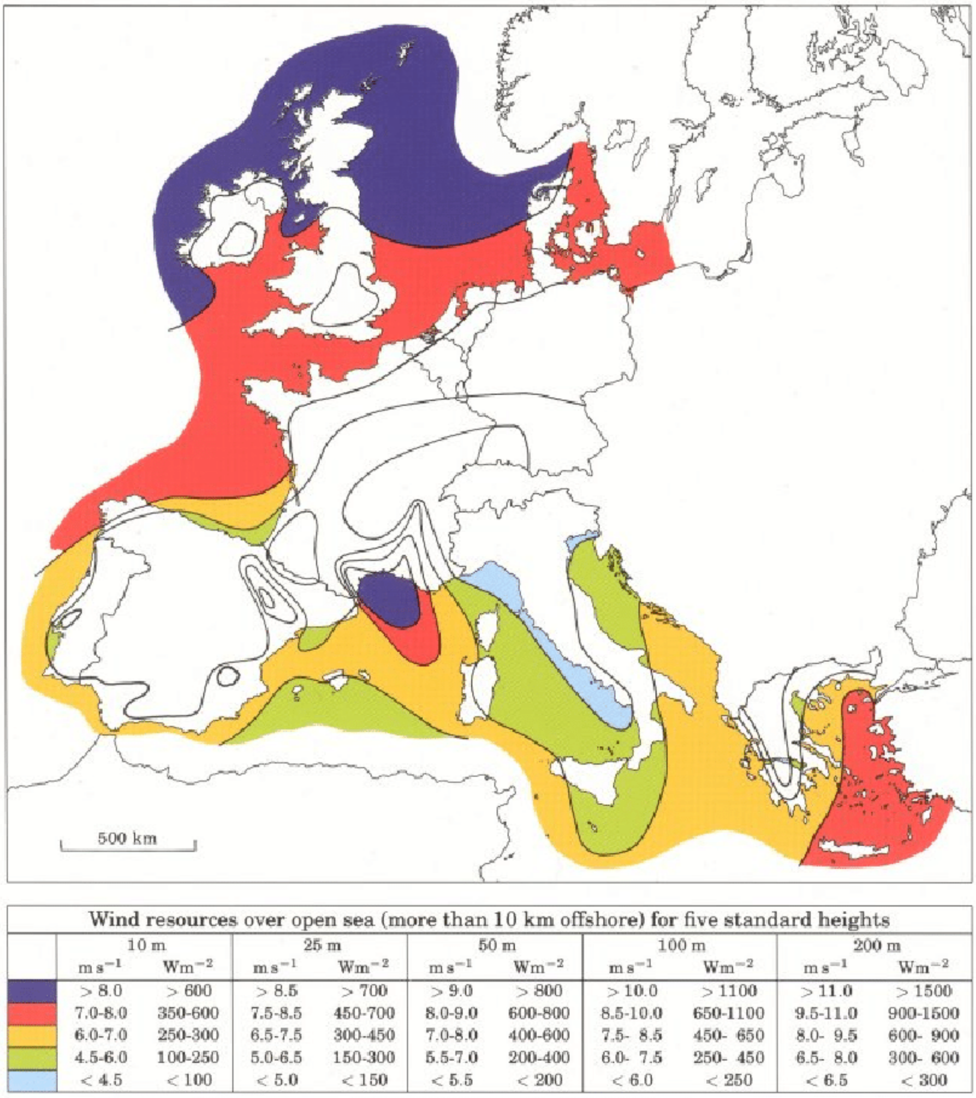

Wind resources over open sea (more than 10 km offshore) for five standard heights	10 m		25 m		50 m		100 m		200 m	
	$\mathrm{m\,s^{-1}}$	$\mathrm{Wm^{-2}}$	$\mathrm{m\,s^{-1}}$	$\mathrm{Wm^{-2}}$	$\mathrm{m\,s^{-1}}$	$\mathrm{Wm^{-2}}$	$\mathrm{m\,s^{-1}}$	$\mathrm{Wm^{-2}}$	$\mathrm{m\,s^{-1}}$	$\mathrm{Wm^{-2}}$
🟪	> 8.0	> 600	> 8.5	> 700	> 9.0	> 800	> 10.0	> 1100	> 11.0	> 1500
🟥	7.0-8.0	350-600	7.5-8.5	450-700	8.0-9.0	600-800	8.5-10.0	650-1100	9.5-11.0	900-1500
🟨	6.0-7.0	250-300	6.5-7.5	300-450	7.0-8.0	400-600	7.5- 8.5	450- 650	8.0- 9.5	600- 900
🟩	4.5-6.0	100-250	5.0-6.5	150-300	5.5-7.0	200-400	6.0- 7.5	250- 450	6.5- 8.0	300- 600
🟦	< 4.5	< 100	< 5.0	< 150	< 5.5	< 200	< 6.0	< 250	< 6.5	< 300

Figure 1.1: Off-shore wind atlas of northern Europe (Wijnant et al. [2014])

1.2 WAKE THEORY

1.2.1 Velocity deficit

A simple way to explain the wake effect is with the use of the first law of thermodynamics: in a closed system, energy is conserved, but energy conversions are allowed. The main purpose of a wind turbine is converting kinetic energy from the wind to electricity. Hence the wind flow downwind of the wind turbine will have a lower energy density compared to the undisturbed wind flow. As wind farms consist of many wind turbines, many turbines will be located in this downwind 'wake' of another wind turbine for all wind directions. This means these wind turbines will experience a lower energy density wind flow which results in less kinetic energy to be converted to electricity. The energy production of a wind farm, while not considering these wake effects, will thus always result in lower energy values than what is expected. (White [1999])

Clear illustrations for the effect on efficiency and power output of a wind farm are shown in the research done by Barthelmie, Hansen, Fransen et al (Barthelmie et al. [2009]). They reported that wake losses account for 10-20% of total theoretical power output in large offshore wind farms, presented here for the Horns Rev wind farm located off the coast of Denmark. Wake losses of up to 40% of theoretical power output were measured for the smallest turbine spacing and the wind direction parallel to this wind turbine spacing. These numbers drastically lower the annual wind energy output and result in lower revenues for wind farm owners.

1.2.2 Wake regions

Swirling of air is another effect a wind turbine has on the wind flow. The combined effect of the swirling of air and the decrease in kinetic energy content of the wind flow causes the wake flow to follow a vortical helix motion like can be seen in Figure 1.2 and increases the turbulence intensity within the wake (Schmitz, S [2015]). The turbulence intensity is defined as the intensity of wind velocity fluctuation, where in more general terms, turbulence is a measure for chaotic changes in flow properties, like pressure and fluid velocity.

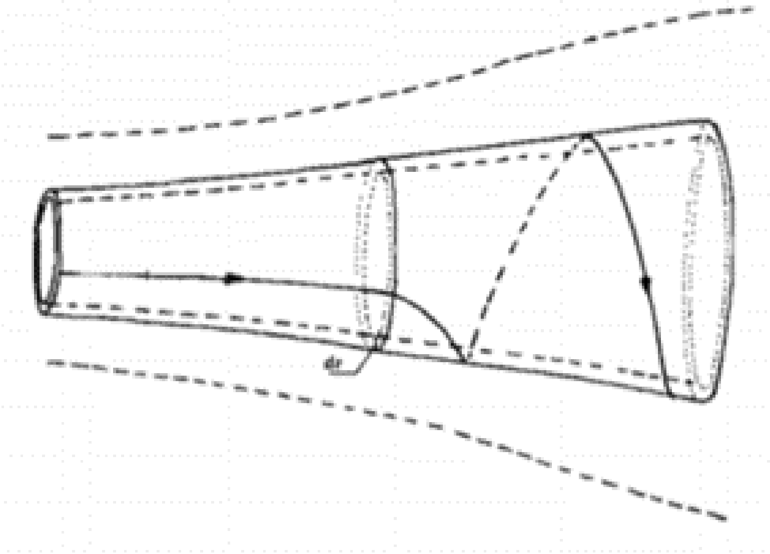

Figure 1.2: Swirling of air visualisation (Schmitz, S [2015])

These vortical helix motions continue for a few rotor diameters, about two to four, behind the wind turbine before they collapse (Brand et al. [2011]). This region, where the vortical helix motions are visible, is called the Near Wake Region (NWR). In the NWR, the largest wind speed deficits are present due to the combined effects of the partial wind kinetic energy conversion to electricity and the vortices created by the blades, causing additional turbulence. The region affected by the wind turbine thus has a lower wind speed than the unaffected ambient boundary layer. The region of this wind speed transition is called the wind shear layer and is often described as a top hat form as can be seen in figure Figure 1.3b.

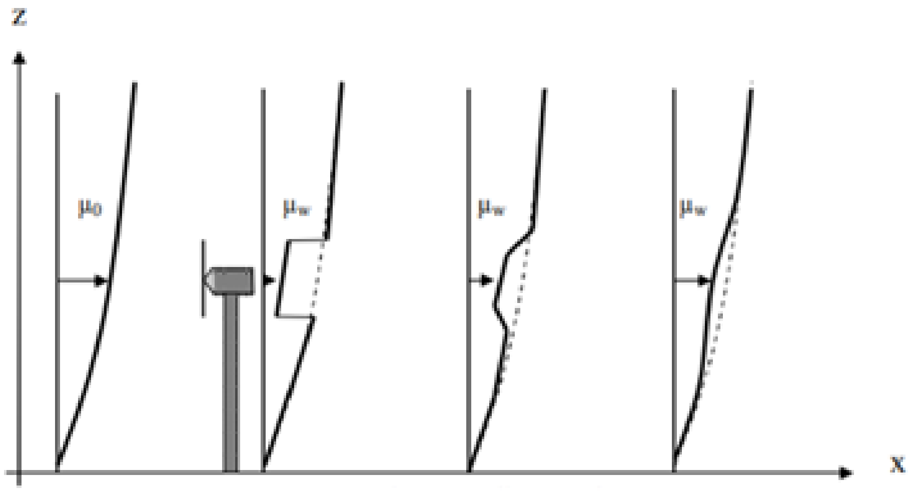

Figure 1.3: Wind speed shear layer affected by the wake of a wind turbine. 3a: unaffected wind speed shear layer. 3b: near wake. 3c: intermediate wake. 3d: far wake (Brand et al. [2011]).

Further downwind, behind the NWR, vortices start to affect each other by rolling over the other vortices. Furthermore, the unaffected wind boundary layer starts to mix with the larger sized wake vortices. Together, these two effects eventually result in the wake vortices collapsing increasing turbulence within the wake. This turbulence causes an even stronger mixture of wake wind flow and the ambient boundary layer. The shear layer experiences transport from the unaffected ambient boundary layer to the lower wind speed region. A stronger wind speed gradient in the shear layer results in a larger transport of momentum from the ambient boundary layer to the lower wind speed layer. This region, where the vortices start to collapse and the ambient boundary layer starts to mix with the lower wind speed region is called the Intermediate Wake Region (IWR). Figure Figure 1.3c shows this region in which can be seen that the wind speed gradient is decreasing.

Eventually the vortices are completely gone and a highly turbulent structure is remaining. Here the lower wind speed layer is regenerated by wind from the ambient unaffected wind boundary layer because of the turbulent mixing. The wind speed gradient in the wind shear layer decreases even further and causes the shear layer to stretch over a further wind layer. If this wind tube has had enough distance to spread the shear layer uniformly over the wind tube, the centre line of the wind tube can even be recovered. This region of wake recovery is called the Far Wake Region (FWR) and can be seen in Figure 1.3d. In wind farms this means that the distance of this FWR is required between an upwind and downwind wind turbine for the wind flow to recover and the downwind turbine to experience an acceptable level of wind kinetic energy (Brand et al. [2011]) (Nygaard [2014]).

1.2.3 The turbulence energy cascade

The collapse of large vortical turbulent structures into smaller structures, transferring the turbulent energy while collapsing, is often referred to as the turbulence energy cascade. The basic principle of the turbulence energy cascade is presented in Figure 1.4. Turbulence is caused by objects like wind turbines. The vortices generated, having the size of the objects, eventually will affect each other and start to collapse in ever decreasing smaller sized vortices. Turbulence energy is transferred throughout this process from the largest scales to the smallest scales. At the smallest scales, the vortices dissipate and the turbulence energy is dissipated. These vortex scales are referred to as the dissipative range. Whereas the larger turbulence scales strongly depend on the geometry of the objects that caused them, the vortices in the dissipative range are only indirectly affected by the initial objects and are often regarded as being random.

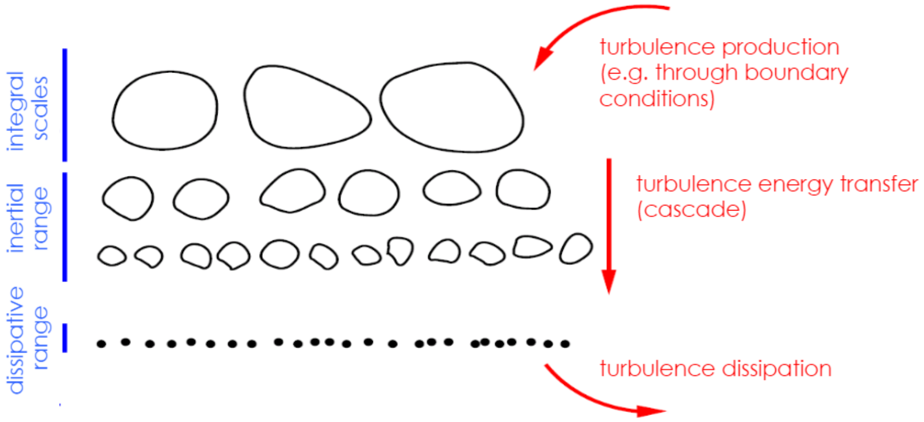

Figure 1.4: Basic principle of the wind energy cascade where turbulence energy is transferred from larger vortical structures to smaller structures until dissipated by the smallest turbulent vortices. (Hickel, S [2021])

1.3 PROBLEM OUTLINE

In re-energizing the disturbed wind flow in the wake of a wind turbine (and to increase the efficiency of a wind farm), two aspects are key. First, the distance required between an upwind and downwind turbine is important as it needs to be large enough for the wind shear layer to spread out over the total wind tube and lead to partial or full wind flow recovery. Second, turbulence is required to force the undisturbed ambient boundary layer and the lower wind speed region to mix. Locating wind turbines closer to another by increasing the wind speed gradient from the ambient wind boundary layer to the lower wind speed region will provide the means to increase total wind farm efficiency. This, because of the velocity increase at downwind turbines resulting in a smaller area of wind farm required for the production of similar (to the original less efficient wind farm) wind farm power output values.

A conclusion that might be drawn from these two aspects is to try to increase the turbulence within the wake as much as possible to enforce the mixing of the unaffected boundary layer and the wake. Increased turbulence results in increased loading on wind turbines, thereby lowering the efficiency and lifetime of wind turbines (Frandsen [2007]). Quoting Frandsen: "The standard deviation of wind speed fluctuations is a known key parameter for both extreme- and fatigue loading, and it is argued and found to be justified that a model for change in turbulence intensity alone may account for increased fatigue loading in wind farms". Mixing between the two wind flows however is an important phenomenon for wake recovery, especially in stable conditions (Cañadillas et al. [2020]) where it was measured that under stable atmospheric stratification wake recovery required much more distance between wind turbines, and wind farms. Thus, even though an acceptable increase in turbulence is necessary, the focus of solutions should not just lie on increasing the turbulence in the wake. A different method should be applied to re-energize the wake, and thus increase wind farm efficiency.

Trying to find this different method, the two main wind flows travelling through a wind park should be studied. First, the wind flow covering the height of the entire wind turbine. This flow that reaches the leading edge of a wind farm still has its full energy density. However, a few wind turbines in, and a large proportion of the energy in the wind flow is converted to electricity by the wind turbines (Meyers and Meneveau [2010]). The second wind flow, as presented and evaluated by Cal et al. [2010], comes from the free wind layer unaffected by the wake of the wind turbines (above the affected wind layer). Especially from the fourth wind turbine row onwards, the largest proportion of the wind kinetic energy experienced by the downwind turbines comes from this free wind flow (because of the mixing effects) (Barthelmie et al. [2009]). Finding a way of steering this wind flow from the unaffected boundary layer into the wake is therefore the main focus of this study.

Different means or methods to attract wind from the unaffected wind flow into the wake are studied next. Research to these different methods is limited and only several quantitative results have been presented and will be discussed in Section 1.4.

1.4 PROPOSED SOLUTIONS

Generally speaking methods for increasing wind farm efficiency can be sorted into two categories. One category focuses on changing the blade angles or rotor angles of the wind turbines in the wind farm, another category applies novel external systems or designs that redirect the wake itself or steers wind from the unaffected boundary layer into the wake. For both systems, some examples will be presented, however we focus on the second category since this research focuses on a novel technology to re-energize the wake. The problem however, is that even though much research is done towards investigating and modelling the turbulence mixing of the wind between the unaffected boundary layer and the wake, not much solutions have been presented for this second category.

1.4.1 Turbine Solutions

Akay et al. [2013] provides a summary of the state of the art of wind turbine control techniques that have increased wind farm efficiency over the past few decades. Actively yawing the wind turbine away from the wind direction results in the wake being steered away from downstream wind turbines. Additionally, tilting the rotor of the wind turbine backwards results in the wake being directed to the ground. Maximum obtainable energy improvements with a combined yaw and tilt model are estimated at 4.6-7.1 %. A disadvantage of these control techniques, however, is an increase in loading on the wind turbines, limiting the efficiency increase of a wind farm.

In the Netherlands, Gebraad et al. [2014] studied the process of yaw misalignment of several wind turbines in a wind farm. Setting different yaw alignments for the wind turbines results in wakes directing into different positions and having different velocities. Using Computational Fluid Dynamics (CFD), with sufficient accuracy, a significant increase of 5% in power production was observed. In contrast to increased turbulence resulting in larger forcing on the wind turbines, this concept of yaw misalignment also resulted in decreased loading on the wind turbines.

Power derating presents another solution towards wind farm power output increase (Barth et al. [2007]). It is based on the concept of wind turbines in the first row of a wind farm operating at a lower electricity generating level to limit the wind deficit behind the first row of wind turbines so that downstream wind turbines experience more energized wind and the wake effect is limited. Barth and al. expected a 4.1% total power output increase for two wind turbine rows downwind of the upwind row of turbines and 0.7-3.9 % for wind turbines in rows 5 to 9 of the wind farm. Taking into consideration wind variability, these values tend to be a little lower practically.

1.4.2 Novel External Solutions

Below, some novel techniques are described that apply external objects (like wings) to increase turbulence and/or steer the unaffected wind boundary layer partially into the wake. These ideas are considered novel, but they are all based on the vertical entrainment (mixing of different wind layers vertically) of wind in wind farms which is a topic that has been a focus of multiple researches already. This vertical entrainment of wind describes how wind at higher altitudes has a higher velocity and thus, if brought down into the wake, can re-energize the wake strongly. Often this results from mixing the boundary layers; or turbulence. Calaf et al. [2010] applied CFD modelling to support a concept described by many researchers that this vertical entrainment of the wind can be in the same order as the wind deficit at the rotor. This also adds towards the findings shown before that for the fourth wind turbine row and onwards only wind from the unaffected boundary layer re-energizes the wake further downstream.

VerHulst and Meneveau [2015] were among the first researchers to apply some external machine or device that lays an additional force on the unaffected wind stream to re-energize the wake. Not yet designing a specific device, this research was meant as a proof-of-concept for increasing vertical entrainment using hypothetical synthetic forcing. In future studies, like this one, specific methods of increasing the vertical entrainment of wind in wind farms should be further investigated. Verhulst et al. concluded that power values could increase with 5% for realistic loading values, while for extreme cases (likely unobtainable loading) power increases up to 95% were found.

On the basis of these theoretical considerations, Bader et al. [2018] proposed the application of airfoils to redirect the wake of the upstream turbine in a downward, causing wind from the unaffected layer to be directed downwards. This concept is further clarified in the two figures below: in Figure 1.5 without the use of the proposed airfoils, and in Figure 1.6 for the system using the proposed airfoils. Bader et al. used Reynolds-averaged Navier Stokes (RANS) in OpenFOAM to model the impact of different airfoil designs and concluded that up to 70-80 % of additional power could be achieved using this technique.

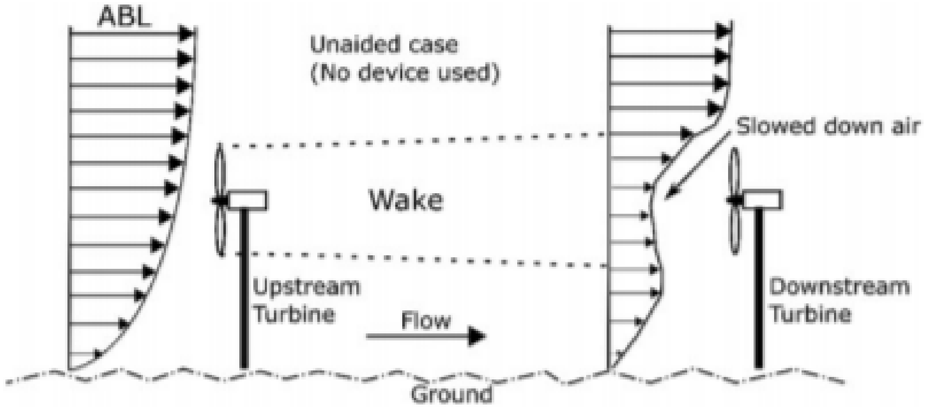

Figure 1.5: Unaided system or normal case of wake effects (Bader et al. [2018])

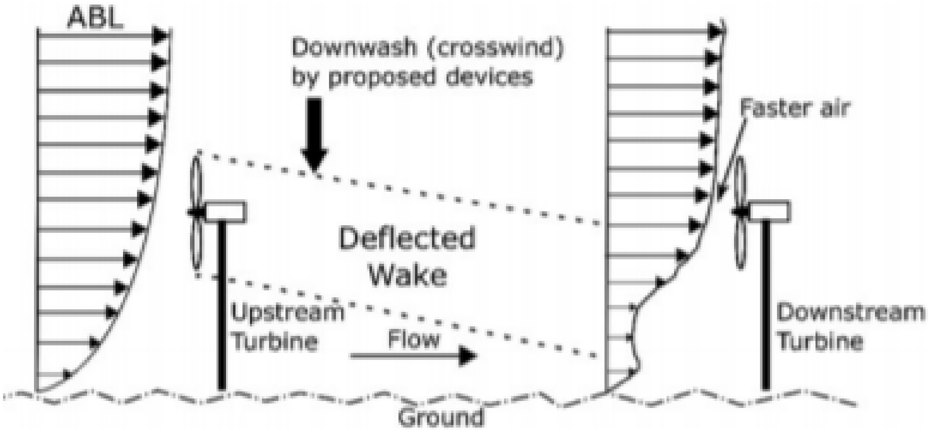

Figure 1.6: Aided system using proposed airfoils for wake steering (Bader et al. [2018])

1.5 RESEARCH ORIGIN

This study is based on the work of Evangelos Ploumakis under supervision of Wim Bierbooms (Ploumakis [2015]) and further investigates the potential of using kites to re-energize the wake by increasing the vertical entrainment of wind from the unaffected boundary layer into the wake. Ploumakis used Large Eddy Simulation (LES) modelling to simulate the turbulent wind flow in a small wind farm of 4 wind turbines in a row, and applied kites in between the four wind turbines to study the wind farm efficiency increase by re-energizing the wake.

Ploumakis based his research on a design that was introduced by a group of students (Boonman et al. [2011]) in the 2011 Design Synthesis Exercise at the Aerospace department of TU Delft. They proposed a bow kite system, as can be seen in Figure 1.7, to initiate a downwards velocity component into the wake between wind turbines. Their theoretical work produced promising results: with a large enough kite, wind farm efficiency increases up to 4% were attainable.

Ploumakis used CFD to simulate the proposition of the group of TU Delft students and compared modelling conclusions with their analytical calculations. His CFD results gave an efficiency increase value of 1-2% which was substantial lower than the analytical calculations but probably resulted from a smaller kite area used in the CFD model, and lower thrust coefficient. Ploumakis concluded however, that the promising results presented by the group of students were realistic and continued his research to find quantitative effects on the wake flow by choosing different kite sizes, turbine loading, and kite energy densities. Larger kite size and higher kite energy densities were observed to cause faster wake recovery and higher efficiency levels, while the overall benefit of a kite showed to be lower under optimal loading of the turbines (and higher for partial loaded wind turbines).

Figure 1.7: Proposed design for wind farm efficiency increase using a kite sytem to re-energy the wake (Boonman et al. [2011])

Because of the high computational costs of LES modelling, Ploumakis research was limited by a small number of simulations and did not contain any parameter studies (besides sizing). However, suggestions for future work were made. These suggestions included the optimisation of kite location, both downstream and in height, for different kite and wind turbine parameters. It is exactly these research propositions this study focuses on, and even goes further by studying multiple kite parameters.

1.6 SCOPE OF THIS WORK

In this work, the application of kites to increase wind farm efficiency by inducing vertical entrainment from the unaffected boundary layer in to the wake, will be further investigated. Using OpenFOAM, the effects of different kite parameters on wind farm efficiency will be studied. RANS will be used for modelling the wind flow and the Actuator Disc (AD) theory is presented to model the wind turbines. The kites will be modelled using the Actuator Line (AL) method. Various simulations will be run to illustrate the effects of changing turbine and kite parameters. Conclusions will be drawn and a roadmap for future work will be presented.

This work will consist of 5 phases:

1. Literature study of relevant work focusing on wind farms, kites, CFD and modelling of the three components of this study: the wind flow, the wind farm and the kites.
2. Learn from scratch how to use CFD and study methods to model the three components that make up the research simulation.

3. Model the wind boundary layer and the wind farm and quantify the wake effect losses.
4. Model the kite into the wind flow and wind farm model and set a base case for the optimization problem.
5. Change various parameters and assess for largest efficiency increase.

The main research question:

Using the AL model for kites, what is the optimal kite farm configuration in a four turbine wind farm and what wind farm efficiency gain can be achieved using this kite farm configuration?

1.7 OUTLINE

In Chapter 1 the problem description is given and the research goals are formulated. A first step of the literature study is performed by studying literature focusing on proposed solutions for the problem description this work focuses on. Chapter 2 continues with the literature study and describes the theoretical framework for kites. The concept of downwash is introduced. Chapter 3 introduces and describes key components of performing simulations using CFD. The process of a simulation in OpenFOAM (the CFD software used in this study) is explained in much detail through a step-by-step simulation case setup. In Chapter 4 first simulations are performed of the atmospheric boundary layer in an empty domain and of a 4 turbine wind farm using the same atmospheric boundary layer. Wind velocity deficit values are recorded and compared to literature. These simulations set the base for the parameter studies done in Chapter 5 to study the optimal kite farm configuration. 5 kite parameter studies are performed and the optimal kite farm configuration is explored. The wind farm efficiency gain is presented using this optimal kite farm configuration. Chapter 6 discusses the results, listing the limitations and most important findings of this work. In Chapter 7 the conclusions of this study are drawn and the main research question is answered.

2 KITE THEORY

The principle of kites has been used already since early history. In Asia kites played a traditional role in cultural celebrations whereas from the 16th century onwards, in Europe, kites were used to conduct experiments at high altitude. Flying a kite connected to a metal tether into a thunderstorm, Benjamin Franklin proved in 1750 that lightning was in fact electricity. Alexander Wilson and Thomas Melville first measured a temperature gradient with increasing height using kites (1749) (American Kitefliers Association [2021]). More recently, the 1973 oil crisis sparked a renewed interest in kite technologies as a purpose for renewable energy generation. The reason: with higher altitude comes higher wind speeds, and more importantly, a more robust wind flow (steadier during both day time and night time). This inspired researchers to study different methods of electricity generation using kites which resulted in the two best known concepts of airborne wind energy, both based on the work of Loyd (1980) (Bauer et al. [2018]): Flight-gen wind energy and Ground-gen wind energy.

Flight-gen wind energy is based on a plane or kite flying at high elevation in crosswind motion which enables the system to experience much larger wind speeds than experienced at wind turbine hub height, requiring smaller engines and turbines to generate a similar amount of power. Figure 2.1a shows the basic principle of a flight-gen system where the system is connected to the ground using electric conductive tethers to transport the electricity generated by the system through the tether to the ground. It is named a flight-gen system because all of its electronic components are located on the system in the sky. This immediately results in its largest disadvantage: the mass of the system increases and failure of the system may result in large economic losses.

Unlike a flight-gen wind energy system, a ground-gen wind energy systems has all its electronic components located on land. The plane or kite is now connected with a non-conductive (and therefore lighter weight) tether and is slowly reeled out from a drum, as shown in Figure 2.1b. As the system is reeled out with a controlled speed, the system experiences a traction force on the drum which is connected to a generator and thus results in electricity generation. Steering the flying system faced straight into the wind flow, when fully reeled out, enables the system to be reeled in with a much lower force, than is measured when reeling out. This presents the result of a net positive power generation.

Even though the present study does not focus on power generation using these wind energy systems, the work of Loyd does address the effects of

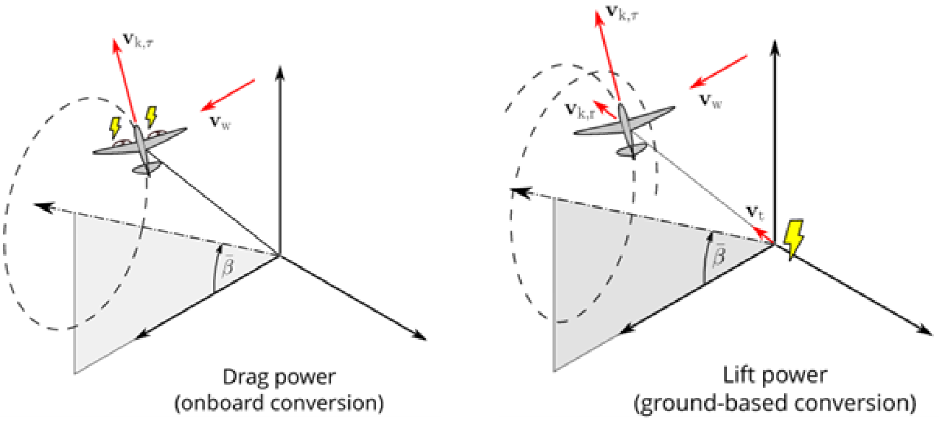

(a) (b)

Figure 2.1: Two types of High Altitude Wind Energy (a) Fly-Gen Wind power (b) Ground-Gen Wind Power (Schmehl, R [2019b])

kites, or other flying rigid bodies, on the wind flow. Specifically it lays the foundation for the so-called principle of 'downwash' which is the change in wind flow direction that bends the wind flow downwards, for example into the wake of a wind turbine. This is the desired effect of re-energizing the wake, and this chapter provides the theoretical background to the principle of 'downwash'.

2.1 BASIC PRINCIPLES

To understand the principle of downwash first some basic terminology must be addressed. For a static kite, force analysis provides 3 fundamental forces that describe the behaviour of a kite with Kite mass (m_k), shown in Figure 2.2. Kites come in many different forms and sizes but these fundamental forces are for all kites the same. Lift (L) and Drag (D) are the main force components on a wing and are presented in equations 2.1 and 2.2. Following Bernoulli's equation, lift pushes air up opposing the effect of gravity. Drag slows the air down and acts as a friction force opposing the wind speed. Lift and drag are force components of the resultant force experienced by a flying body: the Aerodynamic Force (F_a). The mass of the kite enforces a Gravitational Force (F_z) and the kite experiences a Tether Force (F_t) that prevents the kite from flying away. In static conditions, thus during force equilibrium, F_a equals the sum of F_z and F_t.

$$L = F_L = 1/2\rho C_L (v_a)^2 S \tag{2.1}$$

$$D = F_D = 1/2\rho C_D (v_a)^2 S \tag{2.2}$$

$$F_a = \sqrt{L^2 + D^2} \tag{2.3}$$

$$F_t = F_a - F_z \tag{2.4}$$

where ρ is the Density (ρ) of air, C_L is the Lift coefficient (C_L), C_D is the Drag coefficient (C_D), S is the Kite surface area (S) and v_a is the Apparent wind velocity (v_a). v_a is the wind that is 'felt' by the kite and often is not equal to the wind velocity. The effects of lift and drag on the wind speed tend to tilt the kite with an angle α, the Angle of attack (α). This angle represents the angle between the chord line and the relative wind speed, or often called apparent wind speed v_a as can be seen in Figure 2.3. Note that the flight path represents the apparent wind speed direction. Lift and drag strongly depend on the angle of attack as the lift and drag coefficient are directly affected by the angle of attack. Lift increases up to a critical angle of attack where flow separation, stall, takes place as can be seen in Figure 2.3. Drag increases with angle of attack.

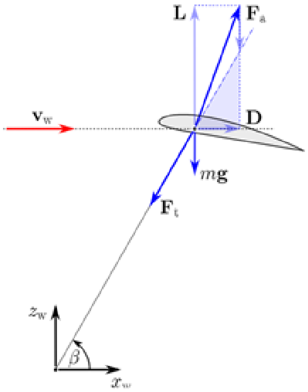

Figure 2.2: Static kite force analysis (Schmehl, R [2019a])

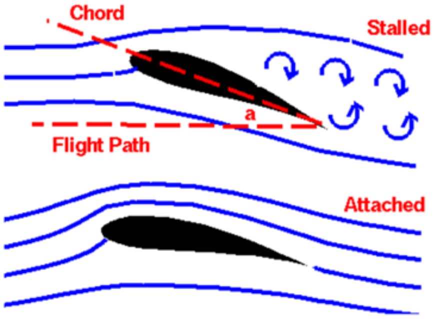

Figure 2.3: Wake flow dependence on angle of attack (Hall, N [2018])

2.2 3D WIND BEHAVIOR

A kite with a finite geometry experiences two different air pressures under and above its body. Above the kite, because of increased wind speed, a lower pressure area is found while the decreased wind speed underneath the body of the kite results in a higher air pressure. At the tips of the wing, wind is enabled to flow from the higher pressure area to the lower pressure generating a pair of counter-rotating vortices as can be seen in Figure 2.4. These vortices change the wind speed and direction and cause an additional velocity generated downwards named downwash. This velocity is experienced strongest at the wing tips and decreases along the span of the kite until the wing root as can be seen in Figure 2.5.

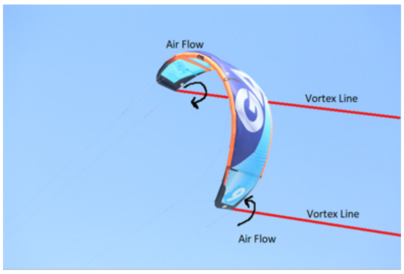

Figure 2.4: Visualisation of vortices generated by a kite.

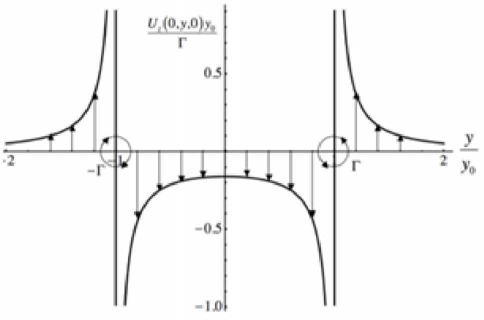

Figure 2.5: Downwash wind velocity profile (Schmehl, R [2019a])

Downwash decreases the effective angle of attack because the apparent wind speed is tilted slightly generating a so-called induced angle of attack that is subtracted from the effective angle of attack. In force analysis, this decrease in effective angle of attack results in an additional force component that decreases the wind speed by acting as a friction force. This force is called the induced drag or drag due to lift. As downwash is stronger at the wing tips and decreases in effectiveness near the kite's root, the angle of attack alters along the span of the kite as well. Analysis (Gilbert, L [2011]) on this change in angle of attack and the additional force component (induced drag) results in loss of the lift coefficient. Assuming kites have a low Aspect Ratio (AR) a final equation can be obtained for the final lift coefficient including the effects of downwash and induced drag.

$$AspectRatio = AR = b^2/s \tag{2.5}$$

$$C_l = C_{l0}/(1 + C_{l0}/(\pi AR)) \tag{2.6}$$

where: b is the wingspan (b), S is the surface area of the kite, and C_{l0} is the Basic Free Stream Lift Coefficient (C_{l0}).

Momentum theory of lift can be addressed to find an expression relating the downwash velocity, the coefficient of lift and the aspect ratio, illustrated in Figure 2.6. This theory first assumes that the angle between the Free stream wind speed (V) and the Downwash velocity (w) is small and can be approximated by formula 2.7. Combining this formula with force and momentum theory yields two final expressions for Downwash angle (ϵ_{dw}) relating the downwash angle to induced angle of attack and the coefficient of lift.

$$\epsilon_{dw} = \arctan(w/V) \tag{2.7}$$

$$\epsilon_{dw} = 2\alpha_i \tag{2.8}$$

$$\epsilon_{dw} = 2C_L/(\pi AR) \tag{2.9}$$

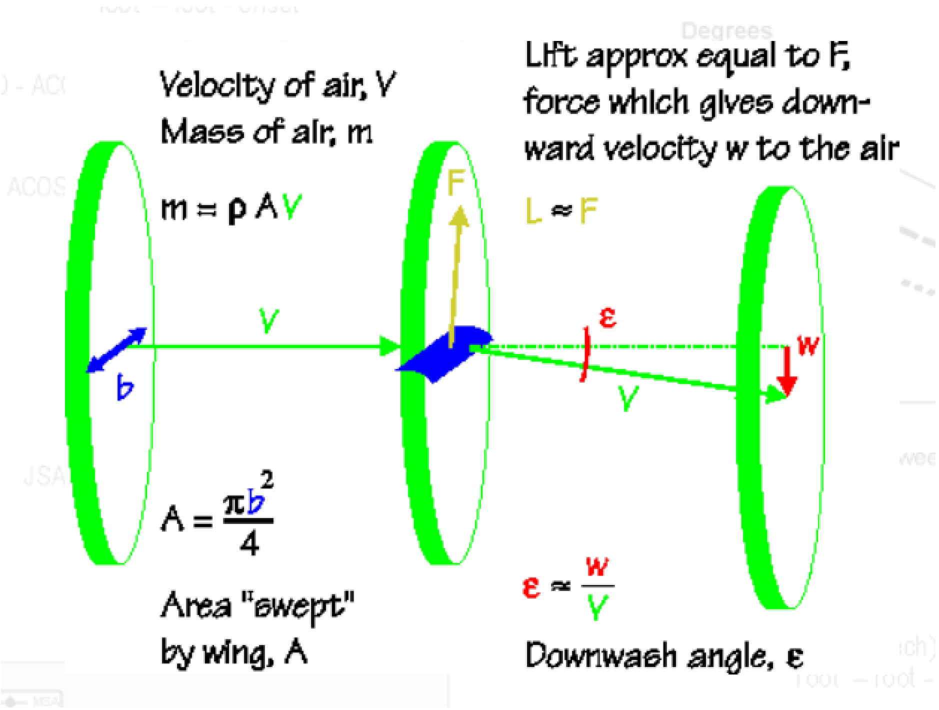

Figure 2.6: Sketch of downstream velocity resulting from force analysis (Gilbert, L [2011])

Combining equations 2.7 and 2.9 yields an expression for downwash wind speed velocity w under the assumption of having a small angle between w and free stream wind speed V.

$$w = 2C_L V/(\pi AR) \tag{2.10}$$

Equation 2.10 presents some interesting theoretical results for downwash. Downwash can be increased by maximising the lift coefficient in which the kite is operating. Furthermore, downwash is most effective for kites with low aspect ratio. For this reason, kites with a small aspect ratio are considered in this study. (Jerez Venegas [2017])

3 COMPUTATIONAL FLUID DYNAMICS

We live in a world in motion, where every movement interacts with fluids. Changes in our world get shaped by fluid dynamics, driving the interest in studying fluid flow. However, the continuum equations, describing the motion of fluids, are very complex and up until now no analytical solution has yet been discovered. Experimentally measuring fluid flows around a large object draws a few problems as well. The main issue is that, in the wind tunnels used for experiments, controlled similar conditions should be obtained that resemble the practical flow in every day life accurately. These wind tunnels are multiple factors smaller than the practical applications, like rocket engines, off-shore wind farms, and so on. Thus, huge wind tunnels are required to experimentally measure the wind flows around these large geometries which is very expensive, complicated and sometimes even dangerous. For that reason, CFD has been introduced as an attractive alternative to study the details of particular fluid dynamics phenomena of these large geometries in controlled similar conditions using numerical analysis. (Note that smaller scaled experiments using scaling factors has been used as a method for experimentally measuring fluid flows and validate results from CFD simulations already widely.)

CFD focuses on splitting a big problem into many smaller problems which can be solved numerically or by hand much easier. Together, these results can be combined to solve the initial big problem. This was first introduced by Lewis F. Richardson in 1922 (Vulpiani [2014]) who tried to model Europe's weather system and provided a weather prediction by means of discretizing Europe as a chess board and solving the fluid dynamics by hand for each 'chess board tile'. His results diverged and both turbulence and wrongful chosen initial conditions were concluded, much later, to be the result for this problem (Richardson [2007]).

In more recent years a general method has been provided for studying fluid flow with CFD, presented in Figure 3.1. In this work, a similar approach is followed and will be discussed in this chapter. First, the physical model is defined: for example the wind flow around a wind turbine. The equations describing wind flow, the mathematical model, are listed and the simulation domain is set. These equations consist of differential equations that need to be modelled using a turbulence model. Parameters and dimensionless numbers that are involved in these equations are listed. Next, this mathematical model is discretized both in time and space to generate the so-called algebraic model, which is the boiled down model run by the solver. The user-selected solver solves the algebraic model from grid node to grid node using an implicit or explicit method. The solutions are visualised and conclusions may be drawn. Section Section 3.1 addresses the governing equations of CFD. Section Section 3.2 introduces the different turbulence models and describes the turbulence model used in this thesis in more detail. Section Section 3.3 explains the process of spatial and temporal discretization. Finally Section 3.4 introduces the CFD software used in this work initiating Chapter 4 in which the wind flow and wind farm are modelled and some first power output and efficiency results are studied.

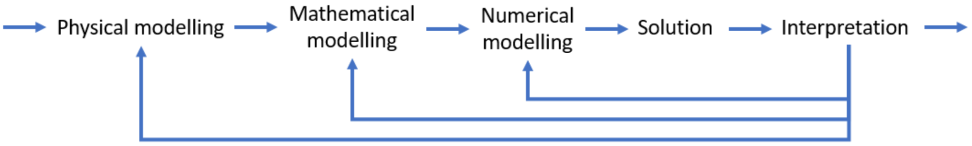

Figure 3.1: Structure of studying fluid flows using CFD. This structure describes the most common method, including cycle loops, of doing research using CFD.

3.1 PHYSICAL MODEL

Fluid flow, like the wind, is described with the use of continuum equations (Flandro et al. [2011a]) that are based on the fundamental law that mass, momentum and energy is conserved during transport of matter in a closed system. Balance equations for mass, equation 3.1, momentum, equation 3.2, and energy, equation 3.3, provide the tools to study these fluid flows. All three equations can be provided in integral or differential form, using divergence forms (Hickel, S [2021]).

$$\frac{\partial \rho}{\partial t} + \nabla \cdot \rho \underline{u} = 0 \tag{3.1}$$

$$\frac{\partial \rho u_j}{\partial t} + \frac{\partial \rho u_i u_j}{\partial x_i} = \sum_n F_{n,j} \tag{3.2}$$

$$\frac{\partial (\rho E)}{\partial t} + \frac{\partial \left(u_i \rho E\right)}{\partial x_i} = -\frac{\partial u_i p}{\partial x_i} + \frac{\partial u_i \tau_{ij}}{\partial x_i} - \frac{\partial q_i}{\partial x_i} + u_i \rho f_i \tag{3.3}$$

where ρ represents the density of the fluid $[kg/m^3]$, t represents time (t), $\underline{u}$ represents the velocity in 3 dimensions [s] ($\underline{u}$), $\sum_n F_{n,j}$ presents sum of all external forces [N] ($\sum_n F_{n,j}$), E presents the internal energy [J] (E), p is the pressure [Pa] (p), τ_{ij} is the shear stress tensor (τ_{ij}), q_i equals the heat flux $[W/m^2]$ (q_i) and f_i presents the body force per unit mass [N/kg] (f_i).

These equations are highly general and can be further simplified for our purposes while still describing wind flow sufficiently. (Flandro et al. [2011a]) Specific assumptions can be made based on two dimensionless numbers that are introduced below. The Mach number (Ma), equation 3.4, defined as the ratio of the advection velocity of the object or flow compared to the speed of sound and is a measure of the compressibility of a flow. If the Ma number is low (<0.3), incompressible flow can be assumed which is the case in wind dynamics where the wind speed very rarely touches the 0.3 barrier of the speed of sound. The Reynolds number (Re), equation 3.5, describes the ratio of the inertial forces over the viscous forces. High Re wind flow present inviscid flows where viscosity effects may be neglected Flandro et al. [2011b].

$$Ma = \frac{U_0}{c_0} \tag{3.4}$$

$$Re = \frac{\rho_0 U_0 L}{\mu} \tag{3.5}$$

where U_0 represents the advection velocity [m/s] (U_0), c_0 represents the speed of sound [m/s] (c_0), L represents a characteristic length for the flow [m] (L) and μ is the dynamic viscosity of the fluid (μ).

For our practical problem of wind flow in a wind farm situation, we can assume a high Re and low Ma number. This greatly simplifies Eqs 3.1-3.3: the energy balance directly follows from the momentum balance and density and viscosity can be assumed constant. The set of continuum equations result in the Navier-Stokes equations (N-S equations) for an incompressible fluid with constant density and constant viscosity, equation 3.6 (Anderson JR [2009]).

$$\left.\begin{array}{c} \frac{\partial \underline{u}}{\partial t} + \nabla \cdot (\underline{u}\underline{u}) + \frac{1}{\rho}\nabla p - \frac{1}{\mathrm{Re}}\nabla \cdot \nabla \underline{u} = 0 \\ \nabla \cdot \underline{u} = 0 \end{array}\right\} \begin{array}{l} \text{incompressible fluid} \\ \text{with constant density} \\ \text{and constant viscosity} \end{array} \tag{3.6}$$

An important term in the N-S equations is the $\nabla \cdot (\underline{u}\underline{u})$ term that represents the non-linearity term of the N-S equations. Non linear partial differential equations can in general not be solved analytically (except for creeping flows with very low Re) and therefore numerical models need to be used to solve these equations and study the dynamics of fluids. In Section 3.2 the best known turbulence models that solve the N-S equations by modelling the non-linear term are described and some advantages and disadvantages are listed.

3.2 MATHEMATICAL MODEL

3.2.1 Turbulence models

In Section 1.2.3 the different scales of vortices, also called eddies, expected in wind flow around turbines, were discussed. The different turbulence models that are presented in this section partially depend on these different scales of turbulence. Five of the most used turbulence models that partially or fully model turbulence are listed below.

DNS

Direct Numerical Simulation (DNS) computes the 'exact' solution by requiring no further assumptions and solve the N-S equations for all flows. All length and time scales of turbulent flow can be computed and the full flow can be studied. Even though this turbulence model appears most preferable, the resulting high level of accuracy comes with great computational costs. The computational cost of DNS is proportional to Re^3. For high Re values, which is the case for wind flows in a wind park, this turbulence model should thus not be used. However, DNS solves the N-S equations using the most accurate method and is thus indispensable for turbulence research.

RANS

RANS (Reynolds-averaged Navier–Stokes) simulations focus on solving the N-S equations for the time-averaged flow, here called mean flow. All gradients and structures of the averaged flow are solved by decomposing the exact solution in a mean and fluctuating part, and studying the mean part of the solution. This turbulence method is less accurate, especially when studying specific vortical structures or eddies in a specific range of size. RANS is more promising for studying the overall effects of a wind flow or when modelling steady-state flows. The main advantage, compared to all four other models, is the low computational costs required for simulating flow in RANS.

URANS

Unsteady Reynolds-averaged Navier-Stokes (URANS) simulation uses the same methodology as RANS to solve a mean flow. However URANS is used for transient simulations and time is not averaged for the mean flow. URANS is used for studying flow solved with RANS that contain some slow unsteady effects.

LES

Large Eddy Simulation (LES) solves for the larger and more energetic vortices while modelling the smaller dissipative scales. LES uses a filtering kernel to filter out the smaller scales with respect to the grid scale. The remaining scales are then solved in the grid scale while the filtered out scales are modelled using a sub-grid-scale model. LES shows more accurate solutions for the larger vortices and is often used to study the vortical structures in wakes. LES involves moderately high computational costs, though cost independent of Re.

DES

Detached Eddy Simulation (DES) is a hybrid turbulence model that uses RANS to solve the N-S equations except for regions fine enough to allow for application of a sub-grid LES model. Resolution of the grid decides what turbulence model is used at what location and time of the flow. DES has the advantage that it does not require the intense computational effort of LES for the largest percentage of the domain, however the switching between LES and RANS cause additional problems that sometimes lead to diffusing modulation.

3.2.2 RANS

This study focuses on the overall power output increase (and efficiency increase) of a wind farm with the use of kites. For that reason, specific details of the wind flows and eddies are not the main interest and this work primarily focuses on the averaged wind flow. Therefore, we have selected the RANS approach to incorporate turbulence in our kite simulations. RANS has the additional advantage to be the least computational intense of all turbulence models. This allows multiple simulations to be run, and large parameter studies to be performed in this work.

As explained in Section 3.2.1 RANS solves for the time-averaged mean flow by decomposing all gradients and structures of the exact solution in a mean and fluctuating part around this mean, see equation 3.7 for wind flow u_i. Note that the triangular brackets present the averaged components.

$$u_i = \langle u_i \rangle + u_i' \tag{3.7}$$

Decomposing the N-S equations results in the Reynolds-averaged Navier-Stokes equations that describe the averaged fluid flow of any process, like the wind flow through a wind farm.

RANS uses this decomposition technique to decompose all components of the N-S equations into its Reynolds Averaged components resulting in the RANS equations. Equation 3.6 gives the N-S equations for an incompressible fluid with constant density and constant viscosity. By substitution of the wind flow as the sum of an averaged flow and a fluctuating part into Eq. 3.6, the following formula is obtained:

$$\begin{gathered}\frac{\partial \langle \underline{u} \rangle}{\partial t} + \nabla \cdot (\langle \underline{u} \rangle \langle \underline{u} \rangle) + \frac{1}{\rho} \nabla \langle p \rangle - \frac{1}{\mathrm{Re}} \nabla \cdot \nabla \langle \underline{u} \rangle = -\nabla \cdot \langle \underline{u'u'} \rangle \\ \nabla \cdot \langle \underline{u} \rangle = 0 \\ \text{Reynolds stress tensor } \tau_{ij} = -\left\langle u_i' u_j' \right\rangle \end{gathered} \tag{3.8}$$

Formula 3.8, just like the NS equations presents a new problem through the Reynolds stress tensor, describing the non-linear term in the upper equation. This Reynolds stress tensor is a new component that can not be solved algebraic. This problem is simplified using an approximation for the Reynolds stress tensor. The most commonly applied turbulence model in RANS studies is the eddy viscosity model that approximates the Reynolds stress tensor using equation 3.9.

$$-\left\langle u_i' u_j' \right\rangle \cong 2 v_T S_{ij} - \frac{2}{3} \delta_{ij} k \tag{3.9}$$

where v_T is the eddy viscosity (v_T), S_{ij} is the strain rate (sij), δ_{ij} is the Kronecker delta function (dij) and k is the turbulence kinetic energy. Using this expression in the RANS equations yields a modeling problem that shifts from many unknowns to only one scalar field: the eddy viscosity.

The eddy viscosity strongly depends on the mean velocity field. Different models to numerically model the eddy viscosity have been used over time. Generally, the two-equation models (where two denotes the amount of transport equations required) provide the most accurate representation for the eddy viscosity. For RANS modelling the Jones and Launder k-ϵ model is selected most often for external flows far from the walls of the domain (as is the case in this research) and estimates the eddy viscosity using equation 3.10, and its relevant transport equations for k and the ϵ in equations 3.11 and 3.12 (Hickel, S [2021]).

$$v_t = C_D \frac{k^2}{\varepsilon} \tag{3.10}$$

$$\frac{\partial k}{\partial t} + \underbrace{\langle u_j \rangle \frac{\partial k}{\partial x_j}}_{\text{Advection}} = \underbrace{\tau_{ij} \frac{\partial \langle u_i \rangle}{\partial x_j}}_{\text{Production}} + \underbrace{\frac{\partial}{\partial x_j} \left(\left[\frac{1}{\mathrm{Re}} + \frac{v_t}{\mathrm{Pr}_k} \right] \frac{\partial k}{\partial x_j} \right)}_{\text{Diffusion}} - \underbrace{\varepsilon}_{\text{Dissipation}} \tag{3.11}$$

$$\frac{\partial \varepsilon}{\partial t} + \underbrace{\langle u_j \rangle \frac{\partial \varepsilon}{\partial x_j}}_{\text{Advection}} = \underbrace{C_{\varepsilon 1} \frac{\varepsilon}{k} \tau_{ij} \frac{\partial \langle u_i \rangle}{\partial x_j}}_{\text{Production}} + \underbrace{\frac{\partial}{\partial x_j} \left(\left[\frac{1}{\mathrm{Re}} + \frac{v_t}{\mathrm{Pr}_\varepsilon} \mid \frac{\partial \varepsilon}{\partial x_j} \right) \right.}_{\text{Diffusion}} - \underbrace{C_{\varepsilon 2} \frac{\varepsilon}{k} \varepsilon}_{\text{Dissipation}} \tag{3.12}$$

with constants C_D is 0.09, $Pr_{epsilon}$ is 1.3, Pr_{kappa} is 1, $C_{\varepsilon 1}$ is 1.44 and $C_{\varepsilon 2}$ is 1.92.

3.3 NUMERICAL MODEL

In the previous chapter the physics and corresponding mathematical equations describing wind flow including turbulence were defined. The resulting Navier Stokes equation now needs to be solved in space and time for the given geometry of a series of wind turbines and kites. Since an analytical solution is out of reach, these equations will be solved numerically using CFD. The standard approach is to represent space as a set of discrete points (mesh), to assign average properties to these points and solve the discretized N-S equations for these grid nodes. Since a computer can only perform algebraic operations, the partial differential equations will be transformed into discretized equations. Looking back at the N-S equations equations, equation 3.6, two partial derivatives (that need to be discretized) are considered: partial derivatives that consider 3D effects in space, and the first derivative of the velocity in time. This process of spatial and temporal discretization will be discussed further in the next sections.

3.3.1 Spatial Discretization

In this work, spatial discretization has been achieved through the Finite Volume (FV) method. Any flow domain can be divided into many non-overlapping volumes, the so-called finite volumes (FVs). A FV is considered homogeneous and has single average physical properties for the entire volume. A FV is represented by a single dot in the centre of the FV. Next, the earlier discussed conservation laws are evaluated over the FV. This is done by integrating the conservation laws over the FV, whereby the resulting volume integrals are rewritten as surface integrals (Gauss theorem). These surface integrals are numerically evaluated using approximation methods. The quadrature method approximates the surface integral of the fluxes using the mid-point rule (see Figure 3.2). However, before these surface integrals can be approximated, the fluxes need to be computed at all locations at the cell surfaces using spatial interpolation.

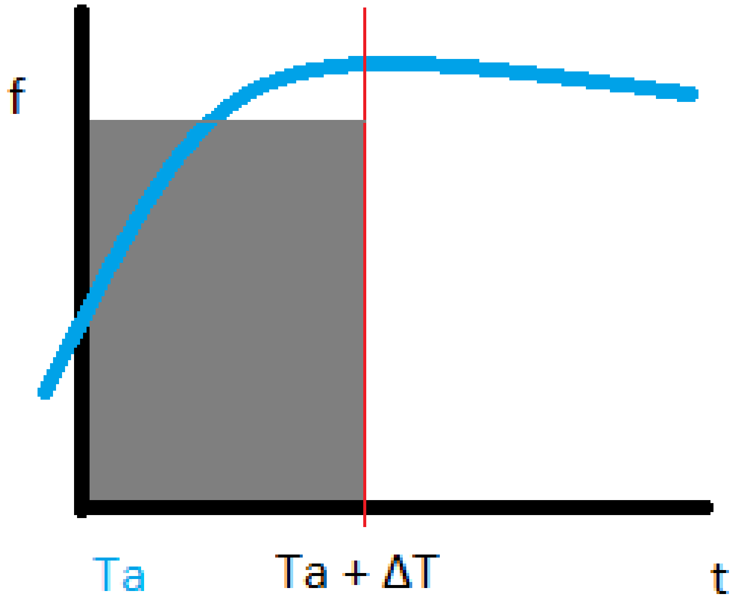

Figure 3.2: Midpoint rule for approximating the surface integrals. Integral is approximated by multiplying the midpoint of a function domain times the area of the cell face.

Two common methods for spatial interpolation are the Upwind Differencing Scheme (UDS) and Central Differencing Scheme (CDS). The main difference between these methods is that the UDS uses upwind variables to calculate the derivatives in the flow field, while the CDS uses the variables in the centre of the cell to provide the numerical solutions to the differential equations, and thus the fluxes.

Important for the numerical model is the generation of the grid, and the structure of the cells in this grid. Two types of grid structures, see Figure 3.3, are regarded for: the structured grid and the unstructured grid. A structured grid consists of cells that are similar in form, the amount of connections to other cells and in size relative to neighboring cells. An unstructured grid mostly consists of cells that have a distinctive amount of neighboring cells than other cells. This makes listing the different cells harder as there is no clear structure in the grid. Structured meshes are often more efficient and accurate, but are more costly because unstructured grid meshing can be done using automatic algorithms. Structured grid require user input and grid correction. Local grid refinement, the addition of more grid cells near areas of interest, is harder for structured meshes. A good grid should be filled up completely with cells while not overlapping, should be smooth (neighbor cells are relatively similar) and orthogonal (angle between phases of a cell should be small). Low resolution meaning large cells and a small total amount of cells in the grid result in large errors, while high resolution with much finer cells, and thus a larger amount of total cells, result in smaller errors. The problem however, is that finer meshes come with greater computational cost.

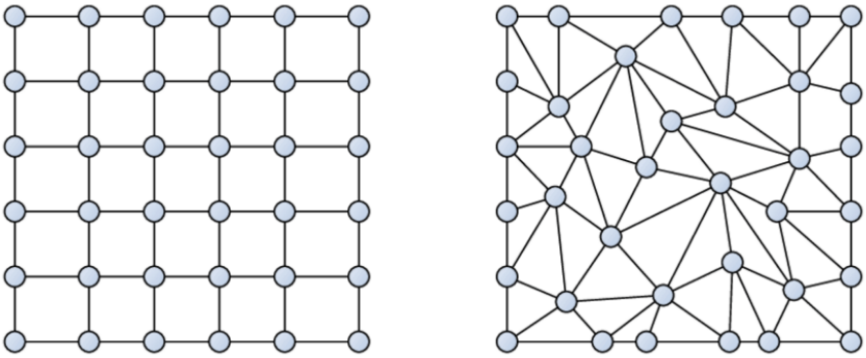

Figure 3.3: Grid structures. On the left a structured grid with a fixed number of neighbors for cells and vertices. On the right an unstructured grid in which it is clearly visible that some cells have a distinctive amount of neighboring cells for vertices (Aissa [2017])

3.3.2 Temporal discretization

When unsteady state problems are studied using CFD, time needs to be discretized aswell. Continuous time is then divided into discrete time values where again, like in spatial discretization, dividing into the smallest timesteps results in the most accurate flow description. This, however, brings great computational costs as a problem so a fine path should be found between computational costs and accuracy. 3 main discretization techniques for temportal discretization are used often: the rectangle rule, the midpoint rule and the trapezoidal rule.

As described in Section 3.2.2 RANS separates every variable in a time-averaged (mean) component and a fluctuating component. The fluctuating component is time-dependent however the integration in time yielding the RANS equations, makes the set of equations fully independent of time. This is a big advantage of using RANS as a turbulence model because it eliminates the time dependence of the N-S equations which is an important reason why RANS is a computational inexpensive turbulence model.

3.4 OPENFOAM

CFD has been widely applied for many engineering applications in a wide variety of industries. Simulating rotating objects like hydro turbines (Tiwari et al. [2020]), predicting heat flows in buildings (Sakai et al. [2008]) and studying wakes in wind farms (Stergiannis et al. [2016]) are only some of many research papers of which results have come from CFD. There are many commercial and non-commerical software packages available for CFD modelling to simulate and numerically solve fluid flows in these different industries. One of the most widely used open source and free package is CFD software OpenFOAM. OpenFOAM is open-source software with the advantages of direct access to the source code, whilst being free of charge and for everyone to use. These advantages resulted in a rapid increasing community that solved OpenFOAM's main issue of having no real user support. In this work, OpenFOAM's mesh generator BlockMesh, and solver SimpleFOAM, explained in more detail in Section 4.1.3, is used for simulating the ABL, the turbines and the kites. Paraview, a programme often used in combination with OpenFOAM is used for post-processing the results (Weller et al. [1998]. *Note: This article presented the first introduction of FOAM to be used for CFD programming. OpenFOAM has been found by a wide community that worked together to develop this new open-sourced software*).

4 WIND FARM MODEL

In this chapter the starting point for the numerical evaluation of the effects of kites on the wake flow in wind farms is discussed. Prior to modelling kites, a wind farm model needs to be constructed. This is done by applying the CFD software OpenFoam. Before an actual windfarm is modelled, first we build a model of the empty domain, i.e. an empty grid including the effects of the so-called atmospheric boundary layer (ABL). Next, wind turbines, modelled through the actuator disc (AD) method are implemented in the empty domain and results are compared with literature. Power and efficiency calculations are done to establish values for the base case model, so without kites. Next, these values are compared to literature, so that the base case model is representative for the final step, i.e. numerical simulations including the implementation of a kite model. Finally results from the ABL and wind farm simulations are discussed and conclusions are drawn paving the way for the kite simulations in the next chapter.

4.1 ATMOSPHERIC BOUNDARY LAYER SIMULATIONS

4.1.1 Atmospheric boundary layer theory

The atmospheric boundary layer

The ABL is the lower part of the atmosphere and specifically defined as the part that is affected the most by the Earth's surface. The ABL interacts with the earth surface on the shortest timescales (of up to 1 hour) and is estimated to be up to 1 to 2 kilometers thick on average (Stull [1988]). Surface roughness of the earth boundary may cause turbulent behaviour in the ABL. This turbulence remains localised in the ABL and is prevented to escape by a so-called capping inversion illustrated in Figure 4.1. A capping inversion is the result of the normal temperature profile (cold air layer above warm air) being reversed. This creates a layer of cold air sitting below lighter, warm air, and is located above the ABL.

Stability conditions

The ABL can be characterised by three conditions: stable-, unstable- and neutral stability, depending on the level of vertical motion of air due to temperature gradients over height. Atmospheric stability is defined as the resistance of the atmosphere to vertical motion. The effects of stability is explained through the parcel method, in which an air parcel in an atmosphere at rest experiences a small displacement. Unstable behavior favors and increases the vertical motion of the air parcel while stable behavior resists it. Under

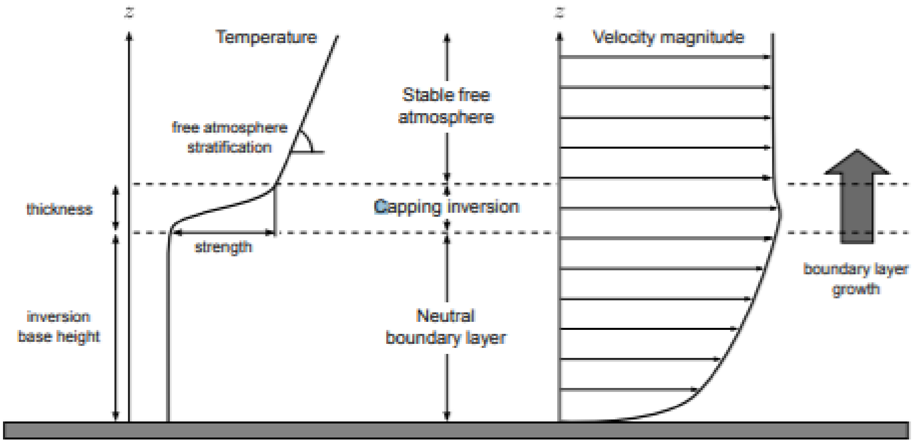

Figure 4.1: Potential temperature and velocity profile as a function of height in the conventionally neutral boundary layer (Allaerts and Meyers [2014])

neutral behavior, the atmosphere minimally affects the vertical motion of the air parcel by neither favoring, nor resisting it. To determine the stability situation of the ABL the so-called Adiabatic Lapse Rate (ALR) is compared to the temperature lapse rate of the air parcel. The ALR is defined by the temperature decrease over height due to compression or expansion in an adiabatic process (e.g. no heat is transferred from and to the air parcel). A distinction can be made between the dry ALR for unsaturated air, and saturated ALR for air saturated with water vapour.

The dry ALR equals 9.8 K/km (= 9.8 [°C/km]) and can be compared to the actual (measured) temperature lapse rate (atmospheric lapse rate) to determine stable, unstable or neutral conditions. For neutral stability the temperature laps rate equals the dry ALR meaning that air parcels in neutral conditions will not experience the ABL to favor nor resist the vertical motion of the air parcel. If the actual lapse rate is less than the ALR, an air pocket moving down will become warmer than the surrounding air, and hence will move up. Similarly an air pocket moving up cools to lower temperatures than its surrounding, and will move down. Vertical motion and turbulence is thus suppressed, hence stable conditions. The air parcel eventually returns to its original position. With similar arguments it can be explained that if the actual lapse rate is larger than the ALR, vertical movement and turbulence is favoured resulting in unstable atmospheric behaviour (see Figure 4.2 for a graphical illustration). If saturated air is considered, the atmospheric lapse rate is compared to the saturated ALR.

Wind shear

Wind shear under different stability conditions is described using Monin-Obukhov similarity theory. A central result of this theory is an expression for the average wind speed at a given height (Eq 4.1).

$$u(z) = \frac{u_*}{\kappa}\left[\ln\left(\frac{z}{z_0}\right) - \Psi\left(\frac{z}{L_{obh}}\right) + \Psi\left(\frac{z_0}{L_{obh}}\right)\right] \tag{4.1}$$

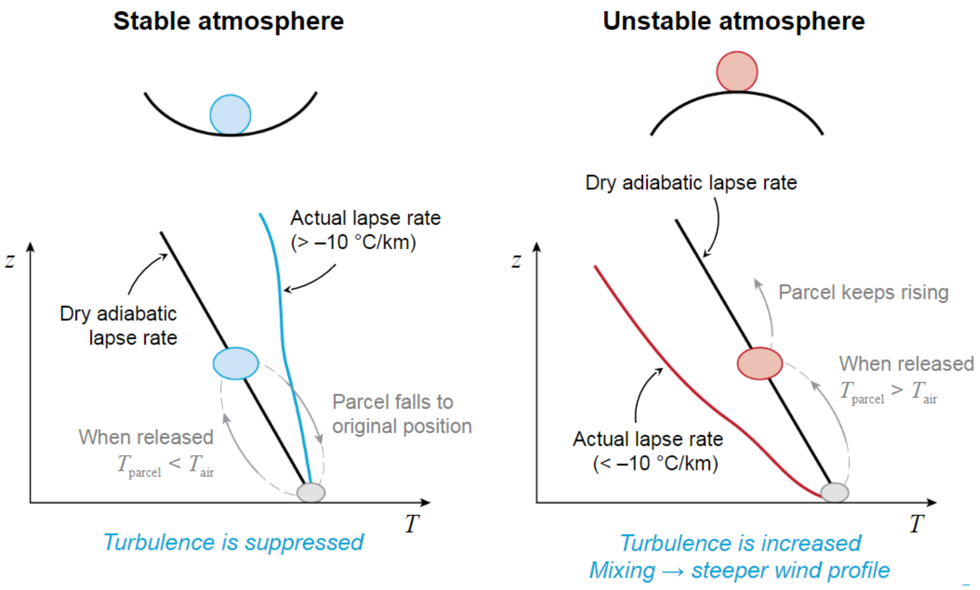

Figure 4.2: Stable and unstable behavior of the atmosphere and comparison of the atmospheric ALR to the dry ALR (Bierbooms, W [2020])

where u(z) is wind speed at height z (u_z), u_* is the friction velocity (u_*), κ is the von Karman constant (κ), z_0 is the surface roughness value (z_0), Ψ is a stability correction function (Ψ) and L_{obh} is the Obhukov length (L_{obh}) (Holtslag et al. [2014]).

Assuming neutral conditions, the stability correction function and Obhukov length can be left out reducing the complex equation to a simple logarithmic expression:

$$u(z) = \frac{u_*}{\kappa} \ln\left(\frac{z + z_0}{z_0}\right) \tag{4.2}$$

In this work, neutral conditions are assumed in order to simplify the problem. Without these assumptions, additional computational costs would slow down the simulations as additional equations (presented in formula 4.1) need to be considered and solved for every grid node.

Often, an alternative wind profile law is used to estimate wind velocity values at increasing height. This alternative law is named the wind profile power law and is shown in formula 4.3 where $u\left(z_{ref}\right)$ represents the reference wind speed at height z_{ref} (u_{ref}) and n represents the Hellman exponent (n).

$$u(z) = u\left(z_{ref}\right)\left(\frac{z}{z_{ref}}\right)^n \tag{4.3}$$

In a recent study by Emeis and Turk [2007], it was concluded that the power law (4.3) only approximates the log law relation of equation 4.2 in stable conditions or in neutral conditions for very smooth surfaces. For neutral and unstable conditions the log law wind profile (equation 4.1) approximates the physical wind profile layer more accurately than the power law, up to a height of about 100 meters. Above 100 meters, both wind profile layers can be used for reasonable estimations of wind speed at heights up to 1000 meters. Above 1000 meters high, geostrophic wind speed profiles should be studied, which use different velocity wind profiles. As the wind turbines and kites will not be located at heights greater than 160 [m], the log law relationship (equation 4.2) for the wind profile is used in this study (as is describes the ABL more accurately in the first 100 [m]).

4.1.2 Atmospheric boundary layer in OpenFOAM

The atmBoundaryLayer class

For numerical modelling of the atmospheric boundary layer, OpenFOAM provides a base class for handling the inlet boundary conditions for wind velocity and various turbulence quantities (Nagy, Jozsef [2021]). It caters for log-law boundary conditions for wind velocity, turbulent kinetic energy (k), dissipation of turbulent kinetic energy (ϵ) and the specific dissipation rate (ω). Together, this class provides a set of boundary conditions that simulate the turbulent atmospheric boundary layer. The specific dissipation rate (ω) is the rate at which the turbulent kinetic energy is converted into thermal energy and has units s^{-1}. In OpenFOAM it is expressed differently, using equation 4.4 because no strict mathematical definition of the specific turbulence dissipation exists (Nagy, Jozsef [2021]). (Note that ω also contains a constant, however this is implemented in OpenFOAM in the source code for the different turbulent methods.)

$$\omega = \frac{\epsilon}{k} \tag{4.4}$$

In Section 3.2.2 the turbulence model RANS was introduced and the concept of using two-equation models, with a focus on the k-ϵ model, to numerically solve for the eddy viscosity was described. Now we will numerically solve the N-S equations equations using the inflow boundary conditions for the velocity, turbulent kinetic energy and the dissipation of turbulent kinetic energy (described above). The functions for these boundary conditions are presented in formulas 4.5-4.7 (OpenFOAMltd [2007]).

$$\begin{aligned} u &= \frac{u^*}{\kappa} \ln\left(\frac{z - d_z + z_0}{z_0}\right) \\ v &= w = 0 \end{aligned} \tag{4.5}$$

$$k = \frac{(u^*)^2}{\sqrt{C_\mu}} \sqrt{C_1 \ln\left(\frac{z - d_z + z_0}{z_0}\right) + C_2} \tag{4.6}$$

$$\epsilon = \frac{(u^*)^3}{\kappa\,(z - d_z + z_0)} \sqrt{C_1 \ln\left(\frac{z - d_z + z_0}{z_0}\right) + C_2} \tag{4.7}$$

where d_z is the ground-normal displacement height (d_z) and the constants C_1, C_2 and C_μ represent fitting constants. d_z sets the ground height of the domain. In the case of this work, the ground is set at a height of 0 [m], resulting in d_z equals 0.

In this work the k-ϵ two equation model is used so ω is not included in the atmBoundaryLayer class. The curve-fitting coefficients C_1 and C_2 are based on the findings of Yang et al. [2009]. In 1995, Versteeg and Malalasekera determined the first set of values for these constants by data fitting for a wide variety of different flows. They found that for larger domains of more than 1 wind turbine in RANS modelling that C_μ to be 0.09, C_1 to be 0, and C_2 to be 1. This reduces the log-law behavior of the turbulent kinetic energy and turbulent kinetic energy dissipation rate while still presenting trustworthy results (Versteeg and Malalasekera [1995]). Since then, different research groups have set different inflow boundary conditions as presented for example in the work of Yang et al (Yang et al. [2009]). However, these newer works focus specific applications whereas the original work by Versteeg and Malalasekera is fine tuned for flows in larger domains with less flow separation which is the case in this study. For this reason, the values given by Versteeg and Malalasekera are used in this work.

Traditional values for the North Sea region were used as inputs for the log-law velocity relationship parameters. Coelingh et al. [1998] measured a u_{ref} around 7.8 [m/s] in the area of IJmuiden close to the Dutch coast in the North Sea, at 18.5 m reference height (z_{ref}). Jrgen et al. [2001] presents different techniques for selecting a correct sea surface roughness factor (z_0). Different equations can be used to select an accurate surface roughness, however to prevent further complexity, the option of selecting a constant surface roughness factor of 0.0002, or 0.2 millimeters was chosen (which is a good estimation for a surface roughness factor over open water).

4.1.3 Atmospheric boundary layer case setup

Meshing

Prior to the actual simulation work, a grid must be selected describing the domain of the simulations. OpenFOAM's internal grid generator is called BlockMesh which is a multi block structured mesh generating tool. The domain is set by specifying the corners of the grid. Next, the grid cell spacing is defined setting the amount of grid cells (and thus its size) in the domain. Unlike the wind farm and kite simulations, no refinement is needed for the ABL simulations because no specific region in the domain is of more interest than another. Methods of refinement and the need for refinement will be further addressed in Section 4.2.3.

The ABL will first be simulated in an empty grid. To check the mesh for any issues, eg backflow, initially 3 different sized grids were created for the ABL simulations: a small sized grid (the s-grid), a medium sized grid (the m-grid) and a large sized grid (the l-grid), of which the latter will be used in the wind farm and kite simulations. The large sized grid is used in further simulations because of the spacing required between the wind turbines (500 [m]) and space required upwind and downwind of the first and final wind turbine (about 400 [m]). The selection for this spacing will be further discussed in Section 4.2.3.

In this study, the effect of objects (turbines) of 80 [m] wind turbine diameter (D_{wt}) in the atmospheric boundary layer are modelled. The model (grid) should be large enough, such that velocity and pressure changes to the ABL will be absorbed by the ABL in a lateral direction. On the boundary of our model, no significant effect of the turbines should be observable. From previous studies (Ploumakis [2015] and Avila et al. [2017]) it can be concluded that for 80 D_{wt} objects, an area of about 800m should be included in the model. Thus domain height (d_z) and domain width (d_y) are 800 [m]. The s-, m- and l-grid all have the same height and width. For the s-grid a domain length (d_x) of 800 [m] is set, for the m-grid a d_x of 2000 [m] and for the l-grid a d_x of 2400 [m] is set.

In a study by Ploumakis [2015], the required grid resolution has been evaluated. It was observed that for a body with diameter D, grid cells with 0.05D or smaller should be used to adequately model physical wind phenomena. With a wind turbine of 80 [m], grid cells of 4x4x4 [m] should be applied close to the turbines. Further away from the body, cells can be coarser. In this study, we have used 8x8x8 [m] cells as base grid cell size. Close to the turbines and kites, refinement of this grid has been applied. Cruz [2019] and Tabas et al. [2019] present similar reasoning for the choice of refinement. Their coarser grid cells are 2 times, or even 3 times larger than the desired resolution near the objects of interest. As is done by Tabas et al. [2019], for the wind farm and kite simulations, to prevent computational costs becoming too high, a lower grid cell resolution (than 8x8x8) will be used at regions of no interest, while refinement regions are introduced near the bodies of interest (turbines and kites).

OpenFOAM uses one final tool for grid generation which is called the simpleGrading tool. This tool is used to define the ratio between the last and first cell along an axis, as presented in Figure 4.3. This makes it useful when a specific part of the axis is more interesting than the other parts, and can thus be seen as some method of refining as well. In the empty domain for the ABL simulations, no refining is required and the simpleGrading values are set at (1, 1, 1) meaning that every cell along the axes has the same cell length in x-, y- and z-direction.

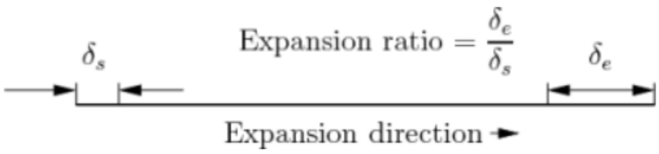

Figure 4.3: Concept of the simpleGrading tool (Greenshields, Chris [2018])

Together, the domain (in this case for the large domain size) is set using the following line of code:

```
blocks ( hex (0 1 2 3 4 5 6 7) (300 100 100) simpleGrading (1 1 1) );
```

where the block is formed using corners 0-7 and where the domain length, width and height are split into cells of 8x8x8 [m]. The total number of grid cells is in this case thus equals to 3 million grid cells. Figure 4.4 present the mesh of the largest sized domain: the domain used throughout this study. Table 4.1 presents an overview of the different domain sizes listing their domain lengths in x-, y- and z-direction, and the number of grid cells (N_{cells}).

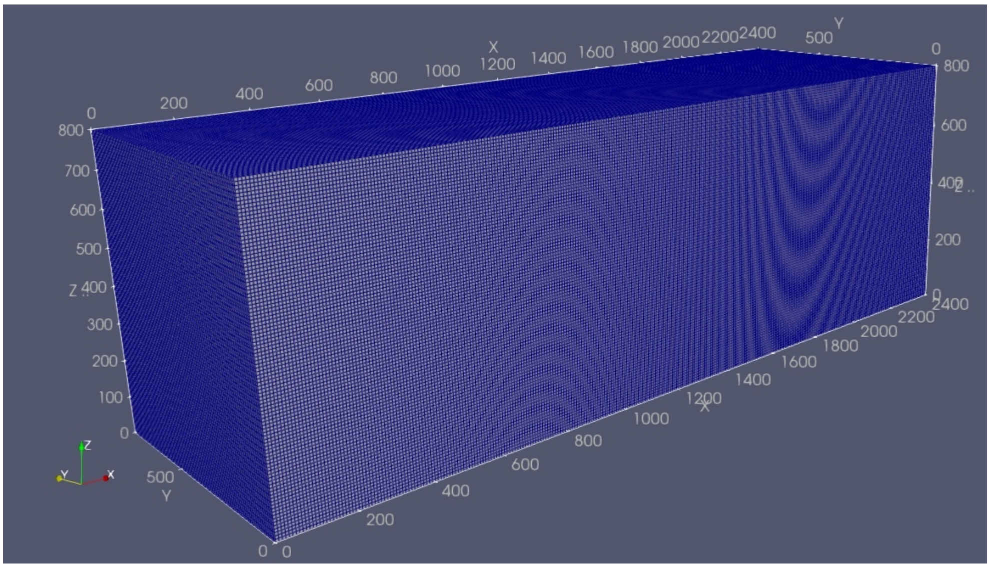

Figure 4.4: Grid domain for the large sized grid: the grid used throughout this study. Domain has length x width x height of 2400 x 800 x 800 [m] consisting of a total of 3 million grid cells.

	d_x	d_y	d_z	N_{cells}
s-grid	800	800	800	1.000.000
m-grid	2000	800	800	2.500.000
l-grid	2400	800	800	3.000.000

Table 4.1: Grid domain size specifications.

The three different sized grids show no difference in the ABL development throughout the domain so no backflow problems or any other mesh issues are recorded. The largest grid is used throughout the simulations discussed from this point onward.

Boundary conditions

Prior to solving the flow equations, boundary conditions need to be assigned to the envelopes of the grid. Table 4.2 summarises the boundary conditions assigned to the inlet and outlet of the system. As discussed in Section 4.1.2

the inlet of the system is set using the atmBoundaryClass. Inlet boundary conditions for U, k and ϵ are set by equations 4.5-4.7. The outlet boundary condition inletOutlet sets a fixed value for possible reversed flows (her 0) and assigns a zeroGradient condition to the outflow. A zeroGradient boundary condition extrapolates the internal field value to the boundary, thus not affecting the flow near the outlet in any way. The gradient perpendicular to the plane is set to zero. Nut is the turbulent viscosity and is numerically solved and calculated from the other parameters. For that reason its boundary conditions is set to Calculated.

	Inlet	Outlet
U	atmBoundaryLayerInletVelocity	inletOutlet
p	zeroGradient	uniformFixedValue
k	atmBoundaryLayerInletK	inletOutlet
ϵ	atmBoundaryLayerInletEpsilon	inletOutlet
nut	Calculated	Calculated

Table 4.2: Boundary conditions for the Inlet and Outlet of the system.

	Ground	Sides	Top
U	uniformFixedValue	Cyclic	zeroGradient
p	zeroGradient	Cyclic	zeroGradient
k	kqRWallFunction	Cyclic	zeroGradient
ϵ	epsilonWallFunction	Cyclic	zeroGradient
nut	nutkAtmRoughWallFunction	Cyclic	zeroGradient

Table 4.3: Boundary conditions for the Ground, Sides and Top of the system.

Table 4.3 summarises the boundary conditions for the Ground, Sides and Top planes of the grid domain. Cyclic boundary conditions are assigned for all parameters to all sides of the model: flow crossing one side is ensured to enter the other side. This prevents mass flow lost through the sides of the domain (even though the flow through the sides of the domain is small). If a boundary condition different than the cyclic boundary condition is used, mass flow through the sides of the domain might be lost. This would cause the pressure to drop throughout the domain. Another reason for using the cyclic boundary condition is that it presents the most realistic wind farm simulations where turbines experience wind coming from different directions. To the top of the domain a zeroGradient boundary condition is assigned so that it does not affect the course of the flow over the domain and block any reverse flows. The velocity at the ground of the domain is set to 0 using the uniformFixedValue boundary condition while the pressure is assigned a zeroGradient boundary condition. The kqRWallFunction boundary condition is a zeroGradient like boundary condition, specifically created in OpenFOAM for the turbulent kinetic energy. The nutkAtmRoughWallFunction assigns the the surface roughness factor z_0 of 0.0002 (as discussed in Section 4.1.2).

Solver

OpenFOAM offers a range of solvers with each their own conditions to consider when being used. As described in Chapter 3, for the simulations in this work we use the stationary RANS turbulence model, while focusing on steady-state incompressible flows. SimpleFOAM is the most widely applied solver under these conditions. Stergiannis et al. [2016] use simpleFOAM to study two turbine rotors with exact geometries for the blades and hub, and compare their findings with the simplified actuator disc model. Richmond et al. [2019] uses the simpleFOAM solver for comparing the measurement results of a real wind farm with a simulated wind farm using the actuator line method. The actuator line method will be further explained in chapter 5, where this method is used to simulate the kites.

SimpleFOAM is a steady-state solver for incompressible, turbulent flow of a single phase under isothermal conditions. SimpleFOAM uses the SIMPLE loop, the Semi-Implicit Method for Pressure Linked Equations loop, to numerically solve the combined continuity and momentum equations presented in Chapter 3. An iterative approach starts by first solving the momentum equation to obtain an initial velocity field. This velocity field is used in both the momentum and continuity equations to obtain the pressure field. Next, this pressure field corrects for the velocity field and the combined velocity and pressure field equations can then be used to solve for the turbulence equations. This iterative (of first setting a pressure and velocity field and next correct for the velocity) is repeated until convergence is reached.

The ABL, the wind farm and kite simulations all use steady state time schemes, with Gauss linear gradient schemes and bounded Gauss upwind divergence schemes for the velocity and turbulence equations. A run-time smooth solver is in operation for all variables and a simulation duration of 5000 iterations caps the simulation, if convergence is not reached. Time and time-steps discussed in the results sections discuss the iterations til convergence of the system, (thus) not the time the wind flows through the system. Timesteps of 1 second have been applied with write interval after every 50 time-steps.

4.1.4 Atmospheric boundary layer simulation results

The goal of the empty domain simulations is to check whether the log-law velocity profile reaches steady-state throughout the entire domain. For every height a constant velocity throughout the domain is desired. The log-law profiles of the velocity, turbulent kinetic energy and dissipation of turbulent kinetic energy are compared to literature. With similar results as literature findings, the wind farm and kite simulations can be performed in the same grid using the same boundary conditions. To reach this goal, the large empty domain presented in Section 4.1.3 was simulated using the simpleFOAM solver. Results for the velocity, pressure, turbulent kinetic energy, the rate of dissipation and turbulent kinetic energy are discussed with a focus on the log-law profiles of the velocity.

Figure 4.5 shows the velocity profile through the domain directly after the first timestep (t=1sec). An unexpected velocity increase is seen (note the lighter red and darker red in the horizontal plane) in the downwind direction of the system. This velocity increase is observed to disappear at later timesteps, see Figure 4.6. Zooming in on the velocity profiles at 3 different locations and for different time steps results in similar findings.

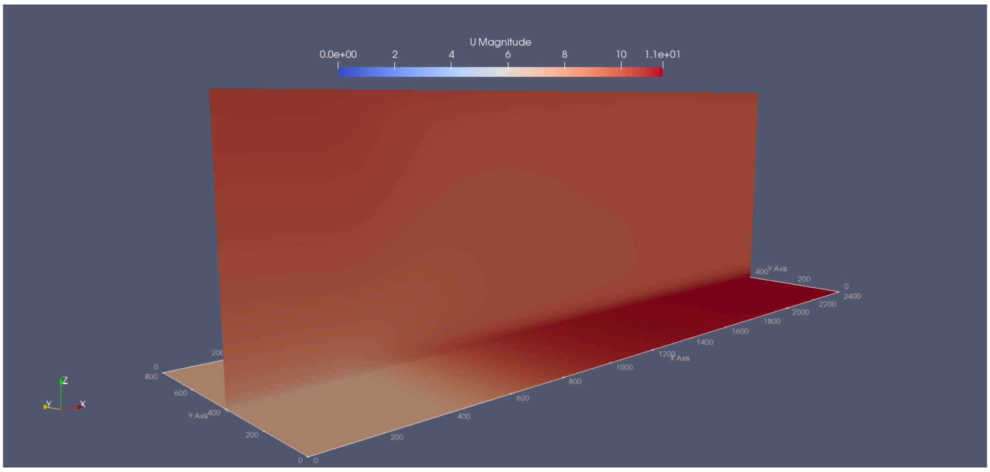

Figure 4.5: Velocity profile through domain during the first iteration. Two cross sections are plotted at a height of 10 meters, and at a width of 400 meters.

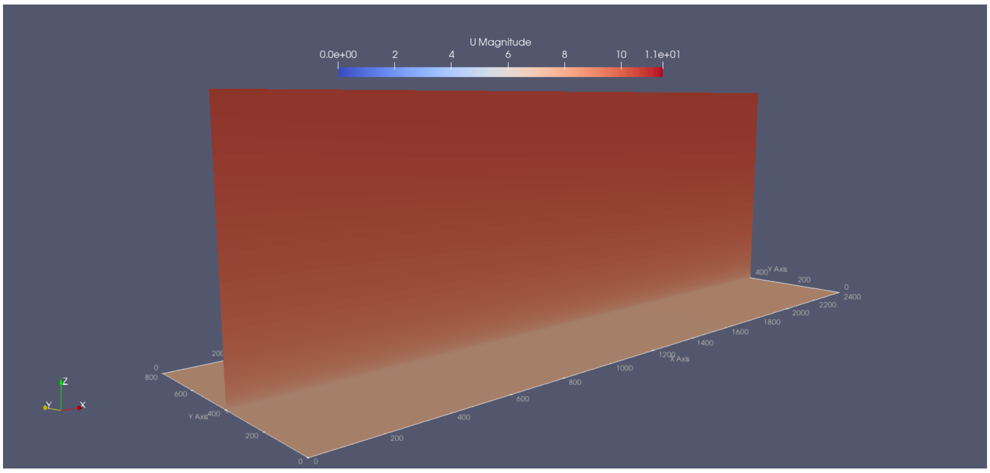

Figure 4.6: Velocity profile through domain during the final time-step. Two cross sections are plotted at a height of 10 meters, and at a width of 400 meters.

Figure 4.7 and Figure 4.8 show velocity profiles at the first and final timestep. The plots are taken at x = 10m (inlet), 1200m (centre) and 2350m (outlet). A transient phenomenon in the wind velocity in the initial simulations can be observed. This transient behaviour can be explained by the different boundary conditions that are imposed to the model. The imposed log-law velocity profile to the inlet of the model will cause a pressure wave going through the model and it will take a number of timesteps before the imposed log-law profile is adopted by the whole grid. In our model, it takes about 10 timesteps to reach a semi steady-state log law velocity profile throughout the whole model. All wind farm and kite simulation results discussed in this report have been performed in semi steady state conditions, with an ABL following the log-law profile throughout the whole model. For wind farm and kite simulations, results from later iterations must thus be used to compare simulation results with literature values. Additional velocity magnitude profiles versus height at different iteration numbers are presented in Appendix A to illustrate the effects of iteration number on convergence.

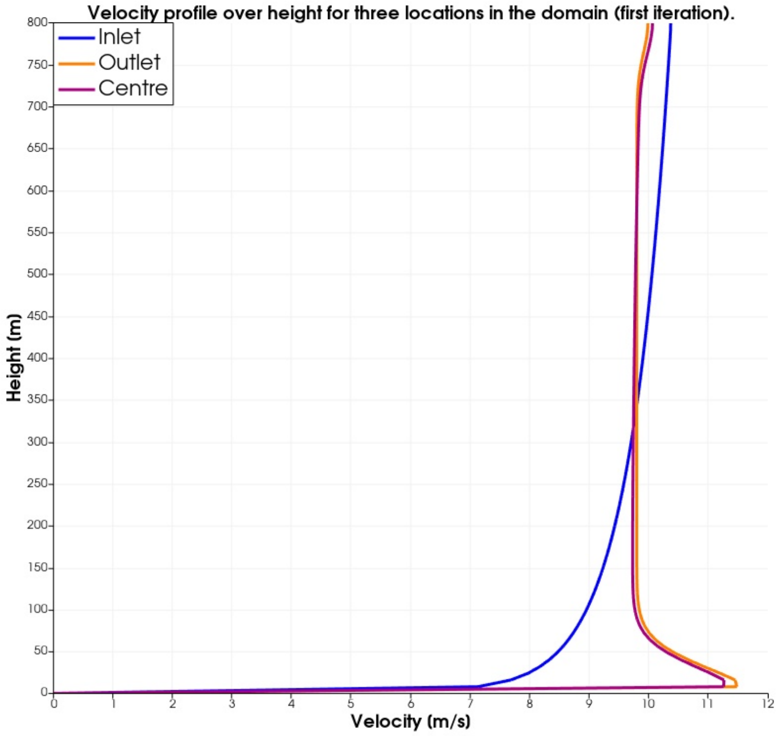

Figure 4.7: Velocity profile over height at timestep 0 at x=10, 1200 and 2350 meters.

The wind shear log law profile given by the atmBoundaryLayer class thus resembles the vertical theoretical wind shear log law closely after convergence. Another result that needs to be checked are the constant wind velocity at similar height, turbulent kinetic energy and dissipation of turbulent kinetic energy throughout the empty domain. Figure 4.8 already showed that the wind speed velocity follows the theoretical log-law relation well throughout the domain. As the log-law profiles at the inlet, centre and outlet overlap closely, constant velocity throughout the domain can be concluded.

Figure 4.9 and Figure 4.10 present vertical profiles for the turbulent kinetic energy and dissipation of turbulent kinetic energy at the inlet and outlet of the domain. Like the vertical wind speed profiles, the vertical pro-

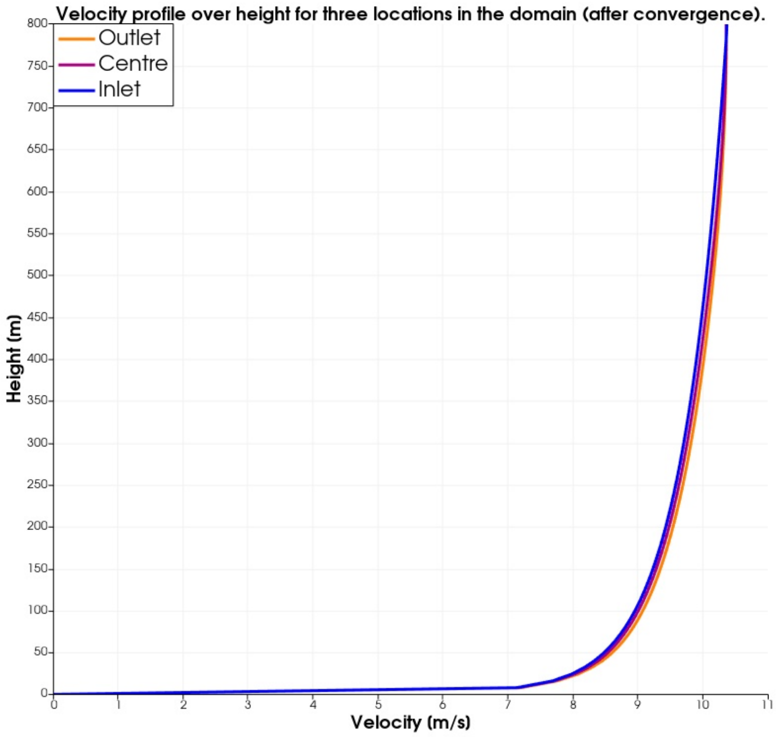

Figure 4.8: Velocity profile over height at the final timestep at x=10, 1200 and 2350 meters.

files of dissipation of turbulent kinetic energy at the inlet and outlet of the domain appear similar and can thus be regarded constant throughout the domain. Figure 4.9, however, shows a significant difference between the turbulent kinetic energy profiles at the inlet and outlet of the domain, even though convergence has taken place. However, because this is a whole different study, and because the different k profiles don't seem to effect the velocity and dissipation of turbulent kinetic energy a lot, this problem is left for future research.

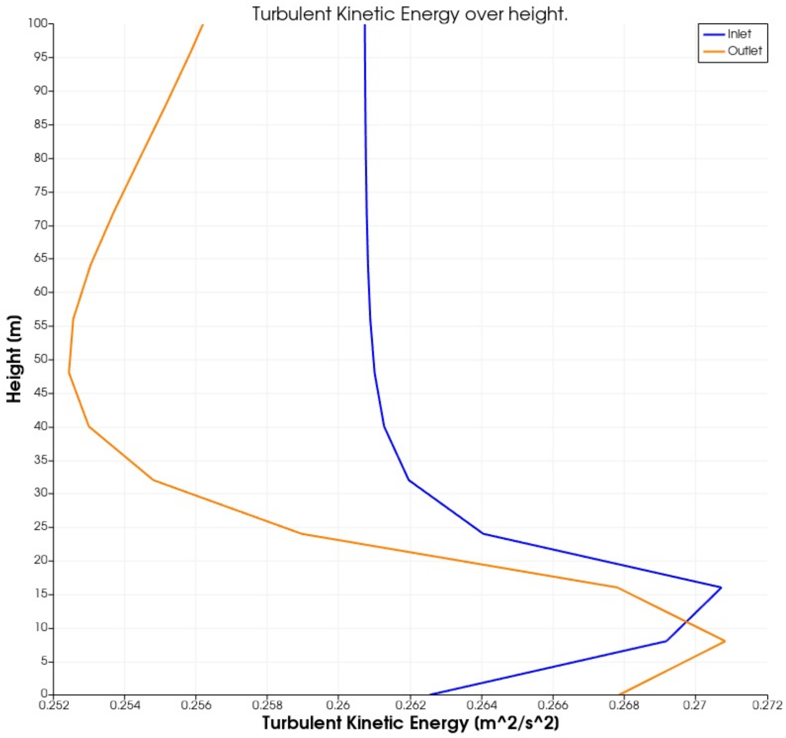

Figure 4.9: Turbulent kinetic energy over height at the inlet and outlet of the domain.

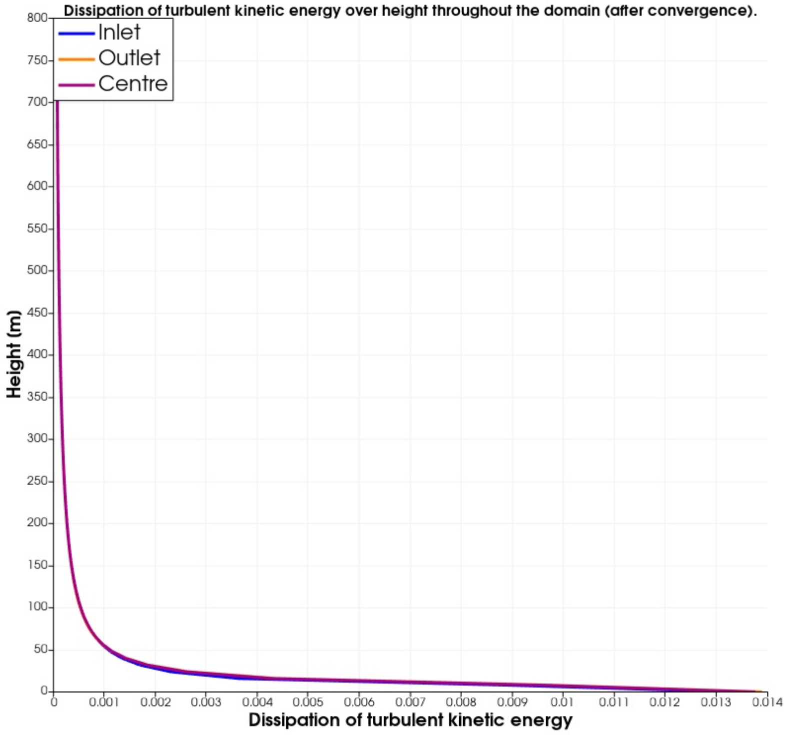

Figure 4.10: Dissipation of turbulent kinetic energy over height at the inlet and outlet of the domain.

4.2 WIND FARM SIMULATIONS

Simulations of fully resolved wind turbine blades are very costly from a computational point of view. For studies involving multiple wind turbines, simplified models for rotor and blades are required. Two of the better known simplified representations for wind turbines and their blades are the AL (actuator line) model and the AD (actuator disc) model, with the AD model being further simplified than the AL method. Martínez et al. [2012] and Wu [2012] compare the performance of the AD and AL method for wind turbine modelling in predicting produced power and velocity lost (in the wake) in wind farms. Both conclude that the two models give results that are in good agreement with experimental values for applying forcing on the wind. Martínez et al. [2012] find the AD and AL model to be both within 8% of the theoretical values (predicted by blade element momentum theory) for power production, where the AL model to even be in a 4% range of theoretical values. The AL model also captures flow structures better than the AD model. AL is a more complex representation of turbine blades, therefore represents wind and forcing more accurately, but is computationally costly. Therefore, we have chosen to model the 4 turbines with AD and apply AL on the kite. One argument for the selection of the AD model for turbine blades is that an accurate representation of the kite is of more importance in this study than the wind turbines. The effects of applying kites in a wind farm is the main focus of this study, and only the averaged velocity increases on the turbines are studied so a less computationally costly model can be used to represent the actuator discs.

4.2.1 Actuator Disc Theory

The AD method uses the concept of an ideal wind turbine to describe the main effects a wind turbine places on the wind flow. The actuator disc assumes an incompressible, inviscid, and isentropic fluid. It replaces the rotor of a traditional wind turbine with an infinitesimally thin actuator disk to study the effects of the disk on the flow as shown in Figure 4.11. Basic momentum theory of a free flow addresses the mass flow rate, momentum flow rate and kinetic energy flow rate given in formulas 4.8-4.10 with the mass flow rate ($\dot{m}$) and the actuator disc area (A_{wt}).

$$\dot{m} = \rho U A_{wt} \tag{4.8}$$

$$\dot{m}U = \rho U^2 A_{wt} \tag{4.9}$$

$$1/2\dot{m}U^2 = 1/2\rho U^3 A_{wt} \tag{4.10}$$

When the actuator disc is placed in this free flow, it exerts an uniform thrust force on the wind flow and power is extracted by converting part of the kinetic energy (in e.g. electric energy) from the free flow. With the same mass flow rate entering the streamtube as leaving it, and wind velocity dropping because of the force, the streamtube expands.

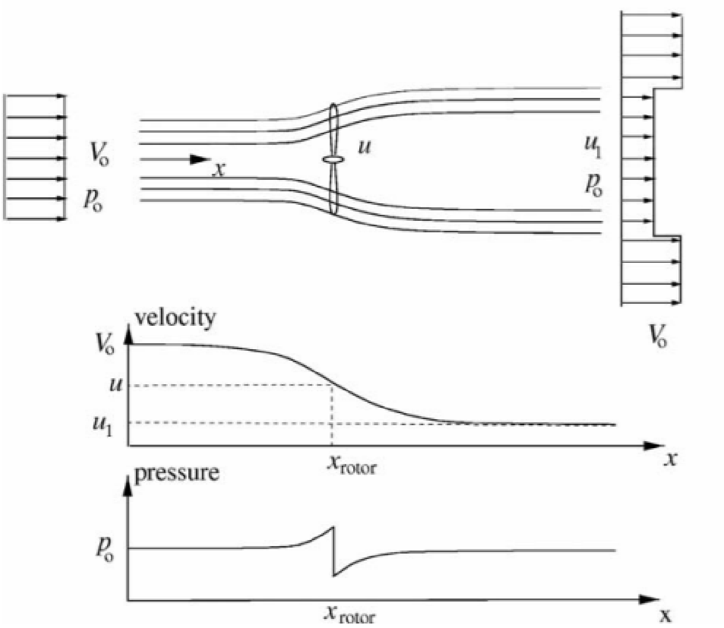

Figure 4.11: Effects of wind passing through the actuator disc: streamtube expansion, velocity decrease and pressure jump (Hansen [2013]).

When the actuator disc is placed in the flow field, a high pressure region is created at the front of the object while a low pressure region is formed at the back of the object. For an infinitesimally small disc, a pressure drop (Δp) is formed that relates to the thrust force (T) and A_{wt} using equation 4.11. The loss of velocity results directly from T while the loss of energy equals the wind turbine power (P_{wt}) extracted from the system, with U_e being the outlet velocity (U_e). This is presented using equations 4.12 and 4.13 respectively, where equation 4.14 relates the thrust force and power extracted using the rotor velocity (U_r). Further simplifying yields a relation between the velocities, given in equation 4.15.

$$\Delta p = T/A_{wt} \tag{4.11}$$
$$T = \dot{m}\,(U - U_e) \tag{4.12}$$
$$P_{wt} = 1/2\dot{m}\left(U^2 - U_e^2\right) \tag{4.13}$$
$$P_{wt} = TU_r \tag{4.14}$$
$$U_r = 1/2\,(U + U_e) \tag{4.15}$$

A non-dimensional induction factor (a) can be defined, that is a measure of the velocity loss of the wind flow by the actuator disc:

$$a = \frac{U - U_r}{U} = \frac{\Delta U}{U} \tag{4.16}$$

Rewriting equation 4.16 yields representations of the inlet and rotor velocity depending on induction factor a. Now equations 4.12, 4.14 and 4.15 can be rewritten to describe the dependency on this induction factor, given in equations 4.17-4.19:

$$\dot{m} = \rho U_r A_{wt} = \rho U A_{wt}(1-a) \tag{4.17}$$

$$T = \dot{m}\left(U - U_e\right) = 1/2\rho U^2 A_{wt} 4a(1-a) \tag{4.18}$$

$$P_{wt} = \dot{m}\left(U - U_e\right) U_r = 1/2\rho U^3 A_{wt} 4a(1-a)^2 \tag{4.19}$$

A wind turbine's thrust coefficient (c_T) and power coefficient (c_P) can be made non-dimensional using equations 4.18 and 4.19 and yield equation 4.20 and 4.21:

$$c_T = \frac{T}{1/2\rho U^2 A} = 4a(1-a) \tag{4.20}$$

$$c_P = \frac{P}{1/2\rho U^3 A} = 4a(1-a)^2 \tag{4.21}$$

In Figure 4.12, the thrust and power coefficient are plotted as a function of induction factor a. As can be seen from these, both coefficients exhibit maximums. For the power coefficient a maximum of 16/27 at a=1/3 can be calculated. This is an interesting result, the so-called Betz limit (after its discoverer) and represents the theoretical limit of power extracted by a single wind turbine. Taking the derivative of equation 4.21 to a yields another method of finding the maximal power coefficient.

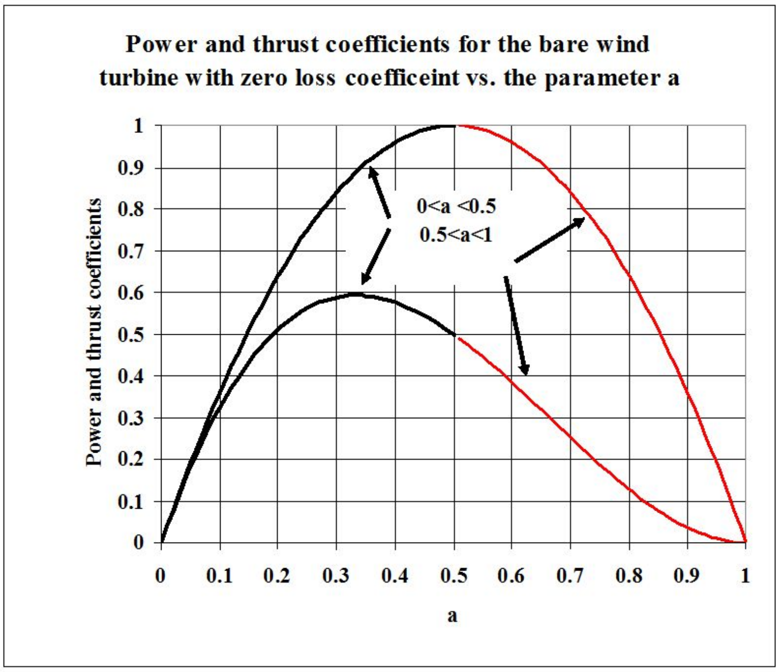

Figure 4.12: Power and thrust coefficient curve plotted versus induction factor a (Ivanova et al. [2016])

4.2.2 Wind turbines in OpenFOAM

OpenFOAM contains the actuationDiskSource which applies sources, in this case forces, on the velocity. Forces are applied on the volume cells instead of the faces of the actuator disc, which disembarks from the principle of theoretical actuator discs being infinitely small. However, this does not result in any major, nor minor, consequences (see Verweij [2010]). The actuationDiskSource uses the fvOptions to add force sources to the RANS equations, and places the forces in the domain (on the disc area) using cellSetOption [The OpenFOAM Foundation [2017]].

In OpenFOAM two different techniques for force computations can be applied: Froude's ideal one-dimensional actuator disc method and the variable scaling actuator disc method[1]. For wind farm simulations, Froude's method is more often applied (Hoem and Kristoffersen [2019], Richmond et al. [2019]). Froude's ideal one-dimensional actuator disc method was presented by R.E. Froude in 1889. Burton et al. [2011] applied Froude's ideal one-dimensional actuator disc theory to arrive at a set of equtions for CFD simulations:

$$T = 2\rho_{ref} A_{wt} \left|\mathbf{u}_m \cdot \mathbf{n}\right|^2 a(1-a) \tag{4.22}$$

$$a = 1 - \frac{C_p}{C_T} \tag{4.23}$$

with the monitored incoming fluid density (ρ_{ref}), spatially averaged incoming velocity on monitored region (u_m) and surface-normal vector of the actuator disc pointing upstream (n).

4.2.3 Wind farm case setup

In Section 4.1.3 the creation of the mesh was described, setting the boundary conditions in the domain and listing the most important specifications of the solver. For the wind farm simulations most of these aspects remain similar. However, the wind turbines will be placed in the mesh and refinement near the wind turbines will be applied to reach the required grid cell resolution of $\Delta_{max} \leq 0.05\text{D}$. At the end of this section an overview of three different wind farm simulations will be presented, with results summarised in Section 4.2.4.

Basic domain specs

The process of simulating wind farms is similar to the simulations of the ABL. Initially coarser grid were used to test and trouble shoot. The final, large sized grid, is selected to contain the 4 actuator discs lined in downwind direction. Ploumakis [2015] found that for a wind farm with only two turbines in a row, wake recovery was minimal and turbulence levels were continuously increasing showing an underdeveloped wake flow. Ploumakis concluded that at least 4 actuator discs are required in future simulations. Ploumakis [2015] for that reason stated the need for 4 actuator discs minimum to provide a base case for additional simulations. In this work, simu-

---

[1] See Van der Laan et al. [2014] for a detailed explanation of the variable scaling actuator disc method. Section 2.2.

lations with 4 actuator discs in a row are considered.

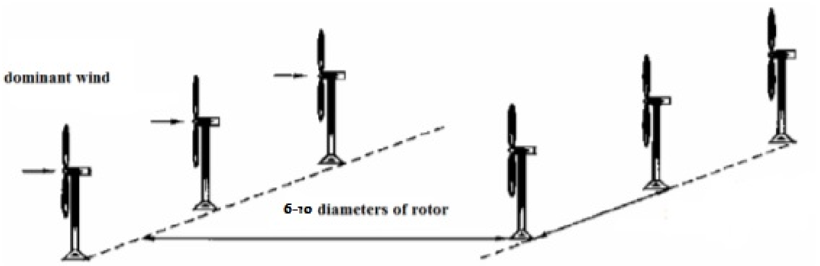

Figure 4.13: Optimal spacing for wind turbines in a wind farm (adaptation of Panaitescu et al. [2019] using the work of Howland et al. [2019])

The actuator discs have a diameter D_{wt} of 80 [m] and are located at a height of 80 [m] (thus having a sweep height between 40 and 120 [m]). Howland et al. [2019] states that the optimal streamwise spacing between wind turbines to minimize aerodynamic losses is 10-15D_{wt}. However, with ever increasing sized turbines, wind farms require kms of power cables and large areas of land or oceans, increasing costs dramatically. For that reason, operational wind turbine spacing of 6-10 D_{wt} is generally used, visualised by Panaitescu et al. [2019] in the picture above[2]. With a diameter of 80 [m], the distance between the actuator discs should be between 480-800 [m]. To optimise computational costs a spacing of 500 [m] was selected. Between the fourth actuator disc and the outlet of the domain another spacing of 500 [m] was set to establish the wake recovery behind the fourth rotor. Between the inlet and the first actuator disc 400 [m] of distance is set to establish the velocity log-law profile coming from the inlet. In total the domain length is 2400 [m] (400 [m] + 4x500 [m]). The grid with the locations of the actuator discs is presented in Figure 4.14.

Meshing

The domain mesh parameters have unchanged, so the code provided in Section 4.1.3 have remained unchanged. A width and height of 800 [m] is selected and a total distance of 2400 [m] sets the length of the domain, as explained above. With the desired grid cell resolution of $\Delta_{max} \leq 0.05$D near the body of interest, a grid cell resolution of 4x4x4 [m] is near the actuator discs. As discussed earlier, with the application of grid refinement a fine grid near the actuators and a coarse grid away from the turbines can be realised. OpenFOAM provides different methods for grid resolution of which the one used in this work is described next. (Note that different methods of refinement can be found in Weller et al. [1998] or in the User Guid of openfoam.)

---

[2] Note that Panaitescu et al. [2019] proposes 5-9 diameters of rotor distance instead of the 6-10 given by Howland et al. [2019]. Findings of Howland et al. are used in this work as more literature supports the statements presented by Howland et al. [2019].

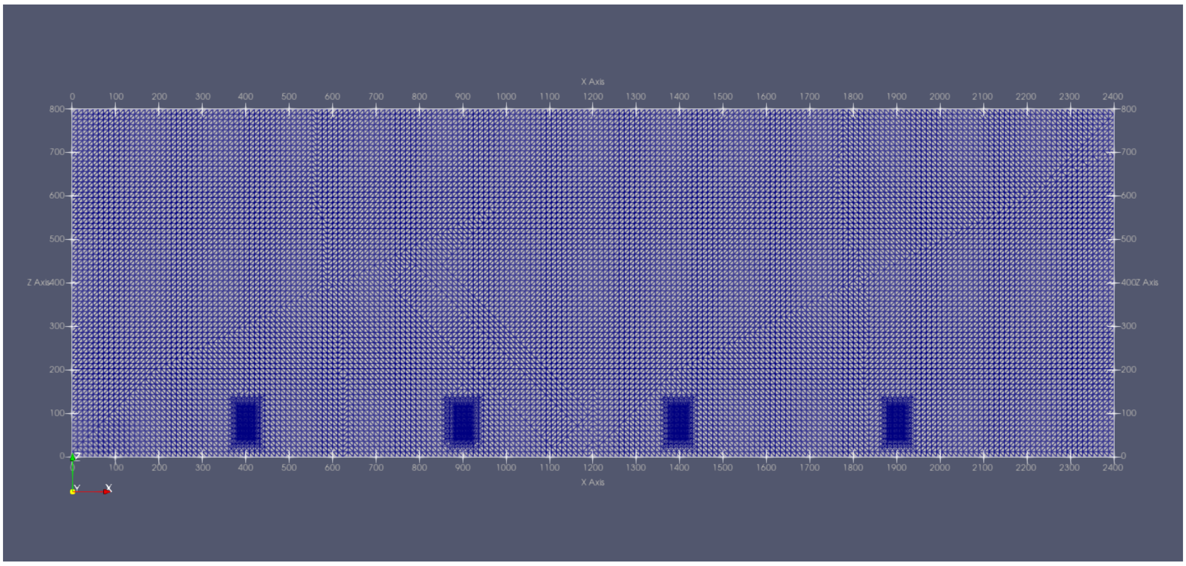

Figure 4.14: Slice through grid domain presenting the locations of the actuator discs at x = 400, 900, 1400 and 1900 [m] at a hub height of 80 [m]. Note that the refinement regions present near the actuator discs are only used for visualisation purposes. The selection of the refinement region is presented in the next section.

SnappyHexMesh is one of OpenFOAM's main mesh refinement tools. Coarsening the resolution in a large part of the domain while refining and increasing the amount of grid cells near the actuator discs, cuts total computational costs and increases resolution at specific locations. These so-called refinement regions are specified in SnappyHexMesh using the searchableBox type which sets a refinement box over the region of interest. In this study the following code is used:

```
windTurbine
{
type searchableBox;
min (0 350 0);
max (2400 450 180);
}

windTurbine
{
mode inside;
levels ((3 3));
}
```

This code yields a refinement box region throughout the domain specified in Table 4.4. As the effects of the wind turbines and kites on the wind flow throughout the whole domain are of interest, the refinement box overlaps with the whole domain in the x-direction. The turbines have a radius of 40 [m] and their centers are located in the centre of the box (400 [m]). This causes the sweep area in the y-direction to range between 360 [m] and 440

[m]. Providing some room for the refinement to take place, the refinement box is located between y = 350 and 450 [m]. In z-direction, the refinement box is set to ranges between ground level (z = 0 [m]) and z=180 [m]. The 180 [m] height is chosen as this is the maximum height the kites will be located at, further explained in Chapter 5. The second snippet of code sets the refinement level inside the box region with a refinement factor of 2. Note that refinement levels are specified as a power of two. So a level 1 refinement level divides a cell into two cells, level 2 divides a cell into four cells, and level 3 divides a cell into 16 cells. With this, the coarser grid cell resolution in the grid can be set to 16x16x16 [m], cutting computation costs drastically, while near the actuator discs the resolution is refined to the desired resolution of 4x4x4 [m]. This changes the main blockMesh file by setting the x, y and z- direction in 150, 50 and 50 grid cells respectively so that a coarse grid resolution of 16x16x16 [m] is reached. Figure 4.15 shows a cross-section of the refinement region in the YZ plane. Figure 4.16 shows part of the the refinement region in the XZ plane.

	minimum value	maximum value
x-direction	0 [m]	2400 [m]
y-direction	350 [m]	450 [m]
z-direction	0 [m]	180 [m]

Table 4.4: Refinement box specifications.

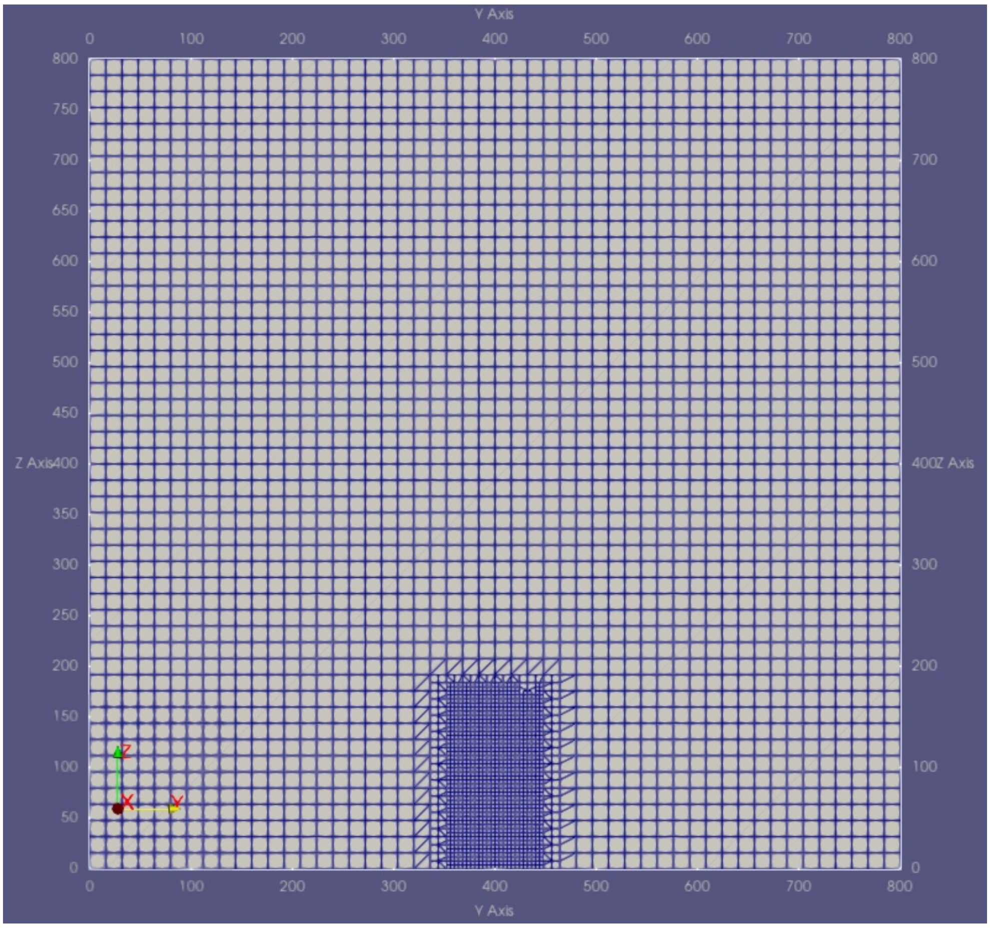

Figure 4.15: Box refinement region in the YZ plane.

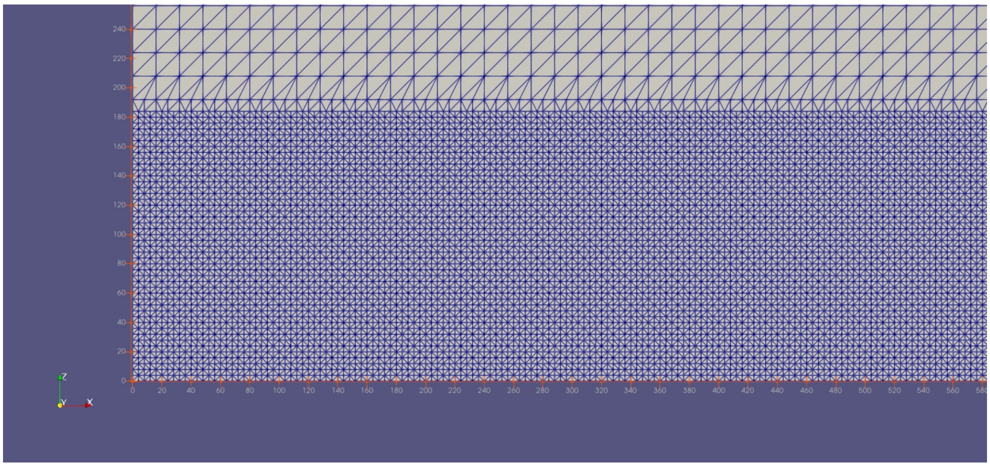

Figure 4.16: Part of the box refinement region in the XZ plane.

Boundary conditions and sources

To generate the same realistic atmospheric boundary layer as described in Section 4.1, exactly the same boundary conditions are imposed at the same sides of the domain. These are presented in Table 4.2 and Table 4.3.

With the refinement region around the actuator discs set, the sources, in this case thrust forces, need to be set at the locations of the actuator discs. As explained in Section 4.2.2 fVOptions introduces the source terms to the RANS equations. TopoSetDict sets the actuator discs to the correct grid cells. The corresponding code for actuator disc 1 is:

```
FvOptions:
disk1
{
type actuationDiskSource;

fields (U);

selectionMode cellSet;
cellSet actuationDisk1;
diskDir (1 0 0); // Orientation of the disk
Cp 0.592;
Ct 0.888;
diskArea 5026.548246;
upstreamPoint (400 400 80);
}
```

Actuator disc 1 is introduced as an actuationDiskSource in the wind direction (1 0 0) affecting velocity field V by setting a force based on the incoming wind speed, and dividing this forcing over the entire disc area. The thrust force is calculated using equation 4.22, specified in Section 4.2.2. The diskArea is simply calculated by A = $\pi * R^2$ and the power and thrust coefficient are set to 0.592 (16/27) and 0.888 (8/9) (based on the optimal induction factor and equations 4.20 and 4.21) for all four actuator discs. The values for the power and thrust coefficients are theoretical maximum values and may not be practical. However, the theoretical maximum values will provide the largest wake formation (by inducing the largest thrust force) so the impacts of kites are expected to be largest. For this reason no further refined or even varying power and thrust coefficients have been used in the Base Case simulation.

A limitation of this actuator disc model is its strong dependence on the up stream point. As presented in equation 4.22, the thrust force strongly depends on the incoming velocity spatial-averaged on the monitored region. This velocity is determined by the upstream point given in the code above. The user sets the upstream point and the velocity at this upstream point is used to calculate the total thrust force which is then spread over the actuator disc evenly. The upstream point should not be located too close to the turbine rotor as the wind velocity drops in front of the rotor as a result of the pressure build-up. However, the upstream point should also not be located too far away, especially in between wind turbines where wake recovery already takes place between the turbines. For this reason, the first wind turbine can have a upstream point far in front of the rotor, while the three other wind turbines should have it relatively close located to the rotor, so the effects of wake recovery are taken into account. In this study, the upstream points for the actuator discs have been set at the same location for all simulations and are summarised in Table 4.5. The first wind turbine has its upstream point 300 [m] in front of the rotor, the other wind turbines 100 [m] in front of the rotor. The exact location for actuator discs two-four is determined studying the location where the velocity starts to drop again. This is generally about 100 [m] in front of the rotor.

	x-value	y-value	z-value
Actuator Disc 1	100 [m]	400 [m]	80 [m]
Actuator Disc 2	800 [m]	400 [m]	80 [m]
Actuator Disc 3	1300 [m]	400 [m]	80 [m]
Actuator Disc 4	1800 [m]	400 [m]	80 [m]

Table 4.5: Upstream point locations for all four actuator discs.

In the topoSetDict file, the actuationDiskSource is set on the grid volume cells of a small cylindrical volume. An infinitesimal small actuator disc would require the grid cells to be infinitesimal small as well, requiring an extremely large amount of grid cells. Using this infinitesimal small actuator disc with a finite grid cell size used in this work, the topoSetDict does not recognise any cells to which it can apply the thrust force, thus not being able to introduce the actuator discs into the domain. To solve this problem, the actuator disc is represented as a thin cylindrical volume, of which the topoSetDict is able to recognise cells. The thrust force is spread over this cylindrical volume. This is a widely accepted method for solving the issue that OpenFOAM simulations (and CFD simulations in general) can not introduce the ideal infinitesimal actuator disc into the domain.

Wind farm simulation cases

Three main wind farm simulation cases are set up, simulated and explored in Section 4.2.4. The distinctions between these three cases are as follows:

1. Case 1 uses the power coefficient and thrust coefficient for the optimal induction factor for **all 4 actuator discs**. This case provides the base case for the kite simulations in Chapter 5.

2. Case 2 uses a different induction factor for the first wind turbine to study the effects on efficiency with the first turbine partially loaded. This case presents an additional method of validation with literature through studying one method one method of increasing wind farm efficiency.

3. Case 3 uses a much higher wind velocity inflow of 10 [m/s] at a reference height of 18.5 [m] to present a reference simulation without kites used in the kite simulations chapter.

Case 1 and 2 are used to explore and evaluate the findings of Barth et al. [2007]. Case 3 sets the base for a sensitivity study for the kite simulations as the forcing of the kites on the wind flow strongly depends on the velocity of the wind. Simulations of a wind farm and kites with higher wind speed velocity may result in higher downwash values, thus higher wind farm efficiency increases.

4.2.4 Wind farm results

Case 1: Optimal induction factor

Case 1 sets the power coefficient (C_P) of all 4 actuator discs to 0.592 (16/27) and the thrust coefficient (C_T) to 0.888 (8/9), which results from equations 4.20 and 4.21 when inserting the optimal induction factor ($a = 1/3$). With a resolution of 16x16x16 [m] and a refinement region covering the actuator discs, the simulation requires only 862 iterations before converging (with a clock time of a little over 1 hour). Figures Figure 4.17 and Figure 4.18 show the pressure and velocity profiles through cross sections of the domain (at a late timestep so that the ABL velocity follows the log-law as explained in Section 4.1.4).

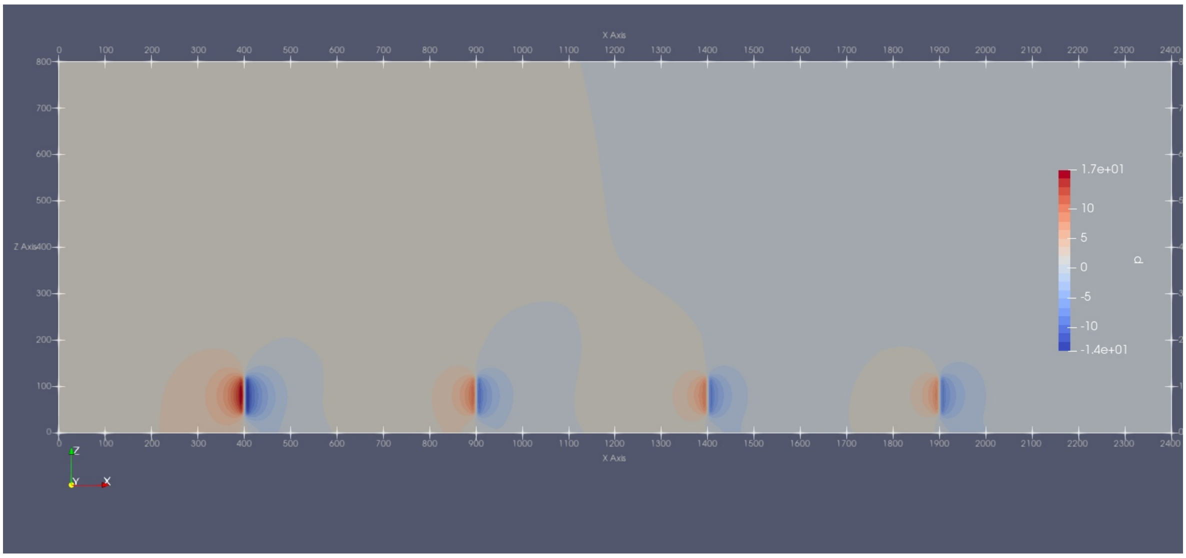

Figure 4.17: Pressure drops over the four actuator discs for the optimal induction factor

Because the wind flow has not been altered in front of the first rotor, the highest velocity (in front of any of the four rotors) can be found in the front of the first rotor. It is expected that for this reason the largest pressure field will be found in front of the first rotor aswell. Figure 4.17 shows this is the case, and the pressure drops to a much lower value behind the actuator disc, where a lower pressure field is found. In front of the rotors, up to 100 [m], the pressure field affects the wind flow already which can be seen in Figure 4.18. Regions of constant velocity (specified with a same color) move up or down in front of the rotors, lowering the velocity at hub height (80 [m]). It is exactly because of this reason, the upstreampoint is located 100 [m] in front of the rotor instead of being located exactly in front of the rotor. The velocity graph shows some results that are expected around the turbines. The wind flow drops from a large value in front of the turbine to a much

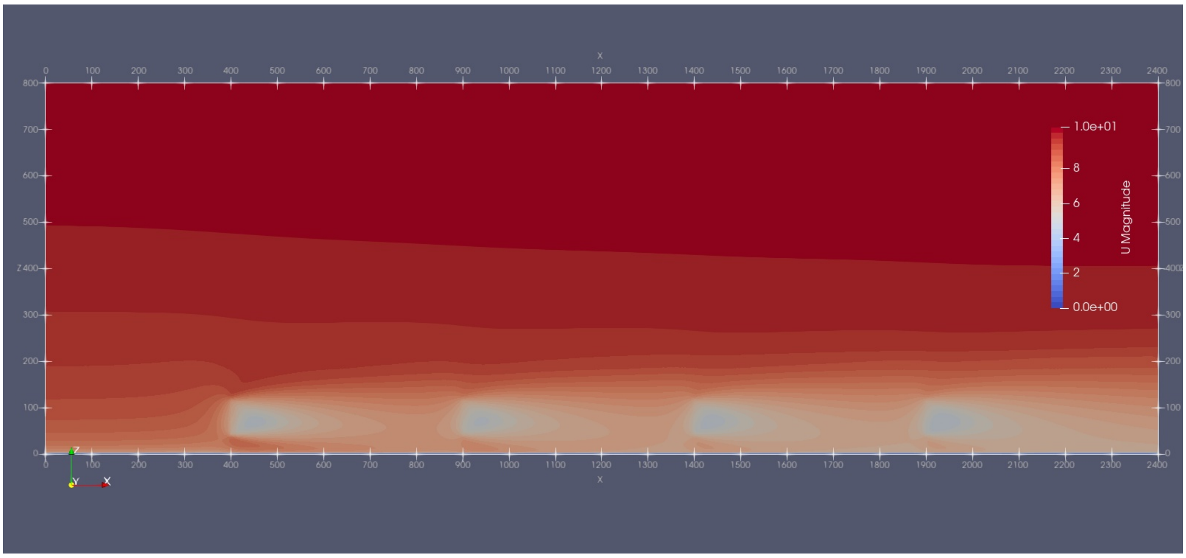

Figure 4.18: Velocity drops over the four actuator discs for the optimal induction factor

lower value in its wake, while below and above the actuator disc the wind speed increases, because the wind is pushed below or above the turbine. At hub height, the effects of the wake can clearly be noted up to about 100-150 [m] behind the rotor after which the velocity slowly re-energizes (and thus increases) with wind coming from the unaffected boundary layer, or wind that is pushed underneath or over the rotor and mixes with the wake. The wake region expands throughout the domain, visible by the velocity contour lines throughout the domain.

An interesting observation is the pressure difference throughout the entire domain. Clearly, a slightly higher pressure region can be found in the first half of the domain, while a lower pressure region is found in the second half of the domain. This is actually not caused by any wake or turbine behavior. It has to do with the boundary conditions for the pressure at the inlet and outlet and the necessity of a pressure field throughout the domain for the wind to flow. The zeroGradient boundary condition at the inlet and uniformFixedValue (of 0) at the outlet cause a slight variation in pressure throughout the domain. Setting both the inlet and outlet to the same boundary condition would fail to result in any specified pressure value throughout the domain, causing the pressure not to be recognised at all. The effect of this pressure difference throughout the domain has been studied while simulating the ABL. It was concluded in Section 4.1.4 that this slight variation in pressure does not impact any other results.

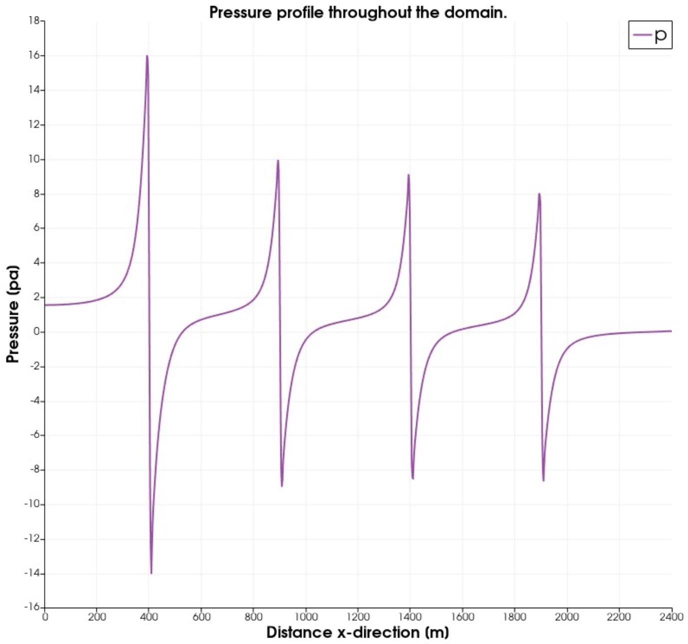

Figure 4.19: Line plot at hub height of the pressure throughout the domain.

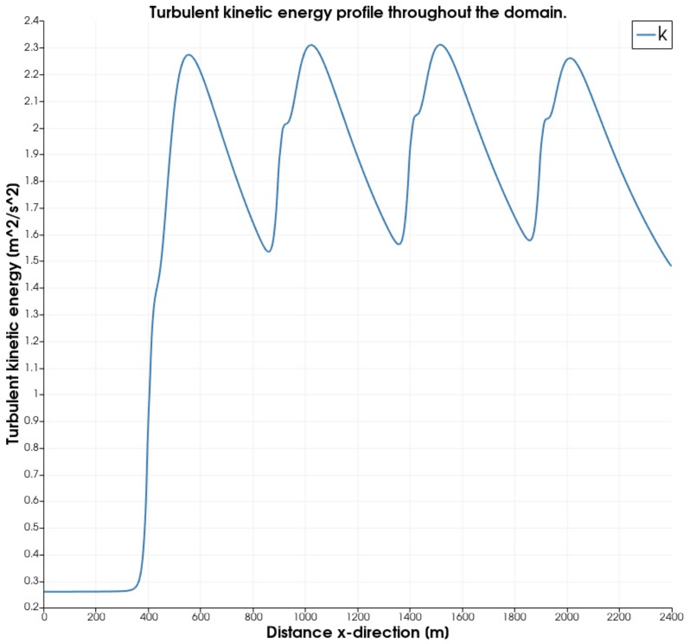

Figure 4.20: Line plot at hub height of the turbulent kinetic energy throughout the domain.

Line plots at hub height throughout the entire domain for the pressure, turbulent kinetic energy and velocity can be found in Figure 4.19, Figure 4.20 and Figure 4.21 respectively. The pressure graph shows the expected behavior that the first actuator disc experiences the highest pressure drop, with downwind turbines experiencing a decreasing pressure drop. Note that the pressure in OpenFOAM is not the real air pressure exactly, but is presented as the pressure divided by the density as shown in formula 4.24.

$$p_{OF} = p_{amb}/\rho \tag{4.24}$$

with the pressure definition in OpenFOAM (p_{OF}) and the ambient pressure (p_{amb}) and density ρ which equals 1.225 $[kg/m^3]$ in all simulations. The pressure drops over the second, third and fourth actuator discs are 63 %, 58% and 55% suggesting that the power loss in the downwind turbines stabilises and reaches a limit also observed by Barthelmie et al. [2009] and Bader et al. [2018].

In Figure 4.20 the turbulent kinetic energy, a direct measure of the level of turbulence, is plotted along the axis though the turbines. The expected result of increased turbulence behind the actuator discs can be seen. Although exact measurements of the turbulent kinetic energy between wind turbines in a wind farm is limited, Siedersleben et al. [2020] presented some interesting results for the turbulent kinetic energy induced by wind farms. Using both simulations and test flights next to and above the wind farms, turbulent kinetic energy values were measured of up to 2.5 m^2/s^2 in the strictest most downwind direction of the wind farm. This observation corresponds well with the turbulent kinetic energy levels that are obtained in this study. However, the test flight results show effects further downstream the last row of turbines, by which the turbulent kinetic energy value has already dropped in the range of 2.1 to 2.3 m^2/s^2. Kumer et al. [2016] provide results of turbulent kinetic energy measurements obtained with the application of Lidar. Measurements for three different cases were done of which one measurement case took place in the wake of wind turbines. Here values in the range of 2-2.5 m^2/s^2 were measured at hub height, directly behind the wind turbine rotor, and again well in line with our results in Figure 4.20.

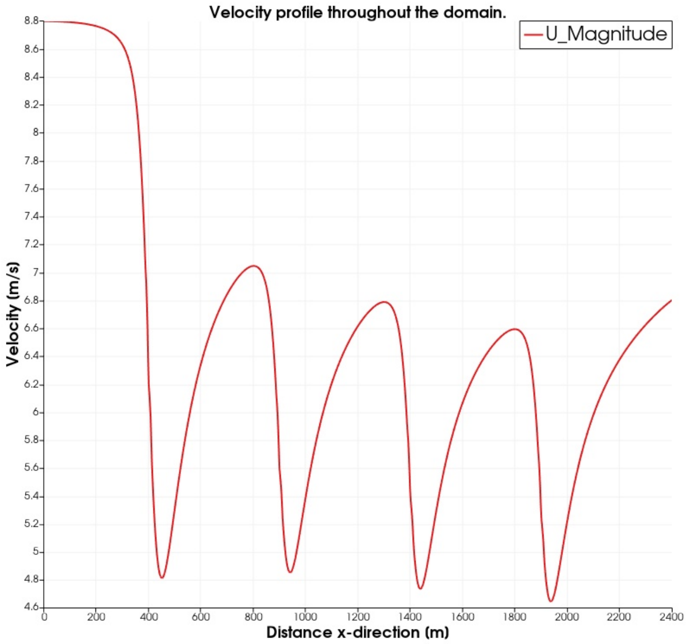

Figure 4.21: Line plot at hub height of the velocity throughout the domain.

Figure 4.21 shows the velocity plot at hub height through the domain and clearly demonstrates the wind velocity deficit induced by the actuator discs. Obviously, the actuator discs drop the velocity with a significant amount. The first disc drops the velocity with 45 %, whereas the second, third and fourth disc with a relatively similar amount of 30.9 %, 30.1 % and 29.6 %. This is not unexpected because the thrust and power coefficient for all four actuator discs are similar. The first disc experiences a much larger velocity drop because of the much higher incoming wind speed, and thus much larger thrust force. Apparently behind the four actuator discs, relatively similar levels of re-energizing takes place, which is confirmed by Figure 4.20 where similar levels of turbulence behind every turbine is observed. Re-energizing is induced by turbulence (and thus the increase in k) hence similar levels of re-energizing can be expected. However, the maximum velocity point is lowered for every disc. This will result in lower turbine power levels, because the power strongly depends on the incoming velocity (cubic dependency).

In Figure 4.22 - Figure 4.25 the wind velocity (in x-direction) as a function of height is presented for different locations: the upstream point (green) in front of every actuator disc, and at three locations beind the actuator disc, at respectively x_{disc} + 50 [m] (blue), x_{disc} + 200 [m] (yellow) and at x_{disc} + 400 [m] (purple) (which is the upstream point for the next actuator disc). Note that for the AD4, the most downstream wind velocity profile is located at the outlet end of the domain instead of at x_{disc} + 400 [m] to show the wake recovery near the outlet of the domain. Whereas for actuator disc 1 the velocity does not come close to re-energizing to the initial undisturbed vertical velocity profile, for actuator 2, 3 and 4, the wind velocity profile away from the actuator re-adjusts almost completely to initial incoming wind profile, showing very effective wake recovery. Especially for actuator disc 4, the wind velocity at 2350 [m] almost perfectly aligns with the vertical wind profile at the upstream point. Göçmen et al. [2016] and Schreiber et al. [2020] found similar vertical wind profiles directly behind the actuator discs that showed Gaussian velocity deficits in the near wake. Further down the far side of the wake, profiles like the ones shown in Figure 4.24 and Figure 4.25 for the downstream positions were found. Note that Schreiber et al. [2020] used double Gaussian velocity profiles showing two instead of 1 velocity minimum in the near wake, whereas further downstream, the wind showed similar vertical wind speed velocity profiles and in Figure 4.24 and Figure 4.25.

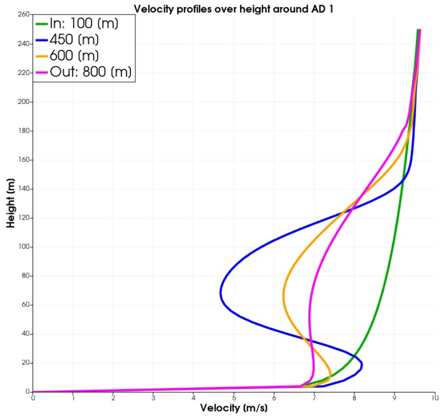

Figure 4.22: Vertical velocity profiles around AD1

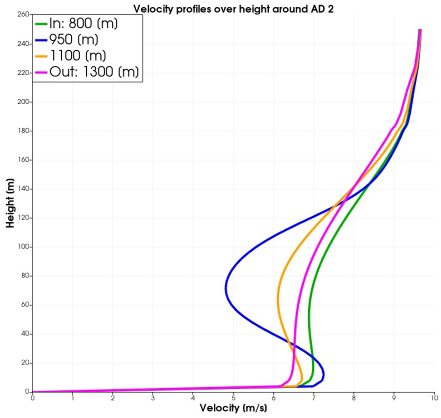

Figure 4.23: Vertical velocity profiles around AD2

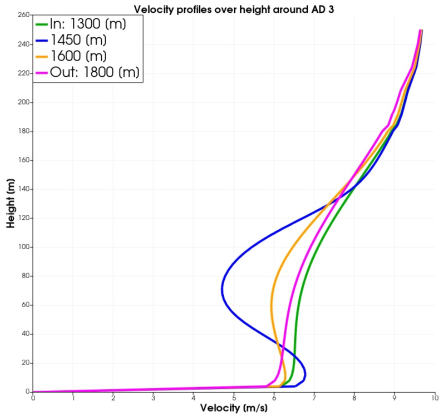

Figure 4.24: Vertical velocity profiles around AD3

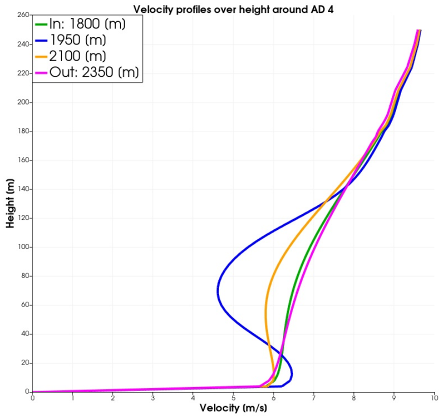

Figure 4.25: Vertical velocity profiles around AD4

Wind velocity values at the upstream point, thrust force values, power values and total wind farm efficiency for the base case are summarised in Table 4.6. As expected, the first turbine generates a much larger thrust force (55 %) than the second actuator disc because the velocity is almost a factor of 1.25 larger. As already explained, the power and thrust strongly depend on the spatial velocity in the monitored region (here the upstream point). The strong loss in velocity result in the logical power deficit outputs for the second (0,515 P_1), third (0,460 P_1) and fourth (0,422 P_1) actuator disc compared to the first actuator disc (P_1). The wind farm efficiency (η_{wf}) is calculated using equation 4.25 where P_i specifies the Power output for turbine i (P_i).

$$\eta_{wf} = \frac{P_1 + P_2 + P_3 + P_4}{4P_1} \tag{4.25}$$

	AD 1	AD 2	AD 3	AD 4
Upstream point velocity [m/s]	8,79	7,05	6,79	6,59
Thrust force [kN]	211	136	126	119
Power output [MW]	1,86	0,958	0,856	0,785
Efficiency wind farm [%]				**59,9**

Table 4.6: Base case simulation results for upstream velocity, thrust force, power output and efficiency

The efficiency of the base case wind farm equals 59,94 %. Barthelmie et al. [2009] studied the large off-shore wind farm Horns Rev off the coast of western Denmark. Taking into account that simulations of wind farms tend to overpredict wake losses, and over- or underpredict wake recovery, Barthelmie et al. [2009] compared results from different simulations software of wind farms to measured results in the Horns Rev wind farm. For the strictest wind direction (wind turbines in the wind farm aligned with the wind direction), results as summarised in Figure 4.26 were obtained.

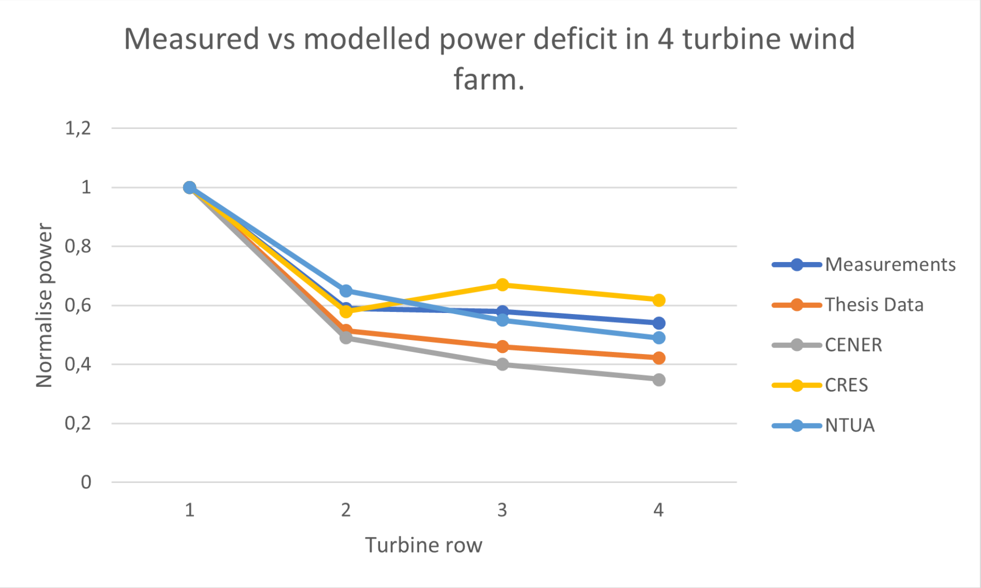

Figure 4.26: Comparison of wind farm power measurements and simulations results for power deficit of downstream wind turbines for the strictest wind direction. Adaptation of the work of Barthelmie et al. [2009]. Dark blue represent onside measurements. Orange represents results in this Thesis. Grey represents results of the CENER model that uses RANS and the k-ϵ model in CFD software Fluent. Yellow is based on the k-ω model and uses an implicit pressure correction scheme. NTUA CFD model uses 3D RANS with second order spatial accuracy, using the k-ϵ as turbulence closure model.

Comparing the results of the simulations in this work with the results found in the study done by Barthelmie et al. [2009], the same conclusions can be drawn. The power deficit curve of turbines 2, 3 and 4 lies between 2 of the wind farm simulation methods introduced in Barthelmie's study. As these two simulation methods also use RANS and the k-ϵ method with 80 [m] actuator disc turbines, the results of this base case is concluded to be valid. However, it is obvious that, compared to the black line which represent the measurements of the wind farm, the wind farm simulations using RANS tend to overpredict the wake losses, a phenomenon that is observed in many other studies (for example: Tabib et al. [2015]). Barthelmie et al. [2009] concludes that it is difficult to validate or compare wind farm simulation studies because the amount of onsite measurement data in wind farm wakes is very limited. More experimental data of wake losses for different wind farm geometries is required to calibrate wind farm simulation models. However, it can be concluded that the wind farm wake effects in this study are similar to literature wind farm simulation results. Hence, this model will be applied as a base case model to evaluate the effects of kites on the efficiency of our wind farm.

Velocity deficit

An interesting question when studying Figure 4.21 is whether the velocity deficit would eventually re-energize to its original value. Dong et al. [2021] recently showed using LES simulations that the wake of wind farms can still affect downwind turbines at a distance of 165D_{wt} behind a first turbine. However, at 55D_{wt} 95% of the wind velocity deficit had been re-energised. Tabib et al. [2015] carried out simulations for wind farms using both RANS and LES models. It was concluded in this research that the RANS model overestimates turbulence, resulting in faster wake recovery than for LES modelling. Also, higher power production levels were measured for wind turbines in RANS simulations than in LES simulations. An expected outcome of simulating a single actuator disc in OpenFOAM is for the wake recovery to be faster, requiring less than 55 D_{wt} for a 95% wind velocity deficit recovery. To evaluate the wind velocity deficit in our model, a single actuator disc simulation was carried out. A grid length of 5500 [m] was selected (400 m + 63.75D_{wt}) to ensure the recovery of the velocity in the wake could be studied over a large distance.

Figure 4.27 shows the wind velocity profile throughout the extended domain. A distance of 55 D_{wt} downwind the actuator disc a velocity of 8.6549 [m/s] was measured. Compared to the initial velocity, this is 98.35 % V which indeed is considerably higher than the 95% wind velocity deficit recovery found by Dong et al. [2021]. This supports the observation that RANS simulations result in faster wake recovery which is in line with the findings of Tabib et al. [2015]. Further more, it is noticable in the curve that the velocity tends to grow to a limit (which is expected to be the initial velocity). Even larger simulations are required to study the effects at 165 D_{wt} downwind of the rotor.

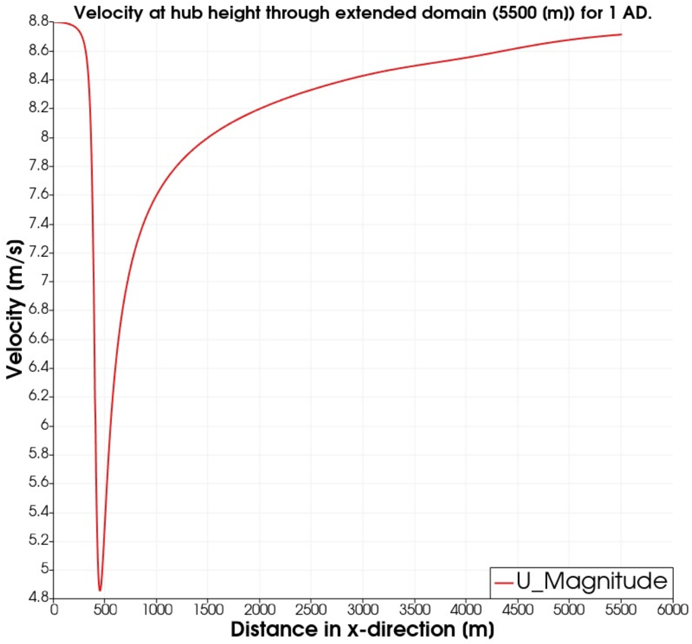

Figure 4.27: Velocity profile at hub height throughout an extended domain showing the wake recovery throughout the domain.

Case 2: Partial loading

As is clear from Figure 4.19, Figure 4.21 and Figure 4.22, the largest pressure and wind velocity drop is experienced by the first actuator. The first actuator therefore, produces at least twice as much power as the second, third and fourth. For Case 2, we evaluate the potential of cutting back actuator 1, thereby increasing power production in the downwind actuators yielding total wind farm efficiency increase. This Case presents an additional method to validate the wind farm simulations performed in this work.

Two methods of increasing wind farm efficiency through limiting power production of one or multiple wind turbines have been discussed in literature. One method uses yaw misalignment to redirect the wake away from downwind turbines, as shown by Van Dijk et al. [2016]. They conclude that, quoting, ”the simulation results show that partial wake overlap can significantly increase asymmetric loading of the rotor disk and that yaw misalignment is beneficial in situations where the wake can be sufficiently directed away from the downstream turbine”. For yaw misalignment angles of 5 and 10 degrees, total power increase is measured (up to 5.5%) and loading decreases on downwind turbines (up to 66%). Yaw misalignment is rather difficult to implement in the wind farm model in this study and has been researched fully by Van Dijk et al. [2016] already.

A second method limits the power output of the first turbine and checks if this could potentially gain enough power output for turbines 2-4 (or more for larger wind farms) so that wind farm efficiency is increased. This case studies this effect. Again, four turbines are located in a row, in downwind direction. This time, for the first actuator disc a lower induction factor of

0.17 is used (as proposed by Ploumakis [2015]) corresponding to power and thrust coefficients of $C_P = 0.468$ and $C_T = 0.562$ (equations 4.20 and 4.21).

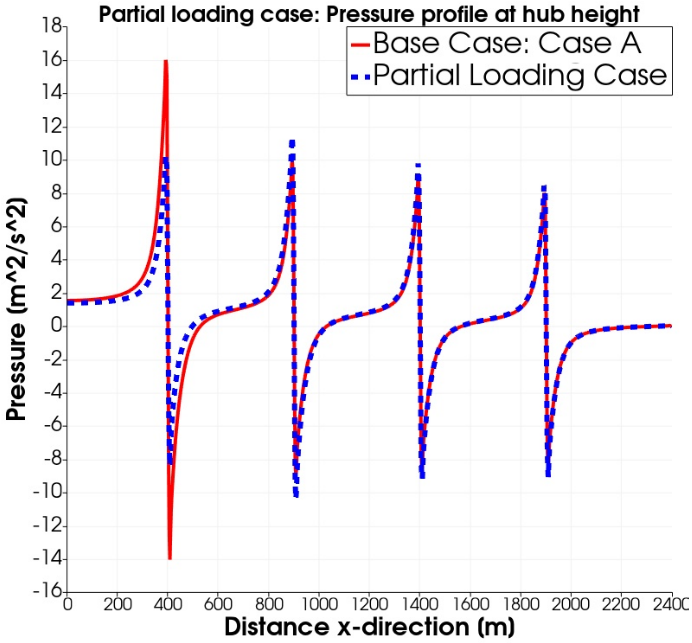

Figure 4.28: Pressure profile at hub height throughout the domain for the partial loading case

Figure 4.28 shows the pressure throughout the domain for the partial loading case and the base case. As expected, the pressure drop over the first actuator disc is lowered. This results in larger pressure drops for the other discs, thus enabling more power to be produced by downwind turbines. This reaches a limit though. Note that already at the fourth disc, the pressure drop is almost equal to the base case.

Figure 4.29 shows the turbulent kinetic energy through the domain. The decrease in loading decreases the turbulent kinetic energy behind the first rotor with a factor larger than two. Behind the second turbine, a slight decrease in turbulence is found as well, whereas behind the third and fourth actuator discs no significant difference in turbulence is observed. For a larger wind farm, equal turbulent kinetic energy can be expected for downwind rows of actuator discs.

Figure 4.30 presents the results for the velocity showing the velocity profile throughout the domain for the partial load case (case II) and the base case (case I). It is clear that enforcing partial loading on the first turbine increases the velocity at the upstream point (thus the power production) for the second, third and fourth turbine. As expected, this reaches a limit, as presented by Barthelmie et al. [2009]. They concluded that after the fourth row of wind turbines in a wind farm, changes in the streamwise velocity would not alter the power production of the downwind wind turbines anymore, and vertical transport of wind plays the most crucial method of re-energizing the wake.

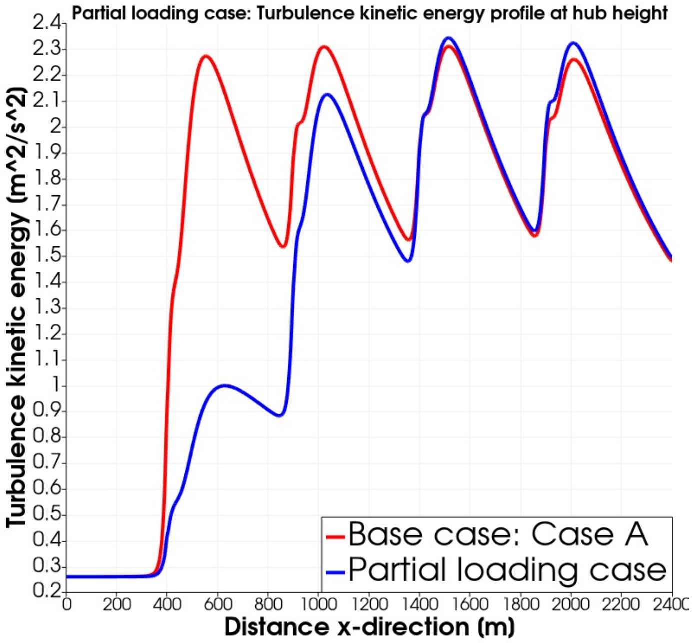

Figure 4.29: Turbulent kinetic energy profile at hub height throughout the domain for the partial loading case

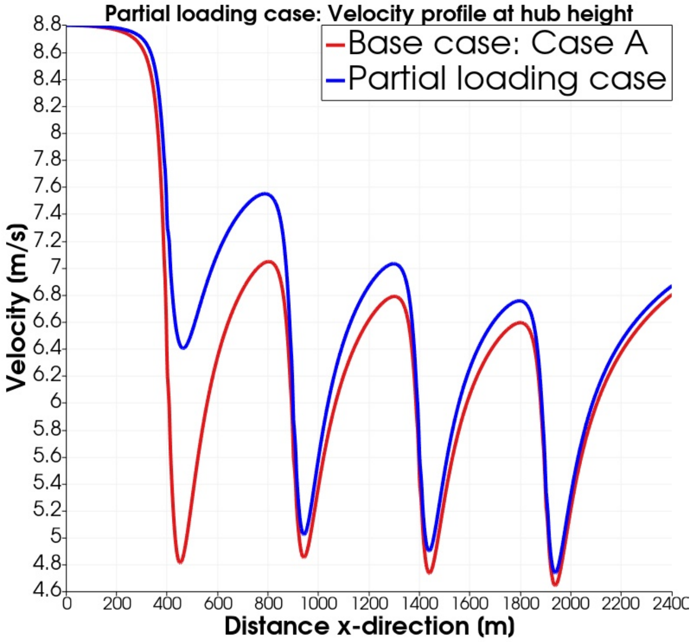

Figure 4.30: Velocity profile at hub height throughout the domain for the partial loading case

Table 4.7 shows the results for the partial loading case. Note that the efficiency strongly depends on the first actuator disc, and the efficiency, calculated using equation 4.25, is considered with respect to the power output of the first actuator disc. That is why this efficiency value can not truly be considered as a correct measure for the wind farm efficiency compared to the base case. A better method to compare the two cases is using the total power output. The base case considers a total power output of 4.4589 MW, whereas

	AD 1	AD 2	AD 3	AD 4
Upstream point velocity [m/s]	8.79	7.55	7.03	6.76
Thrust force [kN]	133	156	135	125
Power output [MW]	1.17	1.18	0.951	0.844
Efficiency wind farm [%]				**88.7**

Table 4.7: Partial loading for AD1 case results for upstream velocity, thrust force, power output and efficiency

the power output of the partial loading case equals 4.1380 MW. This shows that, even though the power output of the second, third and fourth disc has increased a lot (22.8%, 11.1% and 7.51% respectively) compared to the base case, the decrease in power output of the first turbine (-37.3%) still limits the total power output of the wind farm. It shows the obvious result that the optimal induction factor for all four turbines presents the highest total power output (and efficiency). In this work, the existence of a case where the decrease in power output of disc 1 equals or is smaller than the increase in power output of discs 2, 3 and 4, is questioned. Efficiency can be increased, however at a cost of total power output. A better calculation method for the efficiency of a wind farm with different loads should be found. Even though many accurate measurements of single turbines have been found (like Inoue et al. [2005]), calculations for wind farm efficiency using different induction factors for turbines is barely described.

A better efficiency comparison of the partial loading case to the base case can be found when using the same lower induction factor for all four turbines. Even though total power output will drop, as less power is extracted from the turbines under partial loading, wind farm efficiency is expected to increase. Table 4.8 show these results, and show exactly what is expected. Total power output equals 3.796 MW which is -14.86 % smaller than the base case, and -8.26 % smaller than the partially loaded AD1 case. However, efficiency increases a lot.

	AD 1	AD 2	AD 3	AD 4
Upstream point velocity [m/s]	8.75	8.00	8.02	8.02
Thrust force [kN]	131	110	110	110
Power output [MW]	1.15	0.878	0.883	0.886
Efficiency wind farm [%]				**82.9**

Table 4.8: Partial loading (for all four actuator discs) case results for upstream velocity, thrust force, power output and efficiency

Case 3

Case 3 uses a higher velocity throughout the domain. This case is relevant to evaluate the effects of a higher velocity at the kite influence on the wake. For that reason, the results for the higher velocity simulations are not discussed in much detail in this chapter, but will be discussed more widely in Chapter 5.

The velocity is set at 10 [m/s] instead of the 7.8 [m/s] wind speed used in Case I and II. This is based on findings by Coelingh et al. [1998] for wind speeds on the North sea. 7.8 [m/s] refers to the averaged wind speed throughout the wind at the Ijmuiden offshore wind farm, whereas 10 [m/s] is the average wind speed for the windiest wind sector in IJmuiden. The initial velocity condition is also changed to an initial wind speed of 10 [m/s] at 18.5 [m] reference height at the inlet. Note that the velocity of 10 [m/s] is taken at reference height, yielding a velocity of roughly 11.3 [m/s] at hub height (80 [m]) (see Appendix B Figure B.3). The actuator disc of 80 [m] D_{wt} is based on the Vestas V80-2.0MW (for details see Vestas [2013]) which has a rated wind speed of 16 [m/s]. A velocity of roughly 11.3 [m/s] at hub height is thus still underrated so no pitching action is necessary.

Appendix B shows the line plots for the pressure, turbulent kinetic energy and velocity at hub height throughout the domain. No unexpected outcomes are seen (in reference to the base case) so case III can be used as a base case for studying the effects of kites experiencing a higher velocity on the wake. Table 4.9 show the upstream velocity, thrust force, power output and efficiency for case III. Larger thrust force and power outputs are found (as their dependency on the velocity is squared and cubic respectively) but the efficiency only slightly decreases. This results from the fact that the percentage increases in thrust and power are almost similar, which is in line with the plots presented in Appendix B showing no unexpected results compared to the base case.

	AD 1	AD 2	AD 3	AD 4
Upstream point velocity [m/s]	11.272	9.0346	8.7017	8.4342
Thrust force [kN]	374.72	223.38	207.22	194.68
Power output [MW]	3.9195	2.0181	1.8032	1.6419
Efficiency wind farm [%]				**59.84**

Table 4.9: Higher velocity case results for upstream velocity, thrust force, power output and efficiency

5 KITE SIMULATIONS

In this chapter, the effects of kites on the wake flow in wind farms are studied using CFD software OpenFoam. Parameter studies of five kite parameters are performed. The effects of these parameters on the velocity and turbulent kinetic energy in the wake are compared with the base case model, containing no kites. The kites are modelled through the actuator line (AL) method and are located between the wind turbines. As a first step, a validation case is set up that tries to mimic the findings of Ploumakis [2015]. Next, in the first parameter study case A, four kite sizes are compared by introducing a single kite between the first and second wind turbine. One kite size is selected and used in the other parameter studies. In Cases B and C the effects of the kite's location are evaluated: both in height and downwind direction. Case D compares for different kite angles of attack. Using the results from Cases A-D, Case E introduces three kites in the wind farm and optimizes for wind farm efficiency increase. Finally, case F considers the effects of kites on the wake flow in a higher wind field.

5.1 ACTUATOR LINE METHOD

Harnessing power using kites from higher altitudes having more energetic wind flow is a novel method in the road towards a sustainable world. Using kites for non-direct electricity generation but for stimulating and re-energising the wake behind a wind turbine is an entire new field, as explained in Section 1.5. In the airborne wind energy sector the core use of kites is in direct electricity generation purposes. Computational models and representations for the kites studied in the airborne wind energy sector are already limited, however an additional difficulty is that the kite models that do exist represent direct electricity generating kites. Research on kites focuses on studying the (crosswind) motion of a single kite (Mano et al. [2014]), or detailed wind flow over the area of a kite (Pegg et al. [2020]). In these studies, an as accurate as possible representation of a kite is one of the main focuses, resulting in highly refined kite models. Performing simulations of the wind flow around these refined kite models require computational intensive processes. In this study, the exact wind flow characteristics around a kite's body is not the main focus so a more simplified kite model is introduced. The kite is represented using the actuator line method (AL). This is a novel representation of a kite and may provide a framework for future research on kite farms and the effects of kites on wind farms.

The AL method was introduced by Sørensen and Shen [2002] to study the three-dimensional flow fields around wind turbine rotors. Sorensen modelled the rotor blades as lines along which the total blade loading was distributed. This method proved to give detailed information on basic wake features like vortex structures. An additional advantage was the required mesh resolution to be lower and grid structure much simpler, compared to blade-resolved simulations, requiring lower computational cost. These advantages made the AL method quickly becoming a popular representation of wind turbine blades, having an advantage of presenting blades more accurate than the traditional AD model. Troldborg et al. [2012] compared the actuator disc (AD) method, the AL method and fully resolved rotor geometry for the representation of a wind turbine. Troldborg concluded that for a uniform wind inflow the AD and AL method were both in good agreement with the fully resolved rotor geometry simulation. For a turbulent inflow, the AL method and fully resolved rotor geometry model of the turbine were in good agreement. The AD method proved to be limited in representing turbulence in the wake.

Whereas the AD method specifies the thrust force over the entire disc area using a single force calculation, the AL method calculates the force over multiple so-called line segments. This gives a more accurate description of the force a turbine blade, or in this study a kite, places on the wind flow. With the additional advantage of requiring lower computational costs than a fully blade-resolved description of the kite, these arguments present the reasoning for the selection of the AL method to represent the kites.

The first step in using the AL method is shown in Figure 5.1. The kite is represented by a so-called actuator line. This actuator line is divided into actuator line segments. In the centre of every actuator line segment a control point is located. Over every line segment, the varying velocity is interpolated to a single velocity value represented by the control point. With these velocity values, a single velocity magnitude and angle of attack is calculated. Tabulated data of a wing or blade is then compared to the calculated velocity magnitude and angle of attack to find a corresponding lift and drag force. These force components are projected onto the mesh using a Gaussian projection function (note that different projection functions are possible as well, however the Gaussian projection has been proven by Sørensen and Shen [2002] to accurately project the force on the CFD mesh and is used by most researchers). Figure 5.2 shows the projection of an actuator line on the wind flow. For every segment a body force per unit volume is calculated using the lift and drag from the tabulated data which is then added to the N-S equations. (Churchfield et al. [2017])

5.2 TURBINESFOAM

The AL method was introduced in OpenFOAM through the turbinesFoam library created by Bachant et al. [2016] to study vertical axis wind turbines. The research group used both the k-ϵ RANS and Smagorinsky LES turbulence models for validation of the turbinesFoam library while investigating the

Figure 5.1: Representation of the actuator line method for a power kite. The kite is represented as a so called actuator line. Adapted from Bubba, O [2014].

fast wake recovery of vertical axis wind turbines. The turbinesFoam library provided accurate results for the mean power coefficient of the turbine and some important flow features that contribute to the fast wake recovery of the turbine. It was concluded that the turbinesFoam library could be used for future research of horizontal and vertical wind turbines, as well as other blade-like applications (like hydro turbines and kites). Since then, many papers have been published that use the turbinesFoam library for different applications.

The turbinesFoam library provides fvOptions classes (like the AD method for turbines) for adding the actuator lines and actuator line segments to the solver. The force specified by the actuator line is determined using the following force equations:

$$F_l = \frac{1}{2}\rho A_{\text{elem}} C_l \left|\vec{U}_{\text{rel}}\right|^2 \tag{5.1}$$

$$F_d = \frac{1}{2}\rho A_{\text{elem}} C_d \left|\vec{U}_{\text{rel}}\right|^2 \tag{5.2}$$

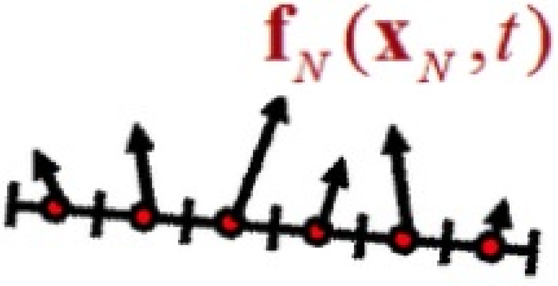

Figure 5.2: Actuator line method: Splitting the actuator line in line segments for which force components are measured (Motta-Mena et al. [2014]).

where U_{rel} presents the local relative velocity projected onto the plane of the element profile, and A_{elem} represents the blade area using the following equation:

$$A_{elem} = bc_{kite} \tag{5.3}$$

with wing span (b) and kite chord length (c_{kite}). These forces are then summed and added to the N-S equations equations as a body force per unit volume.

As described in Section 5.1 some preliminary values are required to look up the lift and drag values from the tabulated data of a chosen wing. The incoming velocity and angle of attack are the values required to find and calculate the lift and drag forces. For an uniform wind flow this value simply equals the velocity throughout the domain. In the case of this work, the velocity is measured at the kite's surface. This thus depends on the kite's height as the velocity changes over height following the logarithmic ABL profile. An initial angle of attack is specified by the user through the so-called pitch angle. The pitch angle is often defined as the the angle between the chord of an airfoil and a level surface (i.e. the ground). Note that the angle of attack of a kite is the angle between the chord of the kite and the incoming velocity. These angles are not the same, however the pitch angle provides a good first estimate for the angle of attack in this study because the velocity is also introduced horizontally. Explained in Section 2.2, the downwash induced by the kites decreases the initial angle of attack (pitch angle) to the effective angle of attack because the apparent velocity is tilted slightly after introduction of the vertical velocity component.

With the angle of attack and velocity measured, the lift and drag coefficients are interpolated from tabulated data of a wing. In the case of this work, the Clark Y wing profile was used based on measurements by Spera [2008] using the Aerodas model. Quoting Spera [2008]: "To date, model calculations of lift and drag coefficients are in close agreement with a large quantity of reference test data for a wide variety of airfoils. Calculations of wind turbine power and fan pressure rise based on AERODAS lift and drag coefficients are also in close agreement with test data." The Aerodas model thus provides a good method of tabulated data for a wide variety of airfoils. The Clark Y wing profile, one of the wings specified using the Aerodas model, was selected in this work as it provides the most general case of wings while presenting lift and drag coefficients that can be used to represent kites with a wide variety of aspect ratios. The measurements of the lift and drag coefficients for angle of attack of the Clark Y wing were performed at a lower Re number than is the case in the simulations in this study. Comparing the tabulated lift and drag coefficients with higher Re measurements, for example by Morgan et al. [1987], similar lift and drag coefficients are found. For this reason the Clark Y wing profile is assumed valid for this study and used throughout this Thesis. The Clark Y wing profile (and the wing profiles studied by Morgan et al. [1987]) are valid for aspect ratios of 2-6. Figure 5.3 presents the tabulated data for the Clark Y wing profile. It presents curves for the dependency of the lift and drag coefficients on the angle of attack. Interpolation is used to find lift and drag coefficients for specific angles of attack, the process shown in the figure below: (Note that the critical angle of attack explained in Chapter 2 is clearly visible given by the angle of attack after which the lift coefficient drops rapidly.)

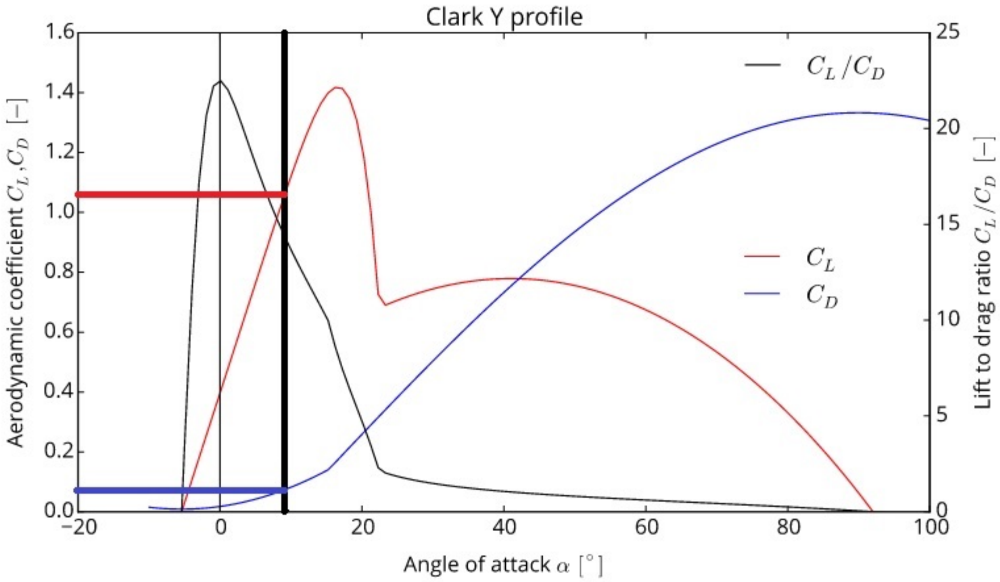

Figure 5.3: Clark Y wing profile for lift and drag coefficients based on angle of attack. An adaptation is made to show how for different angles of attack the lift and drag coefficients are interpolated (Spera [2008]).

The kite is presented in fvOptions as an so-called airfoil. The code is shown in a screenshot below:

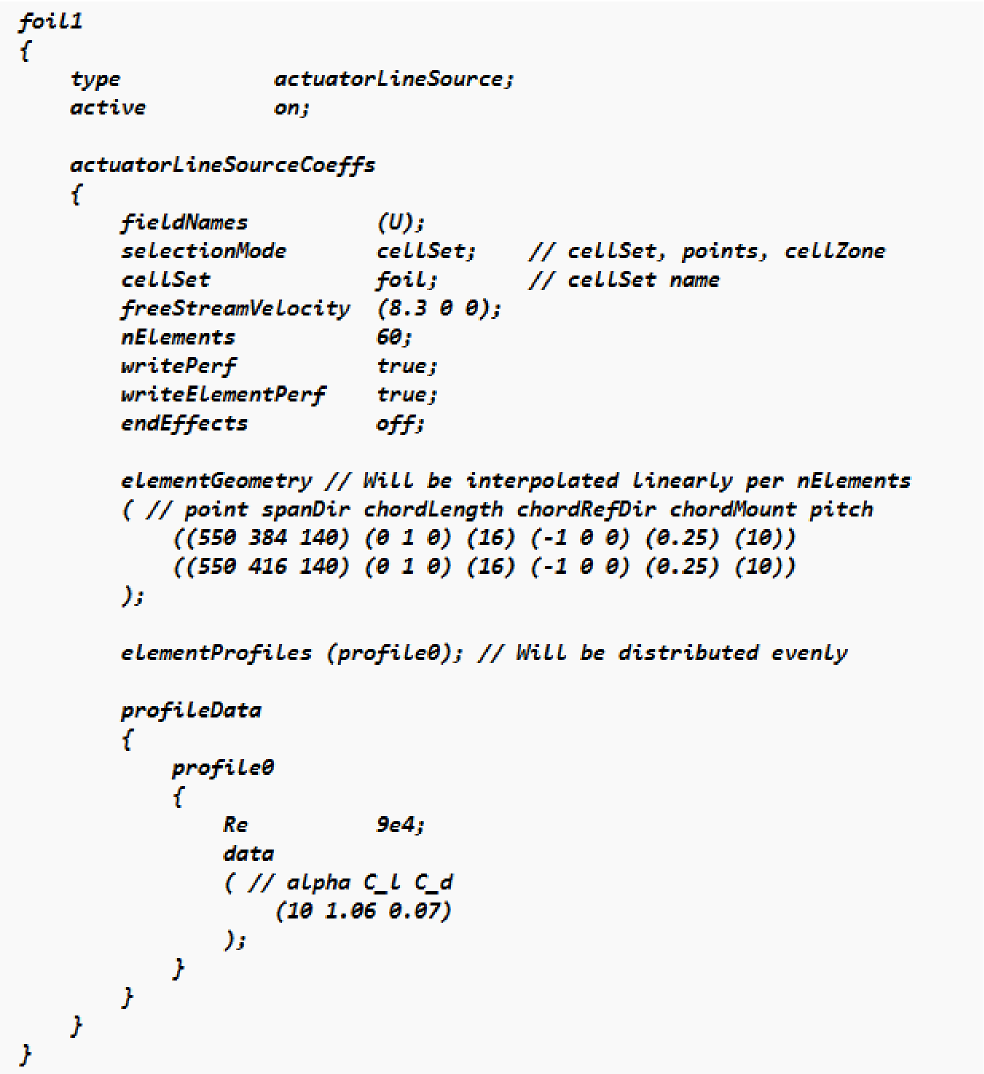

```
foil1
{
    type            actuatorLineSource;
    active          on;

    actuatorLineSourceCoeffs
    {
        fieldNames          (U);
        selectionMode       cellSet;    // cellSet, points, cellZone
        cellSet             foil;       // cellSet name
        freeStreamVelocity  (8.3 0 0);
        nElements           60;
        writePerf           true;
        writeElementPerf    true;
        endEffects          off;

        elementGeometry // Will be interpolated linearly per nElements
        ( // point spanDir chordLength chordRefDir chordMount pitch
            ((550 384 140) (0 1 0) (16) (-1 0 0) (0.25) (10))
            ((550 416 140) (0 1 0) (16) (-1 0 0) (0.25) (10))
        );

        elementProfiles (profile0); // Will be distributed evenly

        profileData
        {
            profile0
            {
                Re          9e4;
                data
                ( // alpha C_l C_d
                    (10 1.06 0.07)
                );
            }
        }
    }
}
```

Figure 5.4: Fvoptions coding for the actuator line representation of a kite.

The freeStreamVelocity is the unaffected velocity at the kite height determined using the ABL simulations of Chapter 4. nElements specifies the amount of actuator line segments the actuator line is divided in. Churchfield et al. [2017] states that an actuator line is typically split into 40-60 segments, based on the length of the line and the different line sizes that are to be compared. In this work, for a smaller sized kite (having a lower span length) the line will be split into 40 segments, whereas the largest sized kite will be split into 80 segments. Note that the amount of line segments increases computational costs as more line segments require more force computations to be performed. In the elementGeometry coding, the actuator line is specified using the start and end point of the actuator line, the span direction, the chord length, the chord reference direction, the chord mount and the initial angle of attack (pitch). In this study, the kite is introduced perpendicular to the wind direction (in y-direction) with the actuator line specified at the quarter-chord length (defined by the chordMount). With the trailing edge located downwind of the leading edge, the chord direction is chosen in opposite direction of the wind direction. The profileData specifies the lift and drag coefficients for the angle of attack of the chosen wing. Note that in this screenshot the data is limited to a constant angle of attack of 10 degrees to limit the size of the snapshot. Lift and drag coefficients are found from literature for every 2 degrees angle of attack (AoA) difference. Other angles are interpolated from this data.

5.3 KITE SIMULATIONS CASE SETUP

With respect to the wind farm case setup in Section 4.2.3, the grid has unchanged. The domain is sized d_x x d_y x d_z by 2400 x 800 x 800 [m]. A refinement box is located in the centre of the box ranging from 0 to 2400 [m] in the x-direction (the total length of the domain), from 350 to 450 [m] in the y-direction and from 0 to 180 [m] in the z-direction. The actuator discs remain located at x=400 [m], x=900 [m], x=1400 [m] and x=1900 [m], in the centre of the width of the domain (400 [m]). D_{wt} = 80 [m] and the discs rotor is located at z=80 [m]. The sweep area of the disc thus ranges between y= 360 - 440 [m] and z= 40 - 120 [m].

The boundary conditions of the domain remain unchanged from those specified in Table 4.2 and Table 4.3. The fvOptions AD representations of the turbines remain similar to the case specified for constant power coefficients and thrust coefficients for all actuator discs, the so-called base case (Case 1: optimal induction factor). The kites are added in the fvOptions, described in the section above, at locations specified in the next section.

With the wind farm cases numerated by number, the kite simulation cases will be numbered by letters.

5.3.1 Validation: Comparison to literature

The master thesis of Ploumakis [2015] is the only study done towards using kites for re-energizing wakes in wind farms (as far as is known to the writer). As Ploumakis could not validate his results in any way, an interesting question arises whether similar results will be found when using a different turbulence model and a more complex kite representation. For this, before starting any parameter studies, a case is set up using the (sometimes questionable) parameters selected by Ploumakis to check for similar results. Table 5.1 specifies the different and similar parameter choices for the cases in this work and the work of Ploumakis. Note that for the simulation case that is compared with the work of Ploumakis, as much parameters and methods are set similar to the work of Ploumakis to achieve an as similar simulation case as possible.

	This work	**Ploumakis' work**
Software	OpenFoam	Ansys Fluent
Domain length	2400 [m]	2240 [m]
Domain width	800 [m]	800 [m]
Domain height	800 [m]	800 [m]
Turbine spacing	500 [m]	480 [m]
Reference velocity	7.8 [m/s]	7.8 [m/s]
Reference height	18.5 [m]	140 [m]
Surface roughness factor	0.0002 [-]	0.1 [-]
Kinematic viscosity	1.5E-5 [m^2/s]	1.79E-5 [m^2/s]
Aspect ratio	2 [-]	3.85 [-]
Nelements	40-80 [-]	28 [-]
Initial angle of attack	10 [°]	10 [°]
Initial velocity	7.8 [m/s]	8.5 [m/s]
Kite height	140 [m]	140 [m]
Kite downstream location	Centre between turbines	Centre between turbines
Coarse grid cell size	8x8x8 [m]	8x8x8 [m]
Refinement region	Block in entire domain	Small area around kite
Refined block cell size	4x4x4 [m]	1x1x1 [m] - 4x4x4 [m]
Turbulence model	RANS	LES
Actuator disc model	Froude's one-dimensional	Variable scaling
Kite representation	Actuator line model	Calculated pressure jump

Table 5.1: Table presenting a comparison between the parameters and methods selected by Ploumakis and this work. Note that for this validation case, as many parameters are set equal to the values selected by Ploumakis.

The purpose of this section is to compare the velocity increase in the wake and wind farm efficiency increase found in one of Ploumakis' cases with a case set up to closely resemble his case. For that reason, the reasoning behind some of the parameters chosen by Ploumakis are not questioned though a few remarks (on parameters and methodology) are summarised:

1. Ploumakis envisions his simulations to represent off-shore wind farms, though the ABL simulated by Ploumakis does not fall in line with an ABL expected over seas and oceans. The reference velocity at reference height is lower than is generally estimated, and the surface roughness factor chosen of 0.1 is in the order of on-shore roughness factors instead of desired ocean roughness factors.

2. The pressure jump generated by the kites is calculated by Ploumakis using the work of De Wachter [2008]. These calculations are based on an aspect ratio of 3.85 of the ram-air wing studied by de Wachter. Additionaly, de Wachter used an angle of attack of the kite of 12 degrees. Interestingly enough, Ploumakis states a similar aspect ratio and angle of attack is used throughout his work, however kites sized 8x16 [m] and 16x32 [m] are used throughout his work that have an aspect ratio of 2 and an angle of attack of 10 degrees (as is the case in this work).

3. For efficiency calculations, Ploumakis uses equation 4.25 as well. A limitation of this equation is the strong dependency on the power out-

put of the first turbine. He mentions this in the section about wind farms, and states: "The total extracted power from the domain will be the parameter to used for comparison between simulations". However, in the kite simulations, the efficiency increases (compared to a base case) are regarded as kite effects, even though the power output of the first turbine is limited which increases total wind farm efficiency (shown in this work in Case 2 of the wind farm simulations). Stating the efficiency increase is caused solely by kites is thus unjustified.

4. The refinement levels around the kites resulting in grid cells of 1x1x1 and 2x2x2 [m] will present the flows around kites more accurately than is the case in this work (where a refinement grid cell size of 4x4x4 [m] is used). However, keeping the grid cells coarse between the turbines and the flow between the wake and the kites might limit the downwash effects experienced in the wake. Coarser grid cells average flow properties over a larger volume, thus damping out effects in a small part of such volume.

Whereas the software and turbulence model used in this work is difficult to change for this validation case, most other parameters are changed to the parameters selected by Ploumakis. The main differences between Ploumakis' case and this validation case are as follows:

1. The refinement region of an entire block throughout the domain is used instead of small refinement regions around kites and no refinement regions in the wake.

2. Froude's one-dimensional actuator disc representation is used instead of the variable scaling method. The main difference is that the variable scaling method updates the power and thrust coefficients using the velocity measured at the actuator disc area, instead of further upstream (at a user-specified location). The variable scaling method is regarded as more accurate, and using Froude's one-dimensional actuator disc method is a limitation of this research.

3. The actuator line model, regarded as a more complex and accurate blade representation than a pre-calculated pressure jump, is used to represent the kites in this work.

All other parameters and methodology choices are similar. Three kites, sized 105 [m^2] with an aspect ratio of 3.85 are introduced in the system at a height of 140 [m] exactly centred between the actuator discs (so at x=650 [m], x=1150 [m] and x=1650 [m]). A snapshot of a slice of the domain is presented in Figure 5.5, showing the locations of the kites and actuator discs.

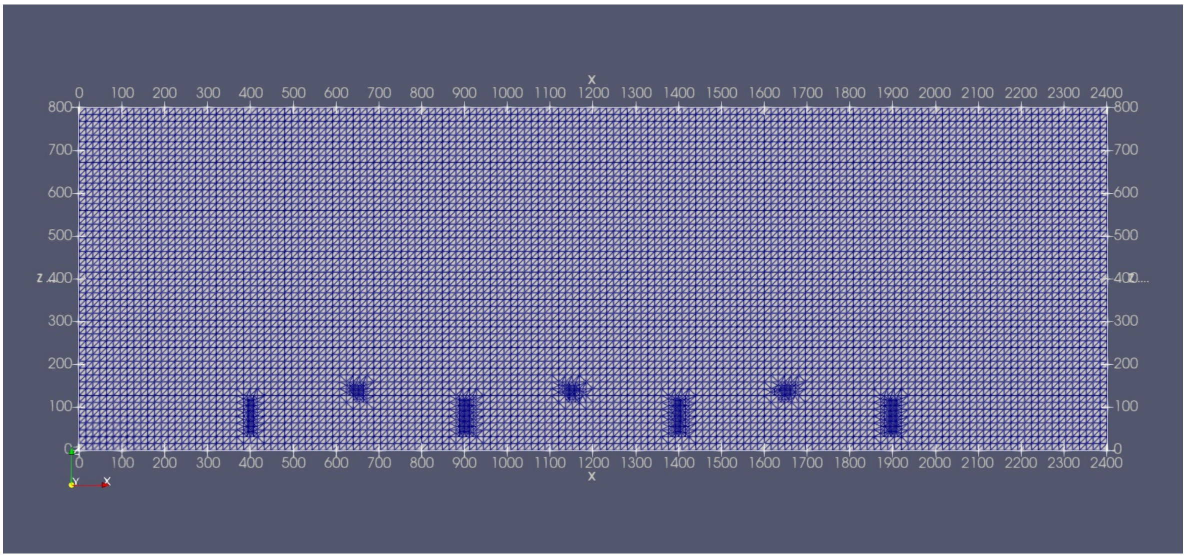

Figure 5.5: Snapshot of a slice through the centre of the domain (x-z plane) showing the locations of the turbines and kites. Note that the locations are shown using refinement regions whereas the simulations consist of a single large refinement block enveloping all regions of interest. The refined cells here are thus purely used for illustrative reasons.

The forces induced by the kites and the effects on wake velocity and wind farm efficiency increase are compared to results found by Ploumakis in Section 5.4.1. The effects on velocity increase and wind farm efficiency are measured by comparing the simulation with kites to a simulation without kites (thus only containing actuator discs).

5.3.2 Parameter study Case A: Kite sizing

Case A focuses on selecting a kite size to be used in the other parameter study cases in this chapter. Ploumakis [2015] already proved the expected result that a larger kite generates a larger forcing on the wind flow, inducing a larger downwash and re-energizing the wake stronger. This expected outcome will be validated with the new AL representation of the kite in case A.

Four different kite sizes were chosen, all having a similar aspect ratio of 2. The smallest kite size is based on the kite size of the Falcon kite of the startup Kitepower (Kitepower [2016]). Kitepower is a leading start-up in airborne wind energy based in Delft. The Falcon kite has a projected area of 47 squared meters. The second and third kite are based on the kite sizes introduced by Ploumakis [2015]. Ploumakis' kite size is used in the validation case and has an area of 8x16 [m] and the medium kite is sized 16x32 [m]. Finally a large kite of 32x64 [m] (2048 m^2) is introduced.

To capture wind from the unaffected boundary layer, the kites are expected to perform best at heights above the wake of the wind farm. Ploumakis [2015] did not focus on studying the effects of kite height and downstream location and decided to locate the kites at a height of 140 [m]. As cases B and C study the effects of height and downwind location respectively, for case A, the kite is located at this height of 140 [m] as well. The turbinesFoam class assumes an initial angle of attack of 10 degrees which is set constant for the entire actuator line. When the exact wind flow around an airfoil is not the main focus of a research using the actuator line method, this angle of attack of 10 degrees is often chosen. This is the case because a 10 degrees angle of attack is generally estimated to be a good angle of attack for the wide variety of wings (of both a turbine and a kite) used throughout literature. Thumthae and Chitsomboon [2009] provided evidence for this estimated optimal angle of attack by optimizing the α for untwisted blade wind turbines. Note however, that the angle of attack for the actuator line does not remain constant at 10 degrees but changes with the different velocities measured at the line segments.

The effect of a single kite on the wake between the wind turbines is studied and compared for the four different sizes. This kite is located in the middle between the first and second wind turbine (at a downwind location of 650 [m]) at a height of 140 [m].

5.3.3 Parameter study Case B: Kite height

In case B the focus is shifted towards the kite height. The selected kite size of 2048 [m^2], clarified in Section 5.4.2, is used and located at heights varying between 120 [m], the highest point the turbine blades reach, to 180 [m], far above the wake. Again, the effects of a single kite is studied, located at x=650 [m] exactly in the middle between AD1 and AD2.

With increased height comes higher valued and more uniform wind. An expectation is therefore that a kite flying at greater heights induces a larger downwash velocity. However, locating the kite too high is expected to reduce the effects on the wake recovery as the downwash will increase the wind flow between the kites and the actuator discs instead of re-energizing the wake between the turbines. It is expected that an optimal kite height close to the wake height is found which is studied in this case. Kite heights of 120 [m], 130 [m], 140 [m], 160 [m] and 180[m] are selected and their effects compared. Case E uses conclusions drawn in this section to find an optimal kite farm configuration for maximum efficiency increase.

5.3.4 Parameter study Case C: Downstream kite location

Case C uses the same size and optimal height (having the largest effect on all 3 ADs) of 130 [m] found in Section 5.4.3 to introduce a single kite at varying downstream locations between AD1 and AD2. It is expected that locating a kite close behind the first AD has the largest effect on re-energizing the wake for AD2. On the other hand, locating the kite close in front of AD2 might have a larger effect on re-energizing the wake for AD3 and AD4.

The kite is located at x = 425 [m] (directly behind AD1), x = 540 [m], x = 650 [m] (centred between AD1 and 2), x = 760 [m] and x = 875 [m] (directly in front of AD2). Note that x = 875 [m] is behind the upstream point of AD2 limiting the effect on power increase (as the velocity at the upstream point is not positively affected by the kite). So the velocity profiles at AD3 and AD4 are of importance in this section. Additional vertical plots are shown as well of the velocity at the upstream point.

5.3.5 Parameter study Case D: Angle of attack variation

In case D the effect of changing the initial angle of attack of a kite is studied. A single kite sized 2048 [m^2] is introduced at x = 650 [m] (between AD1 and AD2) and at kite height z = 130 [m]. Angles of attack of 6, 10, 12, 14, 16 and 18 are studied.

The downwash velocity is mainly dependent on the lift force, and thus the lift coefficient. This is the case because the drag coefficient is at least a factor of 7 lower than the lift coefficient. For this reason, the expected result is an almost linear relationship between angle of attack increase and wake recovery level, up to the critical angle of attack. This results from the linear increase of the lift coefficient between angles of attack of 6 to 18 [degrees], see Figure 5.3. However, drag increases exponentially with increased angle of attack. Drag opposes the wind velocity (and thus wake velocity) so for high angles of attack, drag forces may reduce the effects of kites on the wake flow.

5.3.6 Optimization problem Case E: Kite farm optimization

In Case E, a kite farm is simulated introducing kites between every turbine pair. The parameter studies in Cases A-D are used to simulate the so-called most optimal kite farm layout. Power production and efficiency values are compared to the Base Case (so without kites) to quantify the largest efficiency increase using kites modelled through the AL method.

The kites are located 25 [m] behind ADs 1, 2 and 3, at a kite flying height of 130 [m]. They are sized 2048 [m^2] (32x64 [m]) and have initial angle of attack of 18 degrees.

5.3.7 Parameter study Case F: Wind velocity

Case 3 in Section 4.2.4 sets a base for evaluating the effects of kites using a higher velocity throughout the domain. To compare the effect of kites in a two different velocity flows, 4 simulations are required: a simulation of a wind farm (and no kites) in a lower velocity field (**Case F1**), a simulation of a wind farm (and no kites) in a higher velocity field (**Case F2**), a simulation of a wind & kite farm in a lower velocity field (**Case F3**) and a simulation of a wind & kite farm in a higher velocity field (**Case F4**). The increase in wake velocity of Cases F1+F3, and Cases F2+F4 is then studied and compared.

Cases F1 and F2 have already been set up in Section 4.2.4 where Case F1 = Wind Farm Case 1: 4 ADs in a wind flow having an u_{ref} of 7.8 [m/s] at a z_{ref} of 12.5 [m]. Case F2 = Wind Farm Case 3: 4 ADs in a wind flow having an u_{ref} of 10 [m/s] at a z_{ref} of 12.5 [m]. Next, similar located kites in the two different wind flows are simulated. The three kites are introduced at a kite flying height of 140 [m] centred between every turbine pair (so at x = 650, x = 1150 and x = 1650 [m]). All kites haven an initial angle of attack of 10 degrees and are sized 2048 [m^2].

5.4 KITE SIMULATION RESULTS

5.4.1 Validation: Comparison case results

In Section 5.3.1 the validation case is described, comparing this Thesis' work with the only other study on kite use for wake recovery purpose. As Ploumakis [2015] was not able to validate his results with any other research, this thesis will be first in validating his results.

Two simulations are done: one containing 4 turbines without kites, and one in which 3 kites are located in the middle between the turbine pairs. Figure 5.5 shows the locations of the turbines and kites for the second simulation. Figure 5.6 shows the velocity line plot at hub height (80m) throughout the domain.

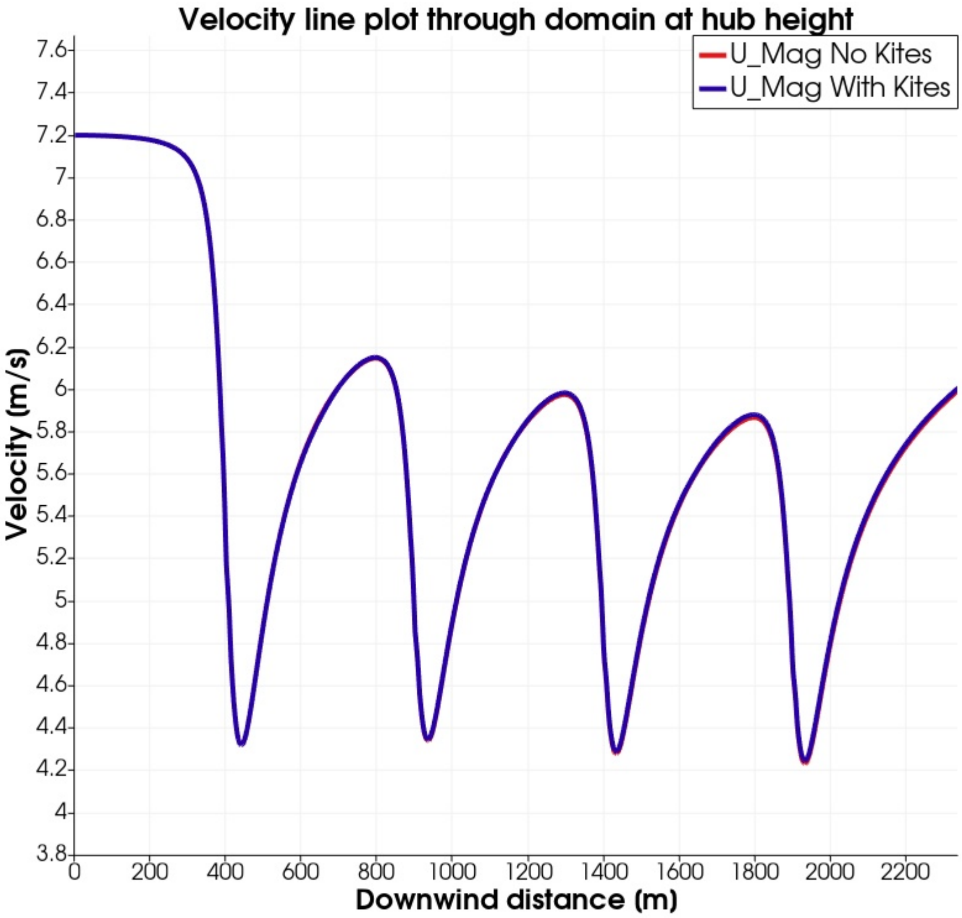

Figure 5.6: Velocity lineplot at hub height (80m) throughout the domain for the base simulation (no kites) and the simulation containing kites. These simulations are based on, and as closely identical to, the simulation specification of Ploumakis [2015].

Immediately noticeable is that the two lines almost overlap completely (hardly visible but for AD3 the no kites plot lies a little underneath the simulation containing kites plot). Zooming in on the two curves for AD2 (where the effect of using kites should be visible) gives the following plot:

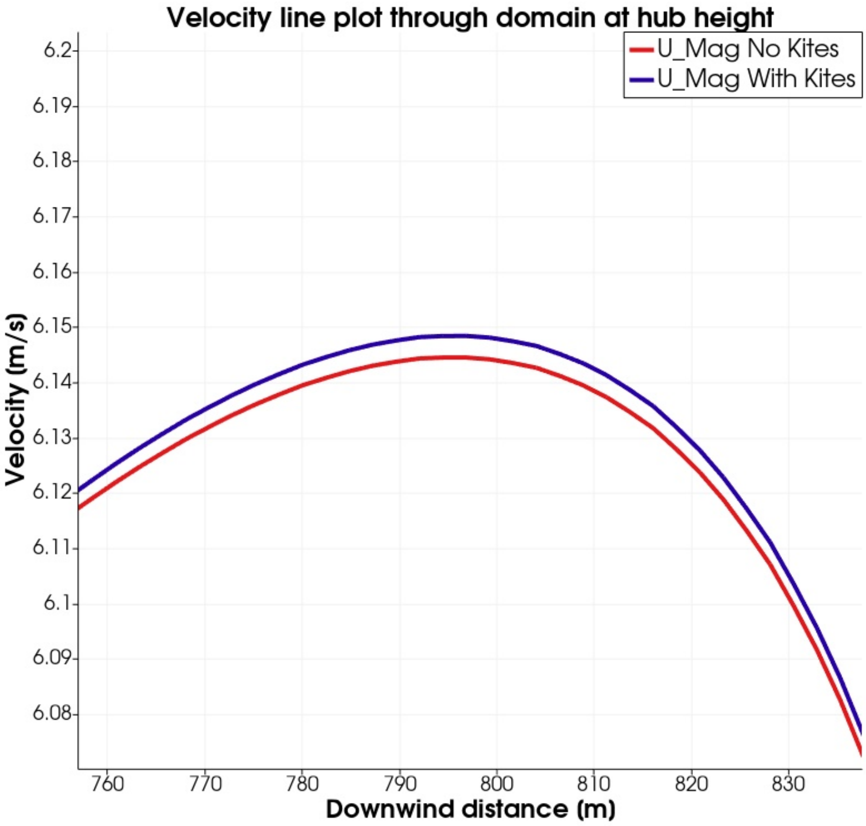

Figure 5.7: Zoomed in velocity lineplot at hub height (80m) around the upstream point of AD2 where the effect of kites on the wind flow should be noticeable, according to the work of Ploumakis [2015]. Curves for the simulation with no kites, and with kites are both shown.

An increase in velocity of 0.0065 % is seen, which would result in a 0.20 % increase in power output of turbine 2. This shows the unexpected result of an almost non-existing influence of the kites on the wind velocity at hub height. In Ploumakis' work, especially the power output of the third turbine increased a lot (with 14%), requiring a large velocity increase at hub height. This is clearly not the case in Figure 5.6, and the question arises what causes the differences between Ploumakis' work and this study.

One important parameter to compare between the two studies is the force generated by the kites. OpenFOAM calculates the forcing of the kites based on the incoming velocity. The source code of the turbinesFoam library enables the user to note values for the force vector generated by the kites. A comparison between the force magnitudes of the kites in Ploumakis' and this work is presented below:

	Kite forcing this work	Kite forcing Ploumakis' work
Kite 1	2101 [N]	4095 [N]
Kite 2	1966 [N]	4095 [N]
Kite 3	1903 [N]	4095 [N]

Table 5.2: Table presenting a comparison between the forces induced on the wind flow by the kites in this work and the work of Ploumakis.

Table 5.2 provides two interesting results:

1. The forces induced by the kites are around a factor 2 smaller than in the work of Ploumakis.

2. The forces in Ploumakis' work are constant and predetermined and do not depend on the incoming velocity. Ploumakis thus does not account for any flow distortion by up-wind kites which is questionable, as the kites are predicted to be able to steer the unaffected boundary layer downwards and re-energize the wake. The kites are meant to affect the wind flow at kite height, so they are expected to affect the velocity incoming at downwind kites.

In this work, the incoming wind velocity at the kite surface affects the kite forcing the most so additional line plots showing the velocity throughout the domain for different heights are shown below:

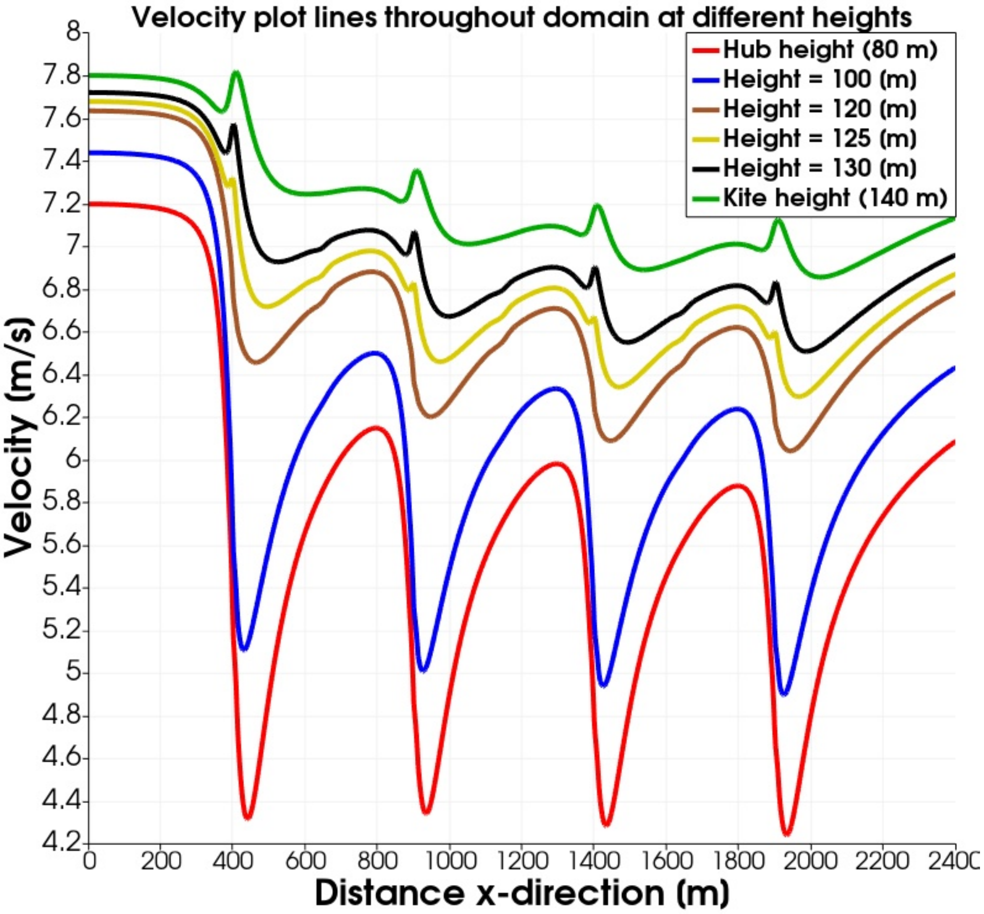

Figure 5.8: Line plots for the velocity in x-direction throughout the domain at different heights. Note that the legend specifies at which height the velocity is plotted throughout the domain.

One immediate explanation for the lower kite forces can be seen in the green line plot showcasing the velocity plots at kite height. The velocity at kite height decreases significantly before the kite force through the AL method is calculated and induced on the wind flow. As described in Section 5.2 the lift and drag forces are calculated using the local relative velocity projected onto the plane of the element profile. So the incoming velocity is lower than the desired velocity of 7.8 [m/s] at kite height, used in the work of Ploumakis. This velocity drop at kite height is caused by the wake effects of the turbines: the expansion of the streamtube and the lower velocity wind flow that accompanies the tube. The small velocity increases at the actuator disc's locations in the yellow, black and green line plots (so above the max tip height of the blade) show a questionable result for which no immediate physical explanation can be given. It appears that the turbulence model gives a weird fluctuation in the velocity before dropping because of the turbine wake effects. It may be caused by a limited grid resolution or domain height but requires future research to find an exact reason for this fluctuation. The velocity line plots through the sweeping area of the turbines do not show this effect, so it seems like it does not affect any power and efficiency calculations for the wind farm.

Other explanations for the lower kite forces may result from the different methodologies used throughout the two works. Having no other literature to compare these results with makes it difficult to find exact reasons why. This uncertainty gives rise to the necessity of more research to be done in the future so that the work done so far (Ploumakis' work and this study) can be validated.

The difference in forcing is only a factor 2, whereas the difference in the effect of kites on the wake velocity is multiple factors (up to a factor 16) larger[1]. Explanations for this large difference in effect may come from the questionable choices of the methodology used by Ploumakis explained in Section 5.3.1, however a first conclusion can be drawn. This concludes that the AL representation of the kites gives considerable different results than the pre-calculated pressure drops used by Ploumakis [2015]. One question that arises is what kite size should be needed before a substantial increase of wake velocity is reached. This will be the main focus of Section 5.4.2.

5.4.2 Parameter study case A results: Kite sizing

With the conclusion that the effects of kites on wind farm wake recovery is limited, a parameter study is done towards kite sizing. With cases B-F studying different parameter settings of the kite, a kite size should be found that clearly impacts the wind farm wake. Then, the effects of changing the kite parameters can be visualised and regarded as substantial, instead of being caused by uncertainty introduced by physical modelling errors, discretization errors, programming and computer round-off errors. As described in Section 5.3.2 4 different sized kites are introduced at a height of 140 [m] in between AD1 and AD2 at x=650[m]. Note that the turbines are located at

---

[1] These factors are calculated by comparing the kite induced wake velocity increase for all ADs in the work of Ploumakis [2015] with this work. The factor 16 is calculated for AD3.

x=400[m] and x=900[m] (and x=1300 and 1900 [m]).

Lineplots for the different sized kites at hub height are shown in Figure 5.9. Zooming in on the velocity plots at the upstreampoints of the turbines (that determine the power production of the turbines) yields Figure 5.10 and Figure 5.11.

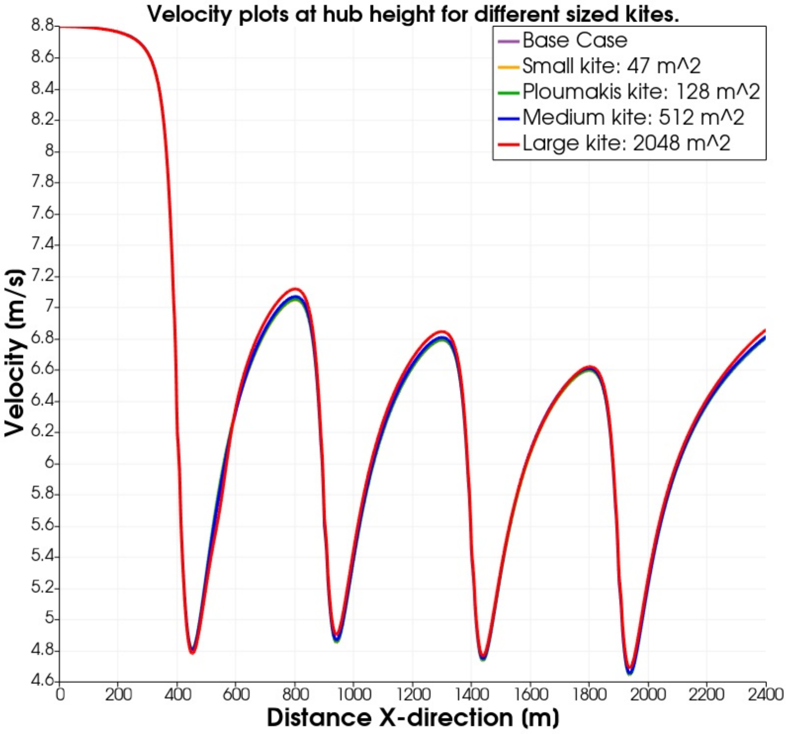

Figure 5.9: Line plots for the velocity in x-direction throughout the domain at hub height for different sized kites.

Figure 5.9 and Figure 5.10 show some expected results based on the findings found in Section 5.4.1. The kites sized 47 [m^2] and 128 [m^2] have minimal effect on the wake recovery at hub height. The medium sized kite of 512 [m^2] increases the velocity at hub height with 0.57 % whereas the largest kite of 2048 [m^2] increases the velocity in the wake with a little over 1 %. This is the first kite that shows a substantial increase in velocity, as it is generates a power increase of over 3% for the second wind turbine (according to basic wind turbine's power dependency on the cubed velocity). The conclusion drawn by Ploumakis that increased kite size results in higher wake recovery levels is validated.

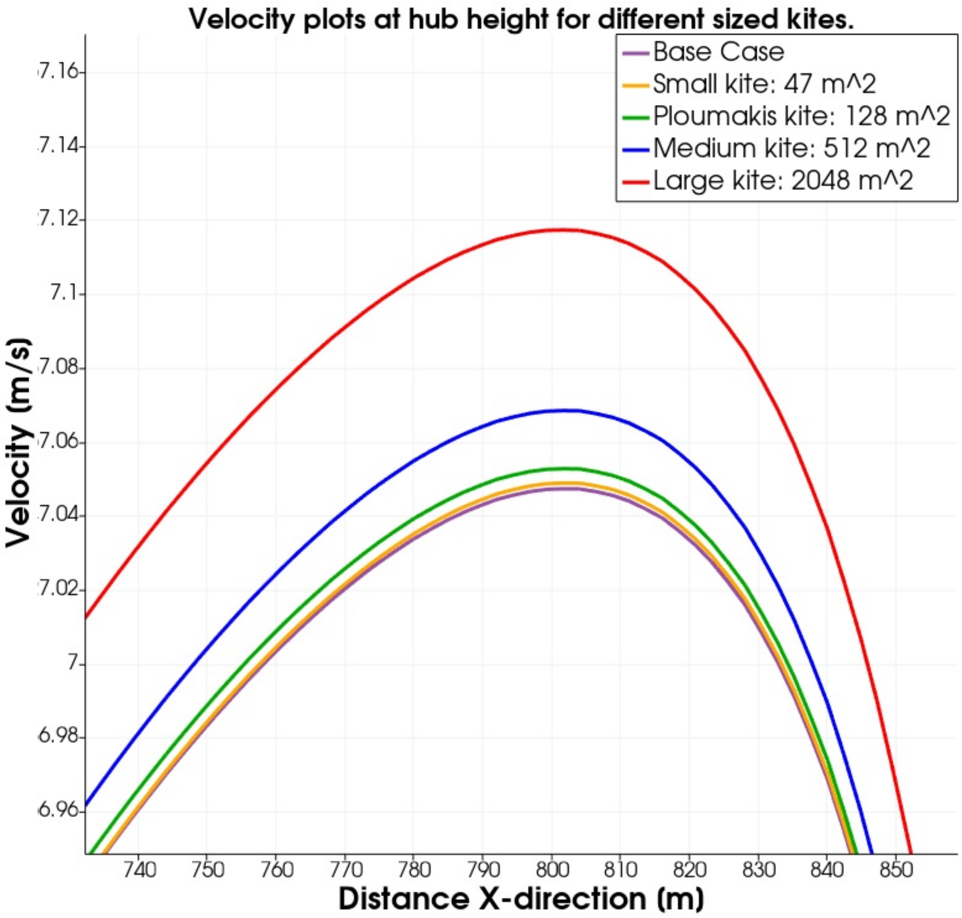

Figure 5.10: Zoomed in line plots at the upstreampoint of AD2 for the velocity in x-direction throughout the domain at hub height for different sized kites.

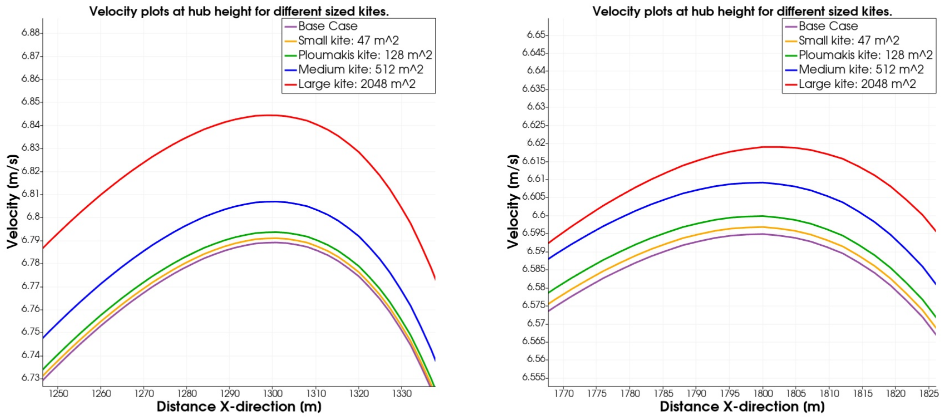

(a) (b)

Figure 5.11: Zoomed in line plots at the upstreampoint of AD3 (left) and AD4 (right) for the velocity in x-direction throughout the domain at hub height for different sized kites.

Interestingly, the effect of introducing a single kite between AD1 and AD2 also seems to affect the wake behind AD2 and AD3. However, this effect decreases with distance as the velocity increase in front of AD3 is a little over

0.05 [m/s] and in front of AD4 only 0.025 [m/s] for the largest kite, respectively representing a velocity increase of 0.7% and 0.36%.

Taking into consideration that the largest kite in these simulations is the only kite that introduces a considerable effect on the wake recovery of the wind flow, the kite sized 2048 [m^2] is used in cases B-D and F to study different parameters influencing the kite. Finally in case E, the different studied parameters are used in a kite farm simulation to find the most optimised wind and kite farm layout.

5.4.3 Parameter study case B results: Kite height

Next, the effects of kite height is studied using the kite sized 2048 [m^2]. A single kite is located in the centre (x=650 [m]) between AD1 and AD2 in the middle of the width of the domain. Kite heights are chosen at z = 120 [m] (the maximum height the ADs reach), z = 130 [m], z = 140 [m], z = 160 [m] and z = 180 [m]. With increasing height comes increased wind speed, and a larger force to be applied by the kites. Figure 5.12 provides a first result to the question whether the higher located kites will impact the wake more, or will be limited because of being located too high to impact the wake at all.

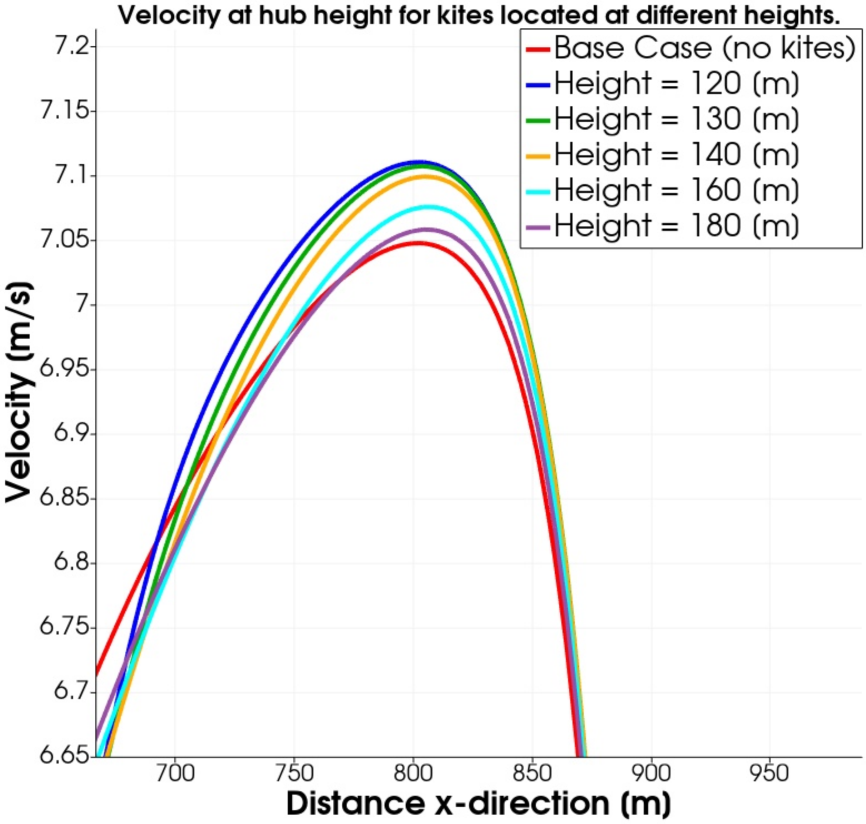

Figure 5.12: Zoomed in line plots at the upstreampoint of AD2 for the velocity in x-direction throughout the domain at hub height for kites located at different heights.

Noticeable is the slight increase in velocity when kites are located just above the sweeping height of the actuator discs (in comparison to the kite height of 140 [m] used in Case A). The kite at a height of 120 and 130 [m] seems to overlap closely, raising the expectation there may be an optimal height between 120 and 130 [m] height, though height effects are limited. In comparison to the base case (so without any kites), a little over 1% velocity increase is found (accumulating for a power increase of roughly 3%).

Another interesting effect is seen in the results of higher kite locations. It seems that the optimal kite height lies close to the top of the wind farm wake, and with increasing height, the effects drop gradually. The difference in effect between the kite located at a height of 140 [m] and 160 [m] is larger than that between z = 160 [m] and z = 180 [m] raising the expectation that with even higher height the base case scenario (no kites at all) will be reached again, providing a limit to kite height effects.

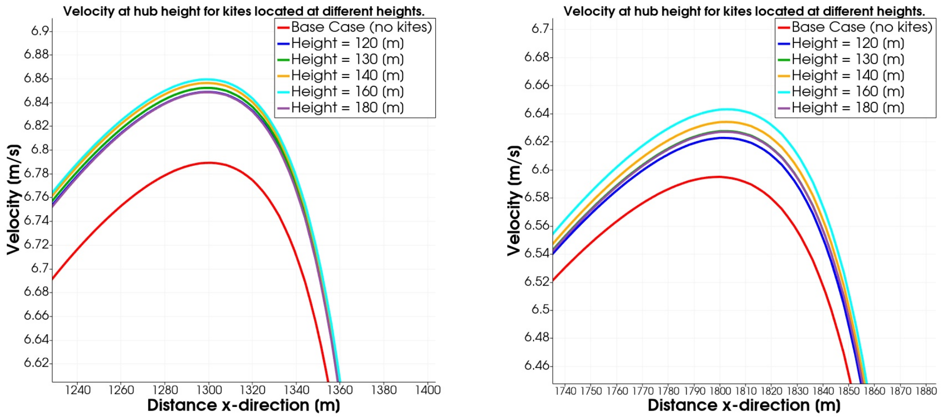

(a) (b)

Figure 5.13: Zoomed in line plots at the upstreampoint of AD3 (left) and AD4 (right) for the velocity in x-direction throughout the domain at hub height for kite located at different heights.

Figure 5.13 show the velocity plots at the upstream-points of AD3 and AD4. Immediately noticeable is that the higher kites have a larger effect on further downwind turbines (than closer located wind turbines). Especially the kite located at 160 [m] height has a large effect on the two downstream actuator discs, increasing the velocity with 1.5 % in front of AD3 and 0.73 % in front of AD4. The kites located at 120 [m] height has the smallest effect on AD3 and AD4 raising the conclusion that higher kites require larger distances to effect downstream turbines, whereas kites located close to the wind turbine wake have the largest effects on turbines located near (downstream). These findings are further studied and evaluated in Case F. In parameter study cases C, D and E, a kite height of 130 [m] is used because at this height, kites seem to perform well in impacting all 3 actuator discs.

5.4.4 Parameter study case C results: Downstream kite location

The kites sized 2048 [m^2] are introduced into the system at kite height z = 130 [m]. Different downstream location cases are simulated: x = 425 [m] (directly behind AD1), x = 540 [m], x = 650 [m] (centred between AD1 and 2), x = 760 [m] and x = 875 [m] (directly in front of AD2). Figure 5.14 shows the velocity in x-direction at hub height near the upstream point of AD2:

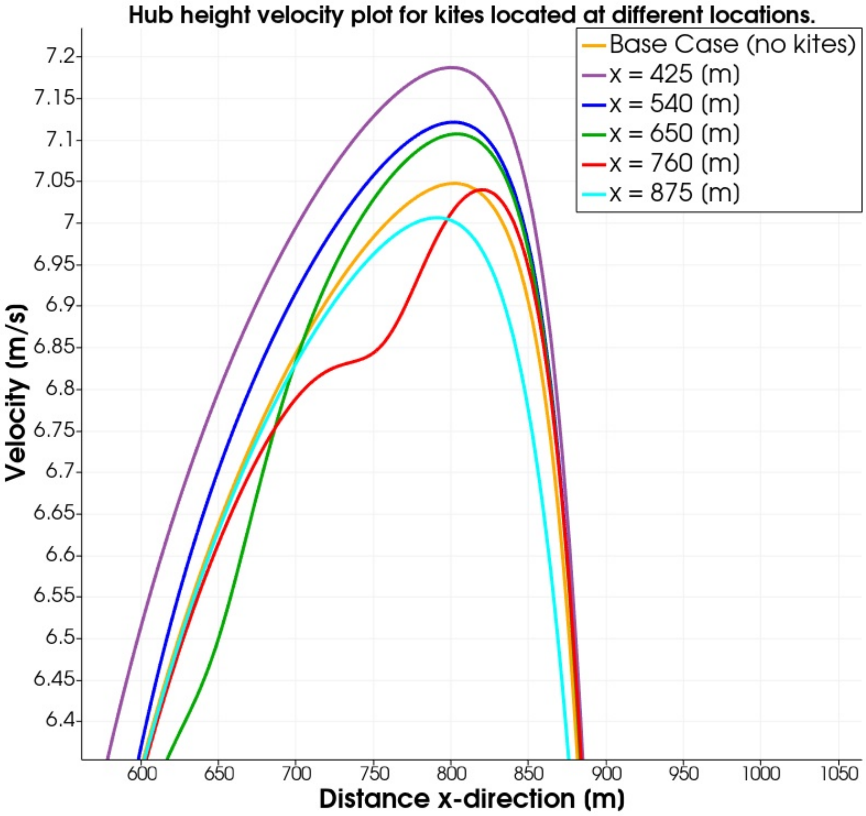

Figure 5.14: Zoomed in line plots at the upstream point of AD2 for the velocity in x-direction throughout the domain at hub height for kites located at different downstream locations.

Immediately some interesting results can be seen. As expected, the kite located close behind AD1 has the largest impact on the wake flow, re-energizing the velocity with almost 2% (power increase of roughly 6.1 %). The kites located at x = 425 and 540 [m] provide evidence that the increase in velocity is not linear with downstream location of the kite. The increase in wake velocity of locating a kite at x = 540 [m] is only slightly higher than the kite located in the middle between the two ADs. The difference in wake velocity recovery between locating a kite directly behind AD1 and at x = 540 [m] is almost 1 % which is much larger than the difference between the kite at x = 540 [m] and x = 650 [m].

Another interesting visualisation found in Figure 5.14 is the effect the kite located at x = 760 [m] has on the velocity profile. An initial velocity decrease is noticed before a steep velocity increase takes place. This is also noticeable for the kite located at x = 650 [m] where the velocity increase is much steeper after x = 650 [m]. A reason for this velocity profile might have to do with the pressure field introduced by the kites. The high pressure field forming under the kite slows down the velocity over the sweeping area of the kite's surface, after which it accelerates the velocity. The chord length of this kite equals 32 [m] so the kite's surface covers roughly a distance ranging between x = 730 [m] and x = 760 [m] with it's centre at x = 745 [m]. Noticing the velocity acceleration to start at x = 745 [m] further adds up to this conclusion.

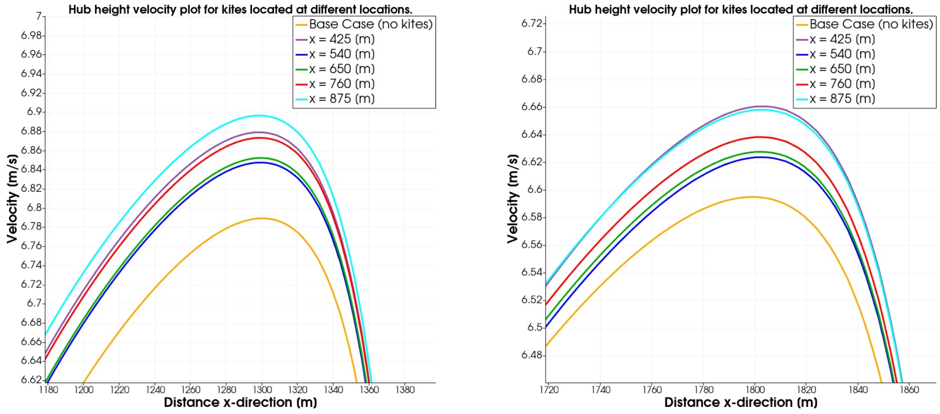

(a) (b)

Figure 5.15: Zoomed in line plots at the upstream point of AD3 (left) and AD4 (right) for the velocity in x-direction throughout the domain at hub height for kite located at different downstream locations.

Figure 5.15 shows the zoomed in velocity plots at the upstream points of AD3 and AD4. As expected, the kite located furthest downstream has the largest impact on AD3. However, interestingly, the kite located close behind AD1 still has a large impact as well, especially on AD4 where it equals the velocity increase of the kite located at 875 [m]. This is an unexpected result. Especially because the kites located at x = 540 [m] and x = 650 [m] perform worse than the kite located at x = 425 [m]. The kite furthest downstream increases the velocity in the wake with 1.6 % in front of AD3. In front of AD4, the furthest upstream and downstream kites increase the wake velocity with roughly 1% (in comparison to 0.36 % for a kite located at x = 650 [m] and 140 [m] height).

Figure 5.16 shows plots for the velocity versus height at the upstream point of AD2. Figure 5.17 shows zoomed in plots of these velocity versus height plots near hub height and in the top section of the actuator disc. A respectable 3 % wake velocity increase in the top section of the actuator disc is found using the kite located closest to AD1. An interesting result is that the kites located further downwind cause some sort of a blocking effect on the velocity, decreasing the wake velocity beneath that of the base case (so without kites). The kite located closest to the upstream point shows some interesting behavior by decreasing the velocity at hub height, while increasing the wind velocity in the wake at greater height. Again, this is probably caused by the pressure field generated underneath the kite's surface. In the upper section of the actuator disc, the results seem valid having the kites located closer to AD1 increase the velocity in the wake more than the kites located further downstream.

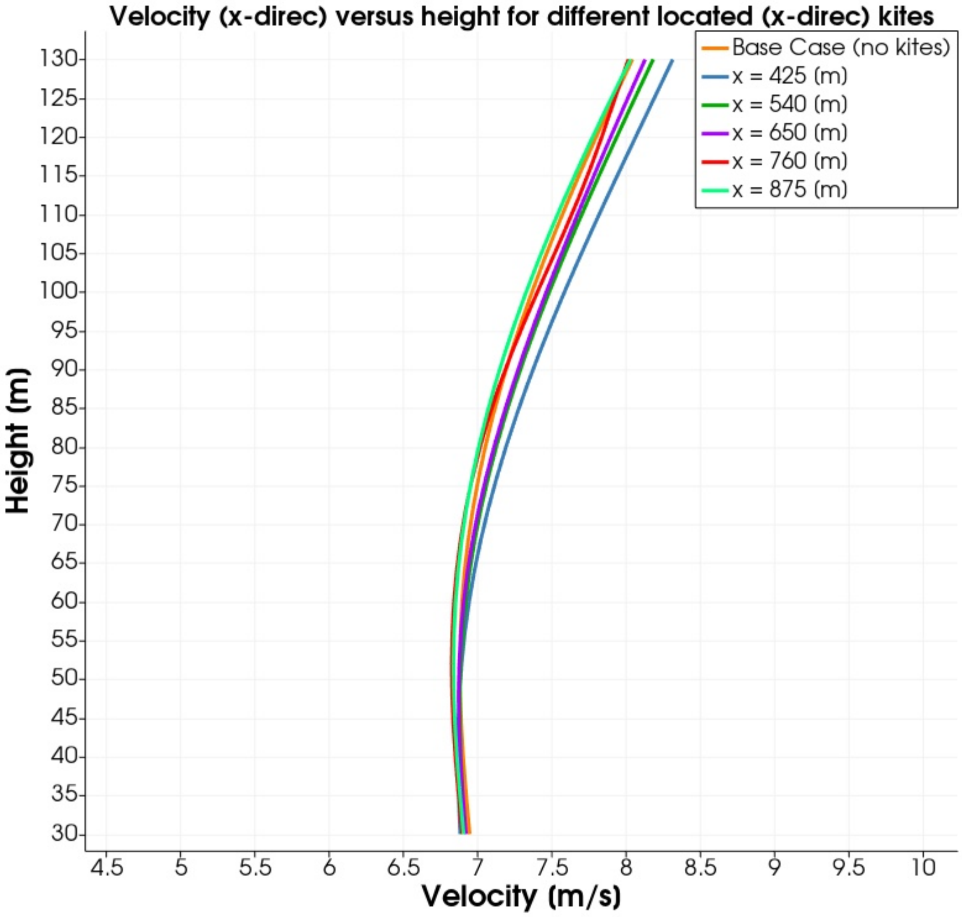

Figure 5.16: Velocity versus height at the upstream point of AD2 for different located kites (in downstream direction).

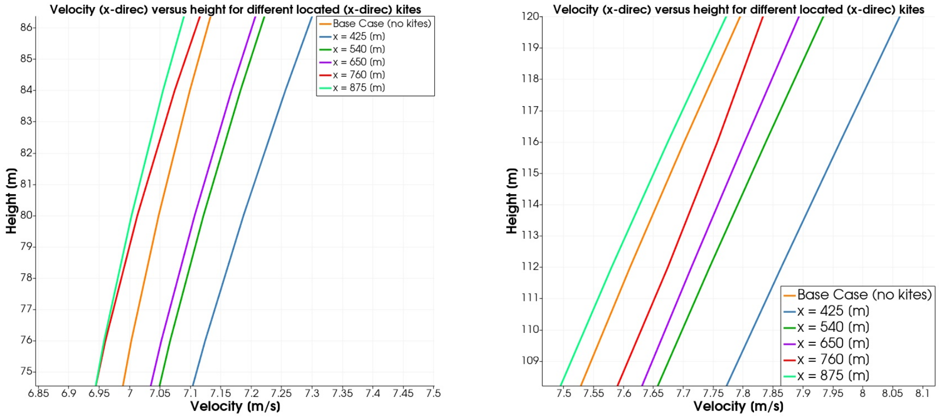

(a) (b)

Figure 5.17: Zoomed in velocity profiles versus height at the upstream point of AD2 for different located kites (in downstream direction).

5.4.5 Parameter study Case D results: Angle of attack variation

In case D the effect of angle of attack variation is studied by changing the initial angle of attack of the kites. A single kite is located at kite height z = 130 [m] in the middle between the first two turbines (at x = 650 [m]). Note that the incoming velocity alters this initial angle of attack to an effective angle of attack because of the so-called induced angle of attack explained in Section 2.2. The initial angle of attack can be regarded as a pitch angle.

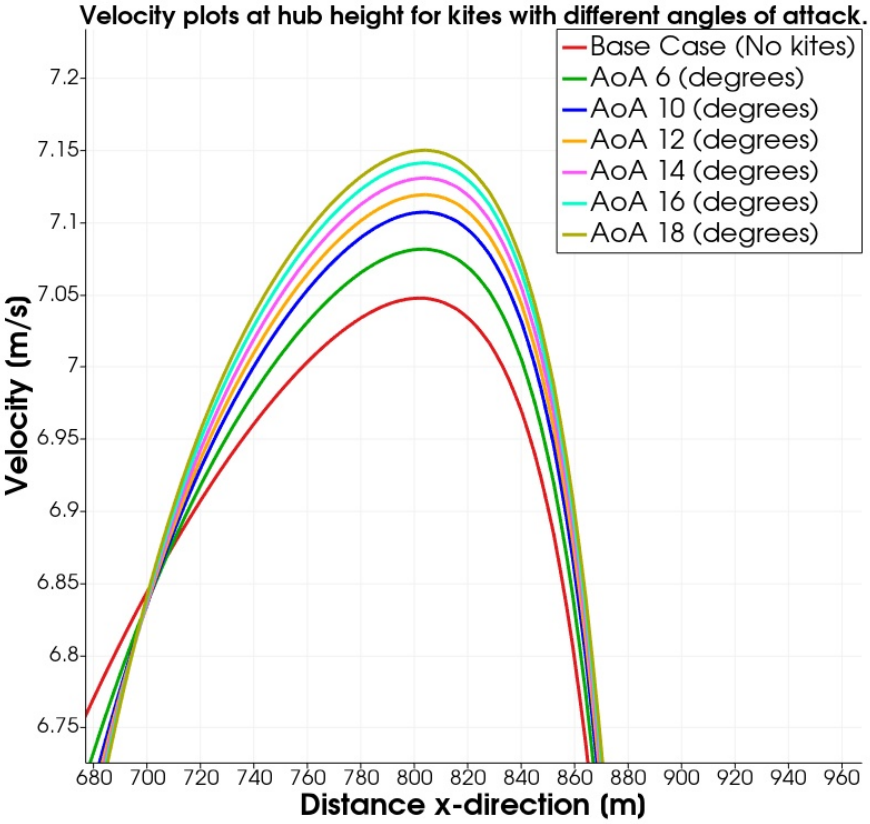

Figure 5.18: Zoomed in line plots at the upstream point of AD2 for the velocity in x-direction throughout the domain at hub height for kites with different initial angles of attack.

Figure 5.18 shows the velocity plots at the upstream point for the kites having a different AoA. Increasing angle of attack increases the lift force, and thus the vertical forcing that steers the wind from the unaffected ABL into the wake. This is visible in the figure because with increasing angle of attack comes increasing wake velocity recovery. Whereas an angle of attack of 6 degrees increases the wake velocity at hub height with 0.4 %, a kite with initial AoA of 18 degrees increases the velocity with 1.4 %. The velocity increase seems linear between AoAs of 10 - 18 degrees. However, velocity versus height plots at the upstream point may present additional results of the effect of AoA on wake velocity increase.

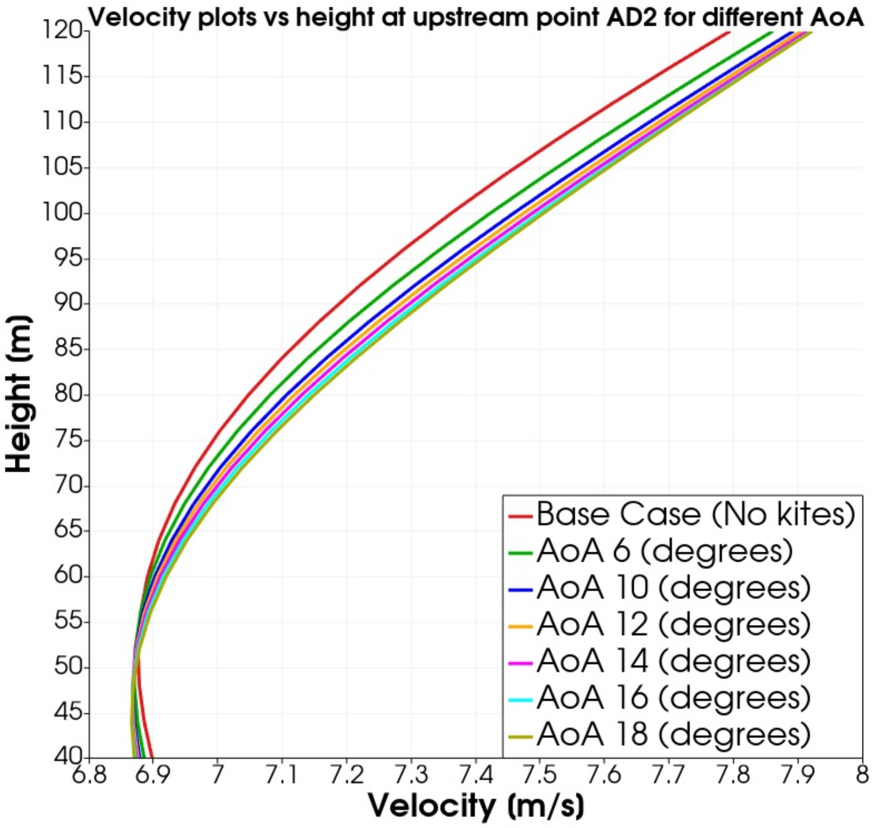

Figure 5.19: Velocity against height plots for kites with different angles of attack at x = 800 [m] (upstream point AD2)

Figure 5.19 plots the velocity versus height at the upstream point of AD2 for the kites with different AoA. Figure 5.20 shows snapshots of this profile at two interesting regions: around the hub height and at the top of the AD sweeping height. At hub height relatively similar findings can be seen as shown in Figure 5.18 where an increase in AoA results in an increase in velocity. However, the plots at the upper section of the AD show some interesting results. For the higher AoAs the velocity plots seems to converge. Especially the kite with an AoA of 18 degrees seems to overlap with the kite having an AoA of 16 degrees. This result is expected to have to do with the drag force induced by the kites. As explained above, for higher AoA the drag coefficient increases exponentially (whereas the lift coefficient increases linearly). For high values of AoA the drag force has become noticeably large and slows down the flow. In the upper region of the AD, especially because the kite is located just above the wake flow, this drag force may slow down the wake flow resulting in the lower velocity increases for higher AoAs.

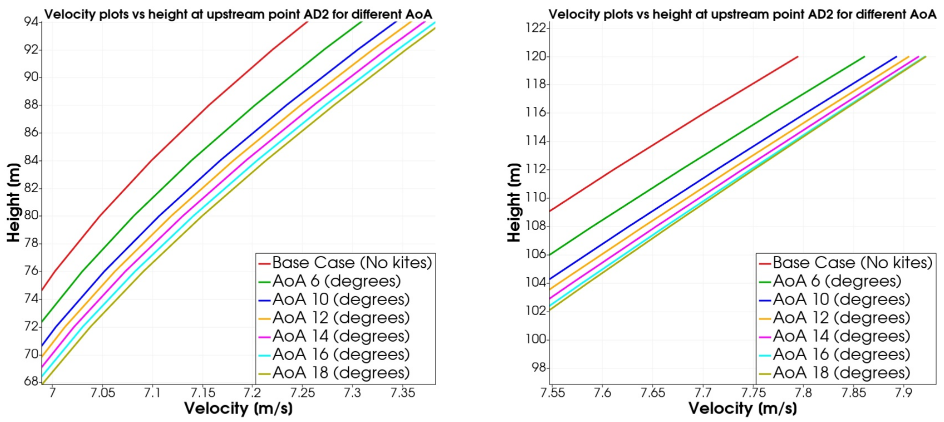

(a) (b)

Figure 5.20: Zoomed in velocity profiles versus height at the upstream point of AD2 for kites with different angles of attack.

5.4.6 Optimization problem Case E results: Kite farm optimization

Now that the parameter studies are performed and methods are found of increasing the wind farm wake velocity by altering the kite parameters, an optimised kite farm is simulated using three kites. This simulation takes into account all kite parameters that have been studied in cases A-D and uses the most impactful values found in the parameter studies. 3 kites of size 2048 [m^2] are introduced directly behind the ADs (x = 425, 925 and 1325 [m]) at a kite flight height of 130 [m]. Initial angle of attack of all three kites is set at 18 [degrees].

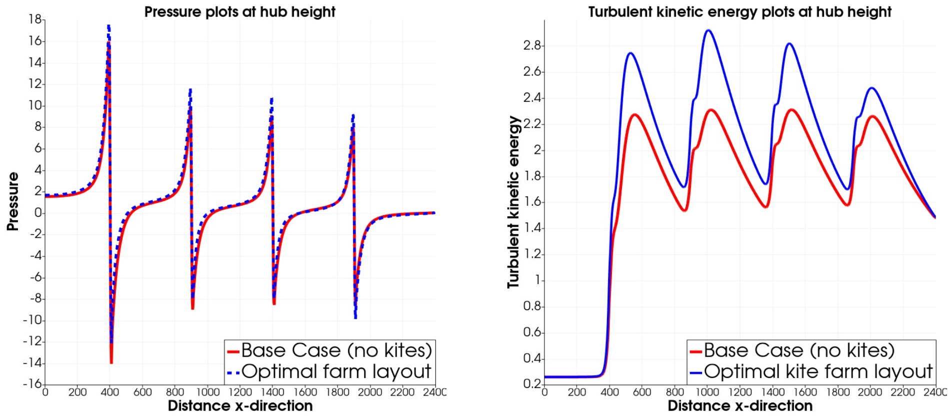

(a) (b)

Figure 5.21: Pressure (left) and turbulent kinetic energy (right) plots at hub height (80 m) comparing the optimal kite farm layout with the base case.

Figure 5.21 show the plots for the pressure (divided by density) and turbulent kinetic energy at hub height for both the base case (without kites) and the most optimal kite farm layout. It can be seen that the pressure rises throughout the domain as turbine 1 experiences a similar sized pressure drop, but reaches a higher positive pressure and a higher negative pressure.

For turbines 2 and 3 the total pressure drop increases: the positive pressure increases in comparison to the base cases and the negative pressure reaches the base case pressure. However especially AD4 sees a large pressure drop increase, thus generating much more power than in the base case. Both the positive and negative pressure are much larger (up to 25%), experiencing a much higher power generation.

The kites introduce considerable more turbulence into the wake. Up to a 20 % higher turbulent kinetic energy is reached behind AD1, whereas AD2 experiences an increase of almost 30 %. Interestingly, the turbulence reaches a maximum increase for AD2 and decreases (in comparison to the increase of AD2) for further downwind turbines. It is possible that for an even larger wind farm (and with the addition of kites) a limit on increased turbulence into the wake is reached. It could also be an effect from the 3 kites being located at similar heights and experiencing the wake generated by upwind kites. The increased pressure drops and turbulent kinetic energy are expected to increase the velocity in the wake. Plots of the wake velocity versus height at 4 downstream points are shown in Figure 5.22 and Figure 5.23.

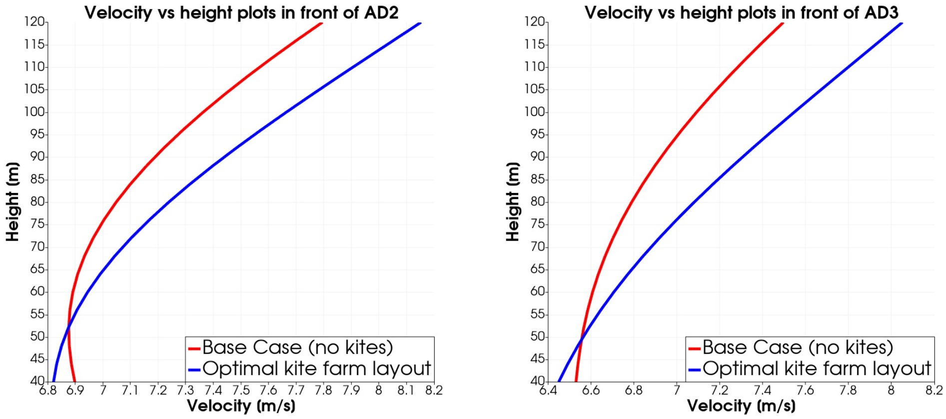

(a) (b)

Figure 5.22: Velocity plots vs height in front of AD2 (left) and AD3 (right).

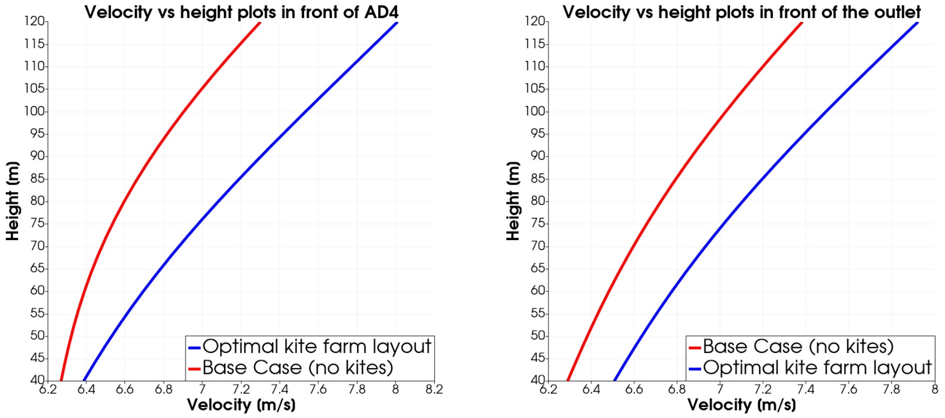

(a) (b)

Figure 5.23: Velocity plots vs height in front of AD4 (left) and the outlet of the domain (right).

The plots shown above are located at x = 800 [m] (upstream point AD2), x = 1300 [m] (upstream point AD3), x = 1800 [m] (upstream point AD4) and x = 2350 (50 [m] in front of the outlet of the domain). Note that no kite is located behind AD4 so it is to be expected that at x = 2350 [m] the wake velocity increase has decreased.

A considerable velocity increase is seen at the upstream points of the different ADs. In comparison to the base case, the velocity at the upstream point of AD2 increases with 2.7 %, at the upstream point of AD3 the wake velocity is increased with 4.7 % and at the upstream point of AD4 with 7.4 % which is a considerable amount. With the increasing wake velocity for downwind turbines, an immediate question for future research rises whether in a larger wind farm even higher wake velocity recovery values can be reached. Interestingly, for ADs 2 and 3, the lower section of the actuator disc shows a lower velocity compared to the Base Case. This is expected to result from the downwash velocities generated by the kites. It can be seen that the optimal kite farm plots show increased velocity in the wake because the base case velocity plots are pushed down by the downwash velocity generated by the kites. An additional effect shows that the largest velocity deficit (normally found at hub height) may be pushed down as well because of the downwash velocity. That may be the reason why for ADs 2 and 3 the curve of the Base Case intersects with the optimal kite farm layout. For further downwind turbines already a lot of turbulence is introduced into the system and the wake flow has been pushed down several times (by the kite's downwash velocity). This probably explains why the curves don't intersect from AD4 onwards. As expected, without a kite behind AD4, the wake velocity recovery decreases fast, with only a velocity increase at hub height of 5.9% (in comparison to 7.4% in front of AD4) at the outlet of the domain.

Figure 5.24 shows a snapshot of the x-z plane and the downwash wake generated by the kites. In comparison to just behind AD4 where no kite is located, the immediate effect of the kites can clearly be seen in the figure. Even though the pressure regions formed by the ADs, the additional effect of the kites result in a large downwash wake. A vertical velocity of up to -1.7 [m/s] is reached behind AD1, AD2 and AD3. Interestingly, instead of a single small region of downwash, an entire downwash wake can be seen. This means that upstream kites are likely affecting downwind kites located at similar heights.

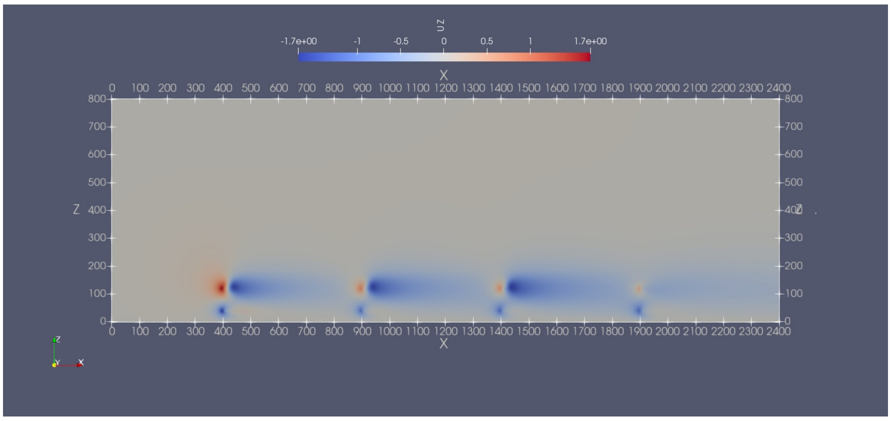

Figure 5.24: Snapshot of x-z plane showing the vertical velocity throughout the domain. The kites, located directly behind the turbines, show a downwash of over 1.5 [m/s]

Table 5.3 presents the final results for the optimized kite farm layout. An efficiency increase of 5.4 % results from the comparison between this optimized kite farm layout and the Base Case (using no kites). The largest power increase is measured at AD4 where power production has increased with almost 24 %.

Kite Farm:	AD 1	AD 2	AD 3	AD 4
Upstream point velocity [m/s]	8,79	7,24	7,11	7,08
Thrust force [kN]	211	143	138	137
Power output [MW]	1,86	1,04	0,984	0,972
Efficiency wind farm [%]				**65,3**
Base Case:	AD 1	AD 2	AD 3	AD 4
Power output [MW]	1,86	0,958	0,856	0,785
Efficiency wind farm [%]				**59,9**

Table 5.3: Optimal kite farm configuration vs Base Case (without kites). An increase of 5.4 % efficiency is reached.

5.4.7 Parameter study Case F: Wind velocity variation

2 simulations are performed for a similar kite system (containing 3 kites) in a 4-turbine wind farm. Together with the wind farm simulations performed in Section 4.2.4, all 4 simulations are run as described in Section 5.3.7. Velocity profiles at hub height for the four different simulations are shown below:

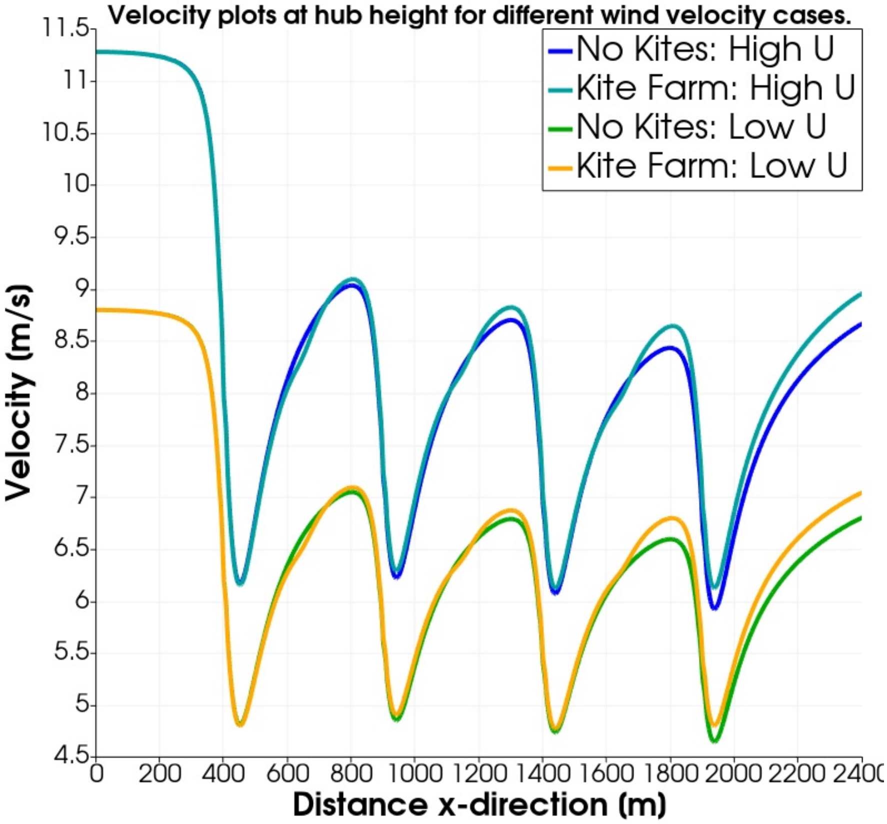

Figure 5.25: Velocity plots at hub height for a wind farm with/without kites at a reference velocity of 7.8 [m/s] (at reference height of 12.5 [m]) and a wind farm with/without kites at a reference velocity of 10 [m/s] (at similar reference height).

The plots show the results that are expected: the simulations of a wind farm (with or without kites) at higher wind velocity show almost exactly the same results as the simulations of a wind farm at a lower wind velocity that is transformed upwards. For AD4, using kites increase the wake velocity with 3.09 % for lower velocity, whereas the wake velocity increases with 2.98 % for higher velocity. These velocity increases are almost identical so using different wind velocities seems to effect the wake velocity increase minimally.

6 DISCUSSION

The introduction of kites in wind farms for wake recovery purposes shows promising results in increasing the wind farm efficiency. Exploiting all optimized kite parameters an efficiency increase of 5.4 % is found. However, these results are based on a list of assumptions that need to be addressed before drawing any conclusions. The methodology and results of modelling the ABL, the wind farms and the kites will be discussed in the following three sections.

6.1 ATMOSPHERIC BOUNDARY LAYER

The first step in this Thesis is the ABL modelling using the atmBoundaryLayer class. Results correspond well with literature for the log-law profiles for the velocity and dissipation of turbulent kinetic energy. However, the turbulent kinetic energy profiles at the inlet and outlet of the system are considerably different. Zhang [2009] and Segersson [2017] obtained similar results for ABL simulations in an empty domain. Zhang [2009] concluded that a constant vertical profile for the turbulent kinetic energy could only be reached when applying a shear stress at the top of the domain. Different user defined wall functions were introduced into the boundary conditions to sustain the wind flow better. However without the introduction of shear stress at the top of the domain, this effect can only be sustained with complex modifications to the viscous model. Quoting Segersson [2017]: "Hargreaves and Wright (1993) shows similar deviations using standard wall-functions in Fluent and CFX. However, given that the implementation in OpenFOAM is based on their findings, it is surprising that the inlet profiles for k are not better preserved in OpenFOAM. More investigations are required to identify the exact reason for this."

Schalau et al. [2021] noticed this problem as well and recorded rapidly changing turbulence profiles throughout the domain when using conventional RANS turbulence models. Schalau developed a system of boundary conditions that proved to be more consistent with reaching a horizontally homogenous boundary layer flow using the RANS turbulence model. This was done by using power laws instead of logarithmic profiles for the velocity and turbulence boundary conditions. Different methods have been found to achieve this horizontally homogenous boundary layer flow through changing the constants in the k-ϵ equations (for example: Alinot and Masson [2005] or Yang et al. [2008]). Even though the constants in the k-ϵ were studied, eventually both studies concluded an additional source term had to be added to the transport equations for the turbulence kinetic energy, and the dissipation of turbulence kinetic energy.

Interestingly enough, the turbulence kinetic energy does not seem to affect the velocity and dissipation profiles. Additionally, the introduction of obstacles (in this work actuator discs) seems to decrease the effect of not reaching a horizontally homogenous boundary flow. The effects the ADs have on the turbulence kinetic energy follows literature well. This probably results from the turbulence kinetic energy being limited by the actuator disc's influence to develop into a non-homogenous boundary flow throughout the domain. However, the effect of a non-homogenous boundary flow should be kept in mind throughout this study as the turbulence kinetic energy at the inlet is roughly 2.5 percent higher than at the outlet. This may contribute to the turbulence kinetic energy decreasing throughout the domain, which is an effect seen in all wind farm and kite farm layout simulations. This decrease in turbulence kinetic energy may result in less turbulence induced by the kites so a lower level of wake velocity recovery. Future research should try to use one of the mentioned techniques above to account for a homogeneous boundary flow throughout the domain, or mention this limitation clearly.

6.2 WIND FARM SIMULATIONS

Part two of this study focuses on the introduction of wind turbines in the empty domain. This is done through the actuator disc model. Initial wind farm simulation results seem valid: turbulence increases behind the ADs, the velocity deficit behind and pressure drop over AD1 is largest (when 4 equally ADs are studied) and the RANS simulations overestimates wake recovery compared to literature LES simulations (see Figure 4.27). Validation of the wind farm results also shows promising results: compared to different AD and turbulence models, the normalised power (relative to AD1) corresponds well to the RANS simulations performed in the work of Barthelmie et al. [2009]. Two RANS simulations were performed by Barthelmie et al. [2009]. The normalised power values of this Thesis falls between the values found by Barthelmie, providing a good base for the introduction of kites into the system.

However, one of the main limitations of this work is actually this actuator disc (AD) model (although also used in lots of other literature works). This AD model focuses on a single upstream point to measure the thrust force (and power generation) for the entire actuator disc. This upstream point is located at hub height at the upwind location where the velocity has reenergized the most (which turned out to be 100 [m] in front of the ADs). The limitation of this AD model comes twofold:

1. At hub height the ADs experience some of the largest velocity deficits in comparison to the entire sweeping area of the AD. This means that some of the lowest possible thrust force and power production is cal-

culated for downwind turbines adding to the overestimation of wake effects resulting from RANS turbulence models.

2. When studying wake velocity re-energizing from the unaffected boundary layer above the wake, the upper part of the ADs experiences the largest velocity recovery. Using the velocity at hub height thus underestimates the wake velocity recovery.

Overestimation of wake effects and underestimation of wake recovery are thus caused by using this AD model. G. A. M. Van Kuik [2020] addresses the limitations of the earliest version of the AD momentum theory (used in this thesis) and describes the more recent extension to this theory. Quoting van Kuik: "This theory gives the performance data like the power coefficient and average velocity at the disc." If an average velocity at the disc was used (see for example Jeromin et al. [2014] who implemented this theory into OpenFOAM), a higher velocity would be used to calculate the thrust force and power generated by the downwind turbines. Taking a look at the velocity plots at the upstream point of AD2 (see Figure 4.23), an estimated average of the velocity over the entire disc height yields an increase of 3 % (compared to the velocity used). This yields roughly an increase in power production of 10 % increasing the efficiency of the wind farm significantly.

Additionally, the ADs used in this Thesis are non-rotating. Wu [2012] explored the differences between using rotating and non-rotating actuator discs. He concluded: "the ADM-R model yields improved predictions compared with the ADM-NR in the wakes of all the wind turbines, where including turbine-induced flow rotation and accounting for the non-uniformity of the turbine-induced forces in the ADM-R appear to be important." Note that ADM-R refers to the rotating actuator disc model and NR refers to non-rotating AD model. Using a rotating AD increases the wake recovery (caused by the swirling of the disc introducing more turbulence into the wake).

It is beyond the scope of this study to explore these more complex actuator disc models. With the same AD model used throughout this study, the same overprediction of the wake losses and underprediction of the wake recovery can be expected throughout the results. Even though future research should study the effects of kites on these more realistic AD models, the limitations of the AD method are considered throughout the entire work, thus limiting the effects on the conclusions drawn.

6.3 KITE SIMULATIONS

Referencing back to the introduction (Section 1.6): in the final phase of this study various kite parameters are studied and the largest efficiency increase of the wind farm is assessed. In this study a wide variety of kite parameters are studied: kite sizes, kite height, kite downwind location, angle of attack and wind velocity. The simulations studying kite size, kite height and wind velocity gave results that were expected:

1. With increasing kite size larger downwash velocity and higher re-energizing levels are realised.
2. A kite should be located close above the wake, as for higher located kites the effects on the wake velocity is minimal.
3. Increasing the wind velocity in the domain has little effect on the effects kites have on wind farm efficiency increase.

Two interesting results are found in the parameter studies of the angle of attack and downwind location of the kites.

1. Increasing the angle of attack (AoA) expectedly results in increased drag and lift forces. This lift force is accountable for the downwash velocity so is expected to increase the velocity in the wake. However, in the upper section of the AD the drag force limits the velocity increase of the wake. This probably results from the non-linear relationship between AoA and drag coefficient (whereas AoA and lift coefficient have a linear relationship up until the critical AoA).
2. A large velocity increase at the upstream points of the ADs are realised through locating the kites close behind the upstream ADs. A velocity increase of almost 2% is measured compared to the base case (using no kites).

Taking all optimal kite parameters and introducing a kite farm (of 3 downwind located kites) yields an efficiency increase of 5.4 %. This analysis thus supports the theory that kites located between turbines are able to affect the spatial distribution of the mean velocity deficit. However, data found in the validation case suggests that the effect of kites on the wake flow is multiple factors (up to 16) smaller than what is found in the work by Ploumakis [2015] (by comparing the wake velocity increase of Ploumakis' work and this work). Multiple questionable methodology decisions in the work of Ploumakis may account for this much lower effect of kites on the wake flow. However, due to the lack of research done on the topic of kite use in wind farms, quantitative results are difficult to validate and the exact reasons for the difference in results between this study and Ploumakis work are not found. More research is required to confirm the 5.4 % wind farm efficiency increase. Qualitative conclusions from the parameter studies, however, can be drawn and give insight in what kite parameters should be selected or further optimized in future work.

For the difference in results between Ploumakis [2015] and this work, multiple factors can be accountable. Most importantly, the pressure drop considered in Ploumakis' work is calculated from simulations performed under different conditions than those that are used in his Thesis. Simulations performed under a different aspect ratio, Reynolds number and kite model provide the base for the work of Ploumakis. Additionally, a constant pressure drop is introduced at the kite's locations, which does not account for any effects of the wakes generated by both the turbines and the kites. In this work, already a considerable chunk of the velocity has dropped in front of the kite because of the turbine wakes. Additionally, this study introduces the effect of downwash wakes, which affect downwind kites with an additional velocity loss.

The quantitative efficiency increase of 5.4 % is realised using a kite of 2048 [m^2]. This provides a practical difficulty because the current kite energy sector has not used kites larger than 500 [m^2]. In comparison: the largest kite that has ever been created (for celebratory purposes) and flown is 2673 m^2 (Katyayan [2020]). Flying a kite this size between turbines is thus (yet) non-practical. With a 5.4 % however, the question arises what effect more practical kites have on the wind flow. One final simulation is performed using the 16x32 kites (and the optimal kite farm layout) and an efficiency value of 62.2 % is recorded. In comparison, the Base Case (without kites) has an efficiency of 59.9 %. This concludes that the parameter studies in this Thesis have achieved a wind farm efficiency increase of 2.3 % using more realistic kites.

Comparing these results with the direct electricity generating kites used in the airborne wind energy sector, the total power gain is lower for kites used to recover the wake in wind farms. An increase of 0.17 [MW] power production is found using the 16x32 kites. For large sized direct electricity generating kites of 400 [m^2], a power density value of up to 3.7 [KW/m^2] has been reported, yielding a power generation of 1.48 [MW] (Ploumakis [2015]). Thus, comparing the two kite uses, direct electricity generating kites yield higher power levels than using kites to recover wakes between wind farms[1]. With these findings, a question arises whether a system could exist where hybrid kites could be used, capable of direct generation of electricity as well as assisting in wind farm wake recovery.

This Thesis has a theoretical nature and the practical aspects of introducing kites behind wind turbines is beyond the scope of this study. Additionally, this kite model has been limited to a static kite. In the airborne wind energy sector, much larger kite forces are reached when kites make crosswind maneuvers. The issue with crosswind flying kites, however, is that the force generated by the kite changes in direction throughout the crosswind maneuvers. This results in the kite force also opposing the generation of a downwash velocity into the wind farm wake. Future research could be done towards studying the kite velocity throughout these crosswind maneuvers and work out if the netto result is more advantageous over the effects of static kites.

---

[1] Note however that direct electricity generating kites fly at greater heights than the kites used for wake recovery purposes in wind farms. In a likely future where turbines will continue to increase in size, the effects of kites flying at greater heights may vary the wake recovery levels.

7 CONCLUSION & RECOMMENDATIONS

Now we can confidently say that kites located between turbines are able to re-energize a considerable amount of the wake velocity deficit. The introduction of kites, using the actuator line model, in a four turbine wind farm yields a wind farm efficiency increase of up to 2.3 %. This result is achieved through extensive parameter studies of kites focusing on: kite sizes, kite height, kite downwind locations and initial angle of attack. In the future, when even larger kites can practically be introduced in wind farms, wind farm efficiency may increase with efficiency values of over 5 %.

Prior to the introduction of kites, simulations of the atmospheric boundary layer and wind turbines give results corresponding well with literature. The Reynolds-averaged Navier-Stokes turbulence model with the k-ϵ closure equations give accurate representations for the velocity and dissipation of turbulence kinetic energy for the atmospheric boundary layer throughout the domain. The vertical profile of the turbulence kinetic energy throughout the domain, however, fails to remain constant, an issue experienced often in literature. Additional source terms need to be introduced in the transport equations for the turbulence kinetic energy to gain the desired homogeneous boundary flow. The normalised power deficits of downstream ADs corresponds well with wind farm simulations under similar conditions performed in literature. The wind farm simulations of this study support the theory that the RANS turbulence model tends to overestimate the velocity deficit generated by the turbines.

Based on the parameter studies performed in this work, it can be concluded that kite size, kite height, downwind kite location and angle of attack are important parameters to consider when introducing kites into a wind farm. With increasing kite size and angle of attack (up to the critical angle of attack), faster wake velocity re-energising levels are found. With the effects of kites clearest visible in the upper section of the AD, an interesting finding is that increasing the angle of attack however tends to limit the wake recovery at the top of the ADs. This may be caused by the exponentially increasing (with angle of attack) drag force which opposes the wake velocity recovery. The kite parameter affecting wake recovery the most substantially is the downstream location of the kite. Locating the kites directly behind an upstream turbine (x + 25 [m]) yields a much larger wake velocity recovery than for kite locations further behind the upwind turbine. The optimal kite height is located just above the wake generated by the wind turbines. Locating the kite at greater heights results in decreased effects on the wake velocity recovery. These findings support the theory that kites located between turbines are able to affect the spatial distribution of the mean velocity deficit which was introduced in literature.

7.1 RECOMMENDATIONS

Suggestions for future work are listed next:

ABL and wind farm simulations

1. To achieve an improved homogeneous boundary flow throughout the domain, a configuration to the transport equation of the turbulence kinetic energy should be obtained (see for example Yang et al. [2008] and Alinot and Masson [2005]). Introducing an additional source term into the transport equation will yield constant vertical plots of the turbulence kinetic energy throughout the domain, limiting the effects of a non-homogenous turbulence kinetic energy on the ABL.

2. An improved AD model for the turbines is said to decrease the overestimation of the velocity deficit when using the RANS turbulence model. Additionally, developing an AD model capable of calculating velocity and force distributions over the entire disc's surface will yield improved quantitative insights into the effects kites have on the wake flow. See for example the work of Behrouzifar and Darbandi [2019] for a starting point of this improved AD model.

Kite simulations

1. Two studies, yielding considerably different results, have been performed on the introduction of kites into wind farms to develop the wake flow. Simulations of such wind farms containing kites using different turbulence models and different representations of kites should be performed so that quantitative conclusions may be drawn. Preferably, the effects of a kite on a small wind farm should be investigated in a wind tunnel. The turbines and kites of the validation case should be scaled down to wind tunnel level so that immediate validation with this work and the work of Ploumakis [2015] may take place.

2. The introduction of kites into the unaffected boundary layer in this study introduced the concept of 'a downwash wake'. This region of downwash should be further studied by for example quantifying its effect on downwind kites. Additionally, downwind kites could be introduced at different heights so that effects of this downwash region is limited on the downwind kites.

3. This study introduces static kites into wind farms. Future research could be done towards studying the kite velocity and force throughout crosswind kite maneuvers. A conclusion should be drawn if crosswind maneuvering kites outperform static kites.

4. A practical and economic study should be performed on the introduction of kites into a wind farm. The question should be answered if flying kites can be realised in any cost-effective manner and quantitative insights should be presented comparing the use of kites in wind farms to the use of direct-electricity generating kites.

A ABL APPENDIX

As described in Section 4.1.4, a few iterations are required before convergence takes place throughout the whole domain. To illustrate the effects of iterations required on convergence (and divergence), figures Figure A.1 - Figure A.5 show the effects of the iteration number on the correct vertical wind profile. The inlet always follows the desired log-law relationship (because of the boundary condition on the inlet), however throughout the domain, at low iteration number, boundary conditions clash and enforce convergence to not take place yet. After 100 iterations, the vertical wind profile in the centre starts to align closer to the theoretical log-law wind relation, and after 200 iterations it fully follows the theoretical log-law wind relation. The vertical wind profile near the outlet needs more iterations to follow the theoretical log-law relation. After 300 iterations it starts to follow the theoretical log-law velocity relation closely, and when convergence has fully taken place, the outlet vertical wind profile aligns fully with the theoretical log-law velocity profile. This concludes with the statement presented in Section 4.1.4 that the final iteration should always be studied.

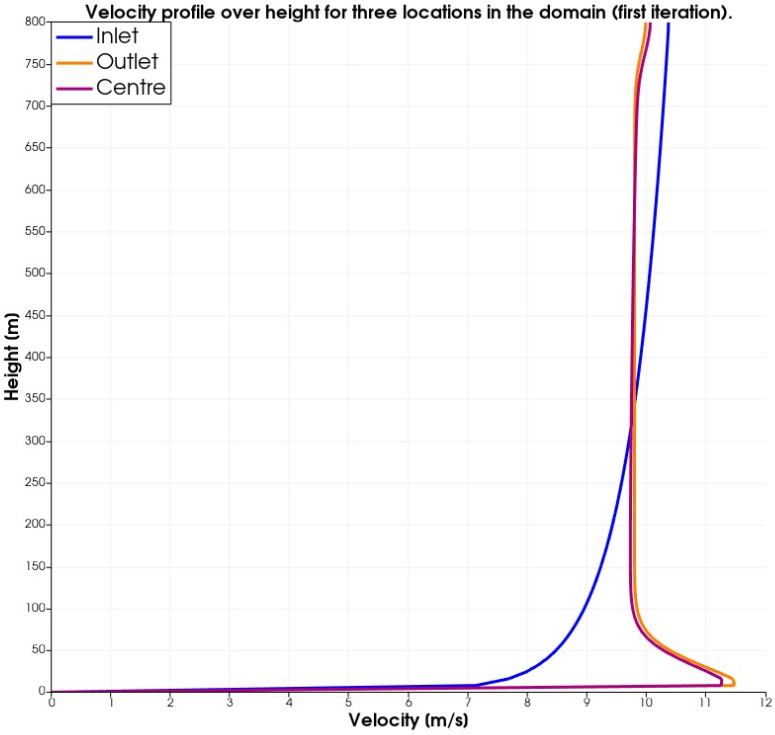

Figure A.1: Velocity profile over height at timestep 0 at x=10, 1200 and 2350 meters.

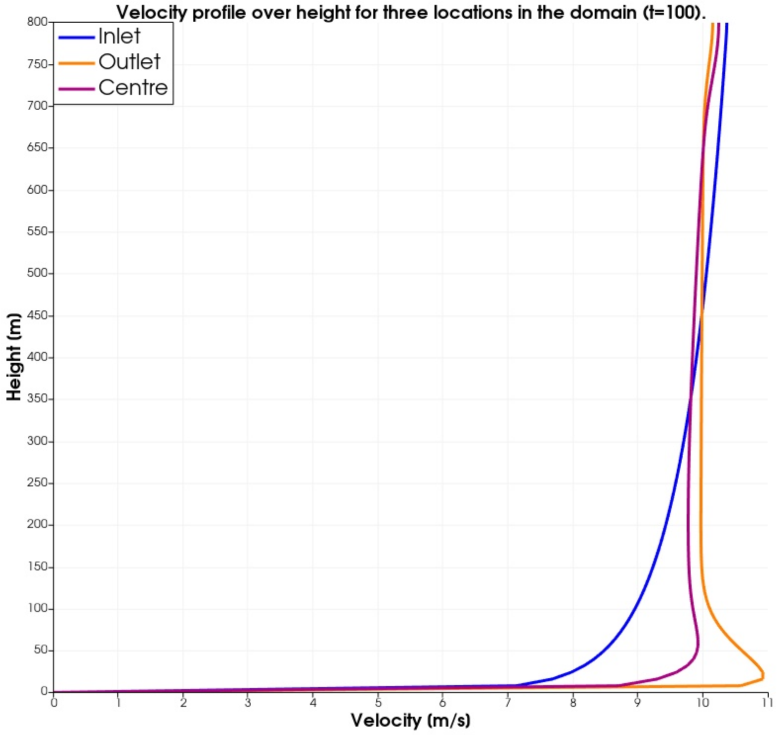

Figure A.2: Velocity profile over height at t=100 [s] at x=10, 1200 and 2350 meters.

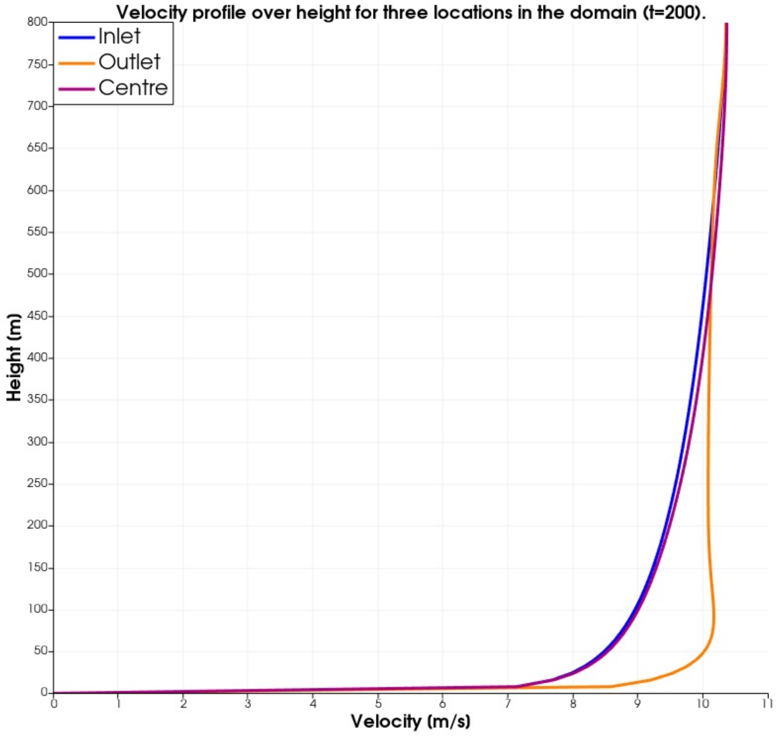

Figure A.3: Velocity profile over height at t=200 [s] at x=10, 1200 and 2350 meters.

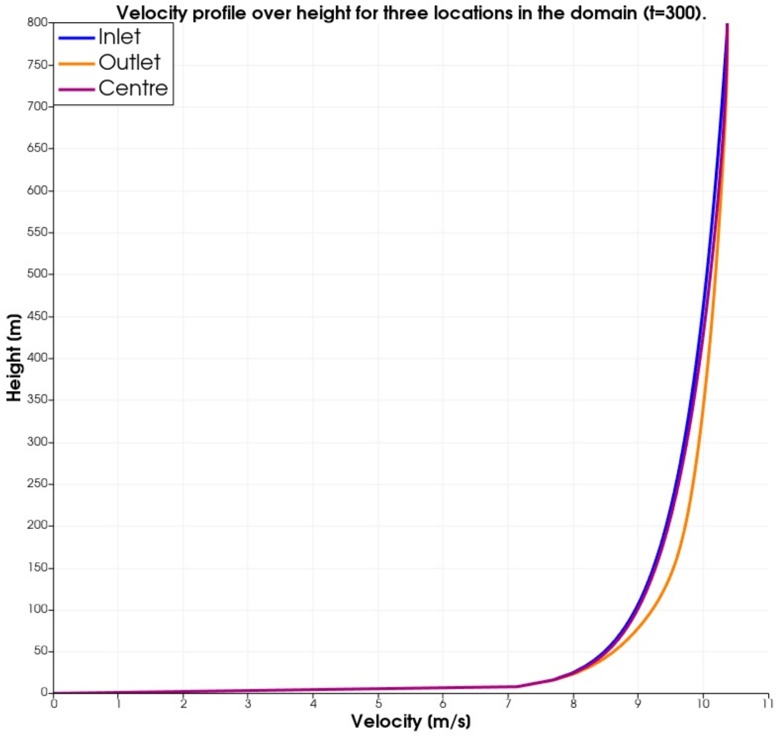

Figure A.4: Velocity profile over height at t=300 [s] at x=10, 1200 and 2350 meters.

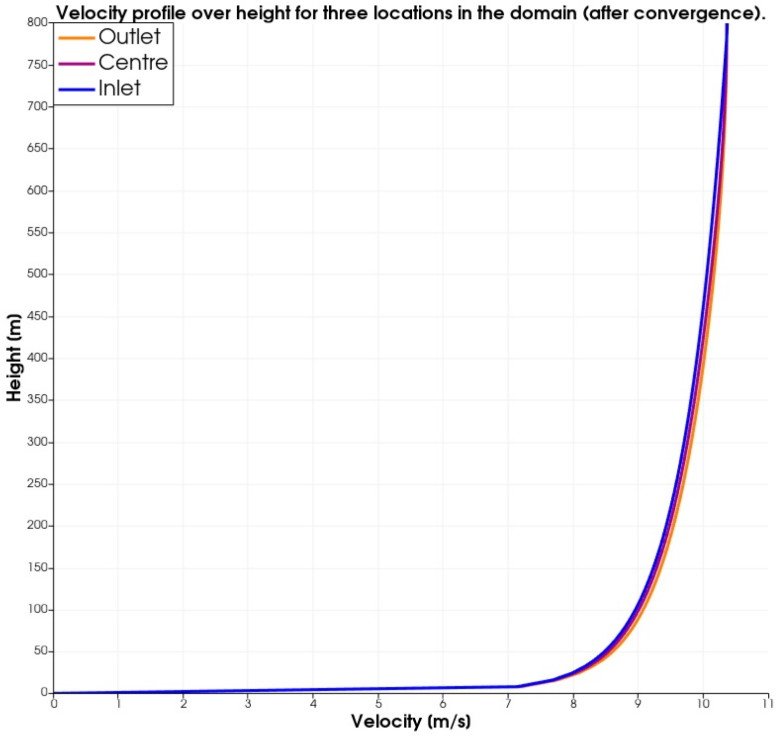

Figure A.5: Velocity profile over height at the final iteration at x=10, 1200 and 2350 meters.

B WIND FARM SIMULATIONS APPENDIX

Figure B.1, Figure B.1 and Figure B.3 show the pressure, turbulent kinetic energy and velocity plot for simulations of the wind farm at a higher velocity at reference height. The results show exactly what is expected: higher pressure drops, higher turbulent kinetic energy maxima, and similar velocity deficits (percentages). This is a direct result of the increase in velocity, and the results show no interesting unexpected outcomes with respect to the base case, setting case III as a good base case for the effects of velocity on the kites in Chapter 5.

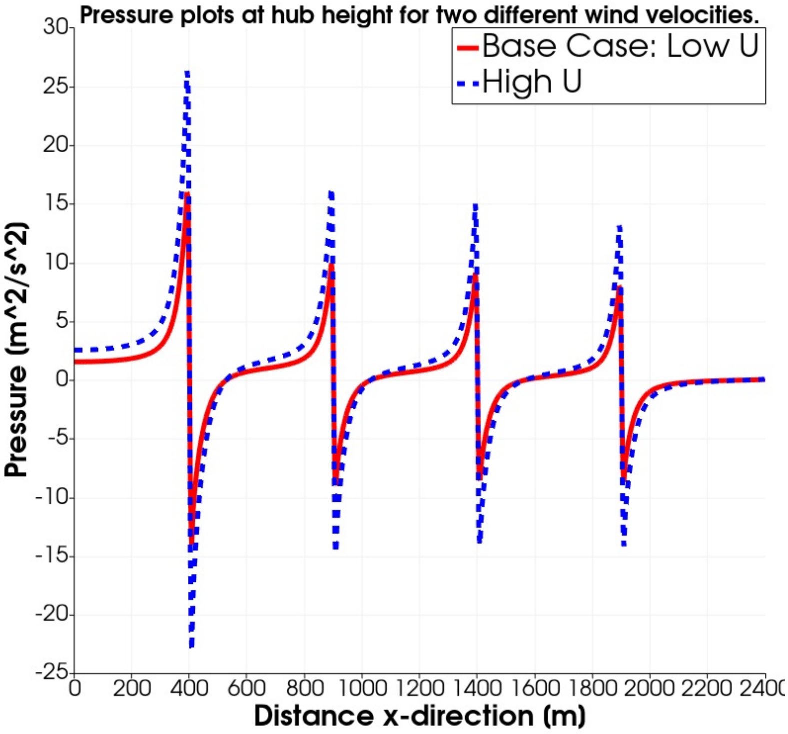

Figure B.1: Pressure line plot at hub height for the higher wind velocity of 10 [m/s]

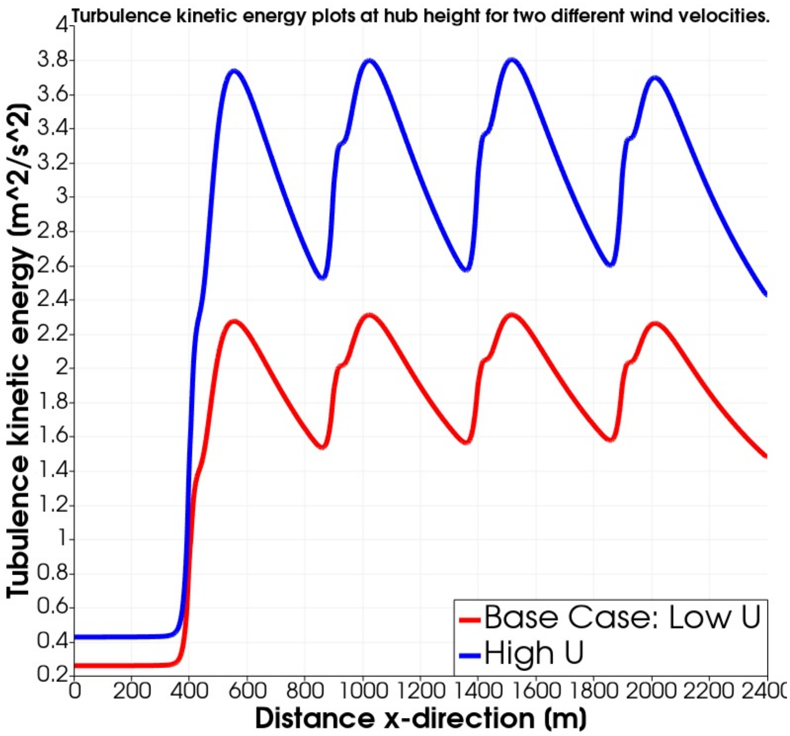

Figure B.2: Turbulent kinetic energy line plot at hub height for the higher wind velocity of 10 [m/s]

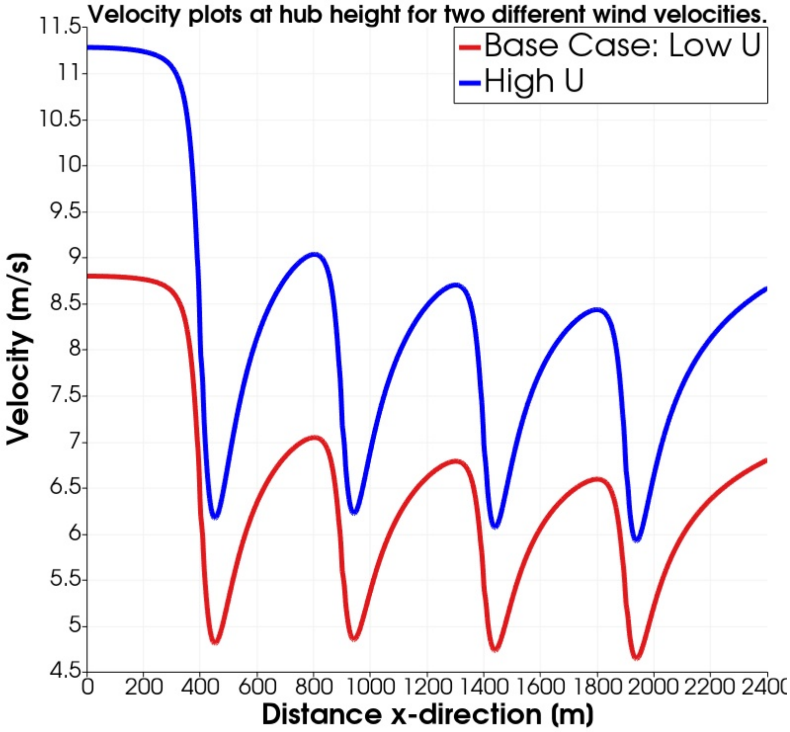

Figure B.3: Velocity line plot at hub height for the higher wind velocity of 10 [m/s]

BIBLIOGRAPHY

Aissa, M. (2017). Gpu-accelerated cfd simulations for turbomachinery design optimization.

Akay, B., Ragni, D., Ferreira, C. S., and Bussel, G. J. W. V. (2013). Investigation of the root flow in a Horizontal Axis. *Wind Energy*, (May 2014):1–20.

Alinot, C. and Masson, C. (2005). KE Model for the Atmospheric Boundary Layer Under Various Thermal Stratifications. *Journal of Solar Energy Engineering, Transactions of the ASME*, 127(4):438–443.

Allaerts, D. and Meyers, J. (2014). Wind farm performance in conventionally neutral atmospheric boundary layers with varying inversion strengths. *Journal of Physics: Conference Series*, 524(1).

American Kitefliers Association (2021). Kite origins. https://www.kite.org/about-kites/history-of-kites/. Last checked on Mar 16, 2021.

Anderson JR, J. (2009). 1 1.1 Conservation Equations. *Auburn University: Governing Equations of Fluid Dynamics*, 3(Cv):1–3.

Avila, M., Gargallo-Peiró, A., and Folch, A. (2017). A CFD framework for offshore and onshore wind farm simulation. *Journal of Physics: Conference Series*, 854(1).

Bachant, P., Goude, A., and Wosnik, M. (2016). Actuator line modeling of vertical-axis turbines. pages 1–21.

Bader, S. H., Inguva, V., and Perot, J. B. (2018). Improving the efficiency of wind farms via wake manipulation. *Wind Energy*, 21(12):1239–1253.

Barth, S., Bot, E. T. G., and Hendriks, H. B. (2007). Evaluation of " Heat and Flux " Farm Control. *Technical Report. Ecn-E-07-105, ECN.*

Barthelmie, R. J., Hansen, K., Frandsen, S. T., Rathmann, O., Schepers, J. G., Schlez, W., Phillips, J., Rados, K., Zervos, A., Politis, E. S., and Chaviaropoulos, P. K. (2009). Modelling and measuring flow and wind turbine wakes in large wind farms offshore. *Wind Energy*, 12(5):431–444.

Bauer, F., Hackl, C. M., Smedley, K., and Kennel, R. M. (2018). Crosswind kite power with tower. *Green Energy and Technology*, (9789811019463):441–462.

Behrouzifar, A. and Darbandi, M. (2019). An improved actuator disc model for the numerical prediction of the far-wake region of a horizontal axis wind turbine and its performance. *Energy Conversion and Management*, 185(February):482–495.

Bierbooms, W (2020). Atmospheric boundary layer. Lecture series Site Conditions for Wind Turine Design (TU Delft) AE4W13. Lecture slides: Atmospheric Boundary Layer. Last checked on Nov 05, 2021.

Boonman, D., Broich, C., Deerenberg, R., Groot, K., Hamraz, A., Kalthof, R., Nieuwint, G., Schneiders, J., Tang, Y., and Wiegerink, J. (2011). Wind Farm Efficiency.

Brand, A. J., Peinke, J., and Mann, J. (2011). Turbulence and wind turbines. *Journal of Physics: Conference Series*, 318(SECTION 7).

Bubba, O (2014). Qunlon q2 4-line traction stunt kites power kites sports beach kites. https://nl.pinterest.com/pin/565342559468593095/. Last checked on Apr 28, 2022.

Burton, T., Jenkins, N., Sharpe, D., and Bossanyi, E. (2011). *Wind Energy Handbook Second Edition*. 2 edition.

Cal, R. B., Lebrón, J., Castillo, L., Kang, H. S., and Meneveau, C. (2010). Experimental study of the horizontally averaged flow structure in a model wind-turbine array boundary layer. *Journal of Renewable and Sustainable Energy*, 2(1).

Calaf, M., Meneveau, C., and Meyers, J. (2010). Large eddy simulation study of fully developed wind-turbine array boundary layers. *Physics of Fluids*, 22(1):015110.

Cañadillas, B., Foreman, R., Barth, V., Siedersleben, S., Lampert, A., Platis, A., Djath, B., Schulz-Stellenfleth, J., Bange, J., Emeis, S., and Neumann, T. (2020). Offshore wind farm wake recovery: Airborne measurements and its representation in engineering models. *Wind Energy*, 23(5):1249–1265.

Churchfield, M. J., Schreck, S., Martínez-Tossas, L. A., Meneveau, C., and Spalart, P. R. (2017). An advanced actuator line method for wind energy applications and beyond. *35th Wind Energy Symposium, 2017*, (March).

Coelingh, J. P., Van Wijk, A. J., and Holtslag, A. A. (1998). Analysis of wind speed observations on the North Sea coast. *Journal of Wind Engineering and Industrial Aerodynamics*, 73(2):125–144.

Cruz, L. E. B. (2019). Wind farm layout optimization based on numerical simulations. *dissertação - Mestrado*.

De Wachter, A. (2008). *Deformation and Aerodynamic Performance of a Ram-Air Wing*. PhD thesis, TU Delft.

Dong, G., Li, Z., Qin, J., and Yang, X. (2021). How far the wake of a wind farm can persist for? *Theoretical and Applied Mechanics Letters*, (xxxx):100314.

Emeis, S. and Turk, M. (2007). Comparison of Logarithmic Wind Profiles and Power Law Wind Profiles and their Applicability for Offshore Wind Profiles. *Wind Energy*, (December):61–64.

Flandro, G., McMahon, H., and Roach, R. (2011a). *Fundamentals of Steady, Incompressible, Inviscid Flows.*, volume 1.

Flandro, G. A., McMahon, H. M., and Roach, R. L. (2011b). *Fundamentals of Steady, Incompressible, Inviscid Flows*, page 110–168. Cambridge Aerospace Series. Cambridge University Press.

Frandsen, S. T. (2007). *Turbulence and turbulence- generated structural loading in wind turbine clusters*, volume 1188.

G. A. M. Van Kuik, G. (2020). On the velocity at wind turbine and propeller actuator discs. *Wind Energy Science*, 5(3):855–865.

Gebraad, P., Teeuwisse, F., van Wingerden, J., Fleming, P., Ruben, S., Marden, J., and Pao, L. (2014). Wind plant power optimization through yaw control using a parametric model for wake effects-a CFD simulation study. *Wind Energy*, 1(October 2014):95–112.

Gilbert, L (2011). Momentum theory of lift. http://www.onemetre.net/design/downwash/momentum/momentum.htm. Last checked on Mar 17, 2021.

Göçmen, T., Laan, P. V. D., Réthoré, P. E., Diaz, A. P., Larsen, G. C., and Ott, S. (2016). Wind turbine wake models developed at the technical university of Denmark: A review. *Renewable and Sustainable Energy Reviews*, 60:752–769.

Greenshields, Chris (2018). Atmboundaryclass. https://cfd.direct/openfoam/user-guide/v6-blockmesh/. Last checked on Nov 01, 2021.

Hall, N (2018). Inclination effects on lift. https://www.grc.nasa.gov/www/k-12/airplane/incline.html. Last checked on Mar 16, 2021.

Hansen, M. (2013). *Aerodynamics of wind turines, second edition*. WIT Press.

Hickel, S (2021). Cfd for aerospace engineers. Lecture series CFD for Aerospace Engineers (TU Delft) AE4202. Last checked on Apr 18, 2021.

Hoem, M. E. and Kristoffersen, R. (2019). Wind turbine simulations with OpenFOAM. *Springer Proceedings in Physics*, 226(January):305–310.

Holtslag, M. C., Bierbooms, W. A., and Van Bussel, G. J. (2014). Estimating atmospheric stability from observations and correcting wind shear models accordingly. *Journal of Physics: Conference Series*, 555(1).

Howland, M. F., Lele, S. K., and Dabiri, J. O. (2019). Wind farm power optimization through wake steering. *Proceedings of the National Academy of Sciences of the United States of America*, 116(29):14495–14500.

Inoue, A., Ali, M. H., Takahashi, R., Murata, T., Tamura, J., Kimura, M., Futami, M. O., Ichinose, M., and Ide, K. (2005). A calculation method of the total efficiency of wind generator. *Proceedings of the International Conference on Power Electronics and Drive Systems*, 2(3):1595–1600.

Ivanova, N., Gugleva, V., Dobreva, M., Pehlivanov, I., Stefanov, S., and Andonova, V. (2016). We are IntechOpen , the world ' s leading publisher of Open Access books Built by scientists , for scientists TOP 1 %. *Intech*, i(tourism):13.

Jerez Venegas, M. (2017). Path Optimization of a Pumping Kite System.

Jeromin, A., Bentamy, A., and Schaffarczyk, A. (2014). Actuator disk modeling of the Mexico rotor with OpenFOAM. *ITM Web of Conferences*, 2(march 2013):06001.

Jrgen, B., Lange, B., and Larsen, S. (2001). Comparison Of Sea Surface Roughness Models For Offshore Wind Power Utilisation. *EWEA special topic*, (1):2–5.

Katyayan, T. (2020). 15 biggest kites in the world. https://topbiggest.com/15-biggest-kites-in-the-world/. Last checked on May 12, 2022.

Kitepower (2016). Plug and play, mobile wind energy. https://thekitepower.com/. Last checked on Apr 29, 2022.

Kumer, V. M., Reuder, J., Dorninger, M., Zauner, R., and Grubišić, V. (2016). Turbulent kinetic energy estimates from profiling wind LiDAR measurements and their potential for wind energy applications. *Renewable Energy*, 99:898–910.

Mano, S., KITAMURA, K., DOI, K., and NAKAMURA, Y. (2014). Numerical Simulation Based on CFD for Aerodynamic Characteristics of Kite in Flight. *Transactions of the Japan Society for Aeronautical and Space Sciences, Aerospace Technology Japan*, 12(0):1–10.

Martínez, L. A., Leonardi, S., Churchfield, M. J., and Moriarty, P. J. (2012). A comparison of actuator disk and actuator line wind turbine models and best practices for their use. *50th AIAA Aerospace Sciences Meeting Including the New Horizons Forum and Aerospace Exposition*, (January).

Meyers, J. and Meneveau, C. (2010). Large Eddy Simulations of large wind-turbine arrays in the atmospheric boundary layer. *48th AIAA Aerospace Sciences Meeting Including the New Horizons Forum and Aerospace Exposition*, (January):1–10.

Morgan, H. L., Ferris, J. C., and Mcghee, R. J. (1987). A Study of High-Lift Airfoils at High Reynolds Numbers in the Langley Low-Turbulence Pressure Tunnel. *Most*, pages 0–62.

Moskalenko, N., Rudion, K., and Orths, A. (2010). Study of wake effects for offshore wind farm planning. *Proceedings - International Symposium: Modern Electric Power Systems, MEPS'10*, (October).

Motta-Mena, J., Jha, P., Campbell, R. L., Schmitz, S., and Brasseur, J. (2014). Wind turbine fluid-structure interaction using an actuator line solver and a finite element solver in a tightly-coupled implementation. *32nd ASME Wind Energy Symposium*, (January).

Nagy, Jozsef (2021). Atmboundaryclass. https://www.openfoam.com/documentation/guides/latest/doc/guide-bcs-inlet-atm-atmBoundaryLayer.html. Last checked on Nov 01, 2021.

Nygaard, N. G. (2014). Wakes in very large wind farms and the effect of neighbouring wind farms. *Journal of Physics: Conference Series*, 524(1).

OpenFOAMltd (2007). atmboundarylayer. https://www.openfoam.com/documentation/guides/latest/doc/guide-bcs-inlet-atm-atmBoundaryLayer.html. Last checked on May 31, 2022.

Panaitescu, M., ANTON, C., PANAITESCU, F.-V., ANTON, I.-A., and TUROF, M. (2019). New solutions to protect the Romanian coastline. (January):10.

Pegg, C., Suri, Y., Islam, S. Z., Asthana, A., and Hossain, M. (2020). Computational fluid dynamics modelling to design and optimise power kites for renewable power generation. *International Journal of Design Engineering*, 9(2):81.

Ploumakis, E. (2015). Improving the Wind Farm efficiency by simple means Evangelos Ploumakis.

Richardson, L. F. (2007). *Weather prediction by numerical process, second edition*, volume 9780521680448.

Richmond, M., Antoniadis, A., Wang, L., Kolios, A., Al-Sanad, S., and Parol, J. (2019). Evaluation of an offshore wind farm computational fluid dynamics model against operational site data. *Ocean Engineering*, 193(October):106579.

Sakai, K., Kubo, R., Kajiya, R., Iwamoto, S., and Kurabuchi, T. (2008). CFD analysis of thermal environment of a room with floor heating or air conditioning. *Indoor Air 2008, 17-22 August 2008, Copenhagen, Denmark - Paper ID: 315 CFD*, (August):17–22.

Salameh, M. (2015). Oil Crises, Historical Perspective. *Reference Module in Earth Systems and Environmental Sciences*.

Schalau, S., Habib, A., and Michel, S. (2021). Atmospheric wind field modelling with OpenFOAM for near-ground gas dispersion. *Atmosphere*, 12(8):1–14.

Schmehl, R (2019a). Airborne wind energy. Lecture series Airborne Wind Energy (TU Delft) AE4T40. Lecture slides: Physics of tethered flight I. Last checked on Mar 16, 2021.

Schmehl, R (2019b). Airborne wind energy. http://awesco.eu/awe-explained/. Last checked on Mar 16, 2021.

Schmitz, S (2015). The rotor disk model. https://www.e-education.psu.edu/aersp583/node/503. Last checked on Mar 15, 2021.

Schreiber, J., Balbaa, A., and Bottasso, C. L. (2020). Brief communication: A double-Gaussian wake model. *Wind Energy Science*, 5(1):237–244.

Segersson, D. (2017). A tutorial to urban wind flow using OpenFOAM. *Proceedings of CFD with OpenSource Software*, pages 1–46.

Siedersleben, S. K., Platis, A., Lundquist, J. K., Djath, B., Lampert, A., Bärfuss, K., Cañadillas, B., Schulz-Stellenfleth, J., Bange, J., Neumann, T., and Emeis, S. (2020). Turbulent kinetic energy over large offshore wind farms observed and simulated by the mesoscale model WRF (3.8.1). *Geoscientific Model Development*, 13(1):249–268.

Sørensen, J. N. and Shen, W. Z. (2002). Numerical modeling of wind turbine wakes. *Journal of Fluids Engineering, Transactions of the ASME*, 124(2):393–399.

Spera, D. A. (2008). Models of Lift and Drag Coefficients of Stalled and Unstalled Airfoils in Wind Turbines and Wind Tunnels. *National Aeronautics and Space Administration, NASA*, (July):1–34.

Steffen, L (2019). The world's biggest wind turbine starts generating enough electricity to power 30,000 homes. https://www.intelligentliving.co/worlds-biggest-wind-turbine/. Last checked on Mar 15, 2021.

Stergiannis, N., Lacor, C., Beeck, J. V., and Donnelly, R. (2016). CFD modelling approaches against single wind turbine wake measurements using RANS. *Journal of Physics: Conference Series*, 753(3).

Stull, R. (1988). Mean Boundary Layer Characteristics. In *An introduction to boundary layer meteorology*, chapter 1, pages 2–26.

Tabas, D., Fang, J., and Porté-Agel, F. (2019). Wind energy prediction in highly complex terrain by computational fluid dynamics. *Energies*, 12(7):1–12.

Tabib, M., Rasheed, A., and Kvamsdal, T. (2015). LES and RANS simulation of onshore Bessaker wind farm: Analysing terrain and wake effects on wind farm performance. *Journal of Physics: Conference Series*, 625(1).

The OpenFOAM Foundation (2017). Openfoam v9 user guide. https://cfd.direct/openfoam/user-guide. Last checked on Nov 13, 2021.

Thumthae, C. and Chitsomboon, T. (2009). Optimal angle of attack for untwisted blade wind turbine. *Renewable Energy*, 34(5):1279–1284.

Tiwari, G., Kumar, J., Prasad, V., and Patel, V. K. (2020). Utility of CFD in the design and performance analysis of hydraulic turbines — A review. *Energy Reports*, 6:2410–2429.

Troldborg, N., Zahle, F., Réthoré, P. E., and Sørensen, N. N. (2012). Comparison of the wake of different types of wind turbine CFD models. *50th AIAA Aerospace Sciences Meeting Including the New Horizons Forum and Aerospace Exposition*, (January):1–11.

Van der Laan, M. P., Sørensen, N. N., Réthoré, P.-E., Mann, J., Kelly, M. C., and Troldborg, N. (2014). The k-E-fPmodel applied to double wind turbine wakesusing different actuator disk force methods. *Wind Energy*, (October 2014):1–18.

Van Dijk, M. T., Van Wingerden, J. W., Ashuri, T., Li, Y., and Rotea, M. A. (2016). Yaw-Misalignment and its Impact on Wind Turbine Loads and Wind Farm Power Output. *Journal of Physics: Conference Series*, 753(6).

VerHulst, C. and Meneveau, C. (2015). Altering kinetic energy entrainment in large eddy simulations of large wind farms using unconventional wind turbine actuator forcing. *Energies*, 8(1):370–386.

Versteeg, H. and Malalasekera, W. (1995). *An Introduction to Parallel Computational Fluid Dynamics*, volume 6.

Verweij, A. P. (2010). An Investigation in Actuator Disc CFD Solution Applicabillity for Aeroacoustic Analysis of Propellers and Rotors.

Vestas (2013). V80-2.0 mw.

Vulpiani, A. (2014). Lewis Fry Richardson: scientist, visionary and pacifist. *Lettera Matematica*, 2(3):121–128.

Weller, H. G., Tabor, G., Jasak, H., and Fureby, C. (1998). A tensorial approach to computational continuum mechanics using object-oriented techniques. *Computers in Physics*, 12(6):620.

White, F. M. (1999). *Fluid mechanics*.

Wijnant, I., van den Brink, H., and Stepek, A. (2014). North Sea wind climatology Part 1: a review of existing wind atlases. *Knmi.Nl*, (May).

Wu, Y. T. (2012). A large-eddy simulation framework for wind energy studies. *Proposal*, (January 2010):1–8.

Yang, W., Quan, Y., Jin, X., Tamura, Y., and Gu, M. (2008). Influences of equilibrium atmosphere boundary layer and turbulence parameter on wind loads of low-rise buildings. *Journal of Wind Engineering and Industrial Aerodynamics*, 96(10-11):2080–2092.

Yang, Y., Gu, M., Chen, S., and Jin, X. (2009). New inflow boundary conditions for modelling the neutral equilibrium atmospheric boundary layer in computational wind engineering. *Journal of Wind Engineering and Industrial Aerodynamics*, 97(2):88–95.

Zhang, X. (2009). *CFD simulation of neutral ABL flows*, volume Risø-R-168.

COLOPHON

This document was typeset using LaTeX. The document layout was generated using the arsclassica package by Lorenzo Pantieri, which is an adaption of the original classicthesis package from André Miede.